Langmuir Trough and Brewster Angle Microscopy Study of Model Lung Surfactant Monolayers at the Air/Aqueous Interface

Thesis

Presented in Partial Fulfillment of the Requirements for the Degree Master of Science in the Graduate School of The Ohio State University

By

Dana-Marie Telesford, B.S.

Graduate Program in Chemistry

The Ohio State University

2012

Master's Examination Committee:

Prof. Dr. Heather C. Allen, Advisor

Prof. Dr. Barbara E. Wyslouzil

ABSTRACT

The alveoli in the human lung have a complex mixture of lipids and proteins that are collectively called pulmonary surfactant (PS). PS is necessary for proper breathing as a deficiency or dysfunction of PS can lead to respiratory distress syndrome (RDS). At present surfactant replacement therapy (SRT) has been used as the preferred treatment for some forms of RDS, however it has not always been proven successful in all cases. In this thesis 1,2-dipalmitoyl-*sn*-glycero-3-phosphocholine (DPPC), 1,2-dipalmitoyl-*sn*-glycero-3-phosphoethanolamine (DPPE), and 1,2-dipalmitoyl-*sn*-glycero-3-phospho-(1'-*rac*-glycerol) (DPPG) lipids of the lung, were studied with a Langmuir trough used in conjunction with the Brewster angle microscopy (BAM) on a water subphase as the temperature and the compression rate were varied. Studying fundamental molecular interactions with respect to each lipid may provide greater understanding of morphology, size, and domain numbers which may provide further insight into better treatment options.

Results illustrated that the compression rate did not have a significant impact on the shape of the isotherms, however the domain morphology was affected. In the coexistence region of the monolayer, the domains were influenced by the temperature of the subphase and the compression rate by way of the shapes, sizes and domain numbers observed. Domains that were formed at the onset of domain formation in the coexistence region had a greater tendency to fuse into larger domains as the compression rate

increased and when the temperature of the subphase was lower than the main phase transition temperature. The fusion of the domains was believed to be observed with all three lipids, however as the temperature of the subphase was increased in the DPPC monolayer, fusion of the domains appear to decrease. The fusion of the domains as the compression rate increased in a cold monolayer suggest that a faster compression rate can induce enough fluctuations in the monolayer to increase the probability of domain-domain interactions DPPG has a main phase transition temperature that is similar to DPPC and fusion was still observed at 37 ^{o}C. These results suggest that DPPG may have a higher phase transition temperature in a monolayer with a neat water subphase. In this thesis, DPPC had the smallest domain size and the largest domain number at 37 ^{o}C on average, it can be inferred that the headgroups have a greater ability to interact with water. Conversely, DPPG was shown to have relatively larger domains than DPPC and as such greater lipid-lipid interactions. Based on results in this thesis, as the alveoli contract and expand while breathing, the lipid type and the rate at which this process occurs may have an impact on the morphology and the number of domains formed.

DEDICATION

This thesis is dedicated to my family and friends.

ACKNOWLEDGMENTS

In the writing of this thesis I would like to thank various members in the Allen lab. First and foremost, I would like to thank my advisor Dr. Heather C. Allen for allowing me to do research in her lab and for her advice, motivation, and support in navigating through graduate school and research. I would also like to thank my fellow colleagues in the Allen lab, in particular Dr. Dominique Verreault for his help in proofreading and making corrections to this thesis. I would also like to thank Ms. Ellen Adams and Ms. Minette Ocampo for helping me with the moving of the BAM setup and also for lending me an extra pair of hands when needed. I would also like to thank my cousins Ann-Marie and Timothy Champ for helping to get settled when I first arrived in the United States. A special thanks to my best friend, Ms Takeisha Dennis, for being there for me through thick and thin. And finally to my family for giving the strength and courage to pursue a higher education and for all their love and support.

VITA

May 12th, 1981	Born – Port-of-Spain, Trinidad & Tobago
2005 - 2009	B.S. Chemistry, South Carolina State University – Orangeburg, South Carolina, USA
2009 – Present	Graduate Teaching Associate, Department of Chemistry and Biochemistry, The Ohio State University – Columbus, Ohio, USA

FIELD OF STUDY

Major Field: Chemistry

TABLE OF CONTENTS

LIST OF FIGURES

LIST OF TABLES

LIST OF ABBREVIATIONS AND SYMBOLS

Abbreviations

ADSA-CSD	axisymmetric drop shape analysis-constrained sessile drop
ARDS	acute respiratory distress syndrome
BAM	Brewster angle microscopy
CBS	captive bubble surfactometer
CCD	charge-coupled device
CF	chrome-free
DPPC	1,2-dipalmitoyl-*sn*-glycero-3-phosphocholine
DPPE	1,2-dipalmitoyl-*sn*-glycero-3-phosphoethanolamine
DPPG	1,2-dipalmitoyl-*sn*-glycero-3-phospho-(1'-*rac*-glycerol)
EM	electromagnetic
G	gas
GDS	Gibbs dividing surface
LC	liquid-condensed
LE	liquid-expanded
LWB	Langmuir-Wilhelmy balance
MMA	Mean molecular area
NA	numerical aperture
NRDS	neonatal respiratory distress syndrome
PA	palmitic acid
PBS	pulsating bubble surfactometer
PC	phosphatidylcholine
PE	phosphatidylethanolamine

PG	phosphatidylglycerol
PI	phosphatidylinositol
PS	pulmonary surfactant, phosphatidylserine
S	solid
SP	surfactant protein
SRT	surfactant replacement therapy
TM	tubular myelin

Symbols

γ	surface tension
γ_0	surface tension of the subphase (water or aqueous solution)
χ_i	reverse rate constant
γ_s	surface tension of the subphase covered with surfactant
β_i	forward reaction rate constant
Γ	surface excess of the solute
Γ_i	surface excess moles of the *i*-th component
λ	wavelength
φ	line tension
μ	chemical potential
μ_i	electrochemical potential of the *i*-th component
τ	dipole density
π	surface pressure
π_{disp}	surface pressure due to dispersive (van der Waals) forces
π_{elec}	surface pressure due to electrostatic forces
π_{kin}	surface pressure due to kinetic forces
π_{other}	surface pressure due to other forces
θ	contact angle
θ_i	incident angle
$\theta_{I,B}$	Brewster angle
θ_r	reflected angle
θ_t	transmitted angle
ρ_p	density of plate

ρ_w	density of subphase (water or aqueous solution)
ω	frequency
A	area, molecular area
c	speed of light
E	total internal energy
$\mathbf{E}$	electric field
$E^{(g)}$	internal energy of phase g
$E^{(l)}$	internal energy of phase l
$E^{(g/l)}$	surface excess internal energy
$\mathbf{E}_0$	amplitude (vectorial) of the electric field
$\mathbf{E}_i$	electric field of the incident wave
$\mathbf{E}_r$	electric field of the reflected wave
$\mathbf{E}_t$	electric field of the transmitted wave
F	force
$F_{buoyancy}$	buoyant force
$F_{gravity}$	gravitational force
F_{surf}	surface tension or tensile force
g	acceleration of gravity, gaseous phase
h	height of submersion of the plate
$\mathbf{H}$	magnetic field
$\mathbf{k}$	wave vector
k_B	Boltzmann constant
$\mathbf{k}_i$	wave vector of the incident wave
$\mathbf{k}_r$	wave vector of the reflected wave
$\mathbf{k}_t$	wave vector of the transmitted wave
l	liquid phase
L	length of plate
n	refractive index
n_i	number of components, refractive index of the incident medium
n_t	refractive index of the transmitted medium

P	pressure
$P^{(g)}$	pressure of phase g
$P^{(l)}$	pressure of phase l
r	position vector
r^p	p-polarized Fresnel reflection coefficient
r^s	s-polarized Fresnel reflection coefficient
R	ideal gas constant
R_p	p-polarized reflectance
R_s	s-polarized reflectance
S	entropy
$S^{(g)}$	entropy of phase g
$S^{(l)}$	entropy of phase l
$S^{(g/l)}$	surface excess entropy
$S_\sigma^{(g/l)}$	surface excess entropy per unit surface area
t	time
t^p	p-polarized Fresnel transmission coefficient
t^s	s-polarized Fresnel transmission coefficient
T	temperature (absolute), thickness of plate
V	volume
$V^{(g)}$	volume of phase g
$V^{(l)}$	volume of phase l
W	width of plate

1. INTRODUCTION

The air/alveolar interface of a healthy human lung contains a complex mixture of lipids and proteins called pulmonary surfactants (PS) whose primary role is to facilitate proper breathing. A deficiency or dysfunction of any PS component can thus lead to respiratory distress syndromes (RDS).[1] For example, premature infants born before 32 weeks are susceptible to neonatal respiratory distress syndrome (NRDS).[2] Another lung disorder, acute respiratory distress syndrome (ARDS), can affect infants, children, and adults.[3] In regards to the treatment of these disorders, surfactant replacement therapy (SRT) has helped reduced NRDS fatalities however this treatment has not been as successful in treating ARDS. Understanding fundamental interactions between PS can therefore aid in development of better treatment options.

In this thesis, three phospholipids present in the PS mixture, namely 1,2-dipalmitoyl-*sn*-glycero-3-phosphocholine (DPPC), 1,2-dipalmitoyl-*sn*-glycero-3-phosphoethanolamine (DPPE), and 1,2-dipalmitoyl-*sn*-glycero-3-phospho-(1'-*rac*-glycerol) (DPPG), were studied on a water subphase. The overall objective of this study is to understand how different physico-chemical parameters (e.g. lipid type, subphase temperature and barrier compression rate) affect interfacial behavior and domain morphology of these phospholipids at the air/water interface with the use of a Langmuir trough and the Brewster angle microscope.

The present thesis is organized as follows: in Chapter 2, the theoretical background as well as a description of each of these experimental methods is given. Chapter 3 presents the surface pressure-area isotherms and BAM images obtained from zwitterionic DPPC and DPPE monolayers spread on a pure water subphase at various temperature and compression rates. Similarly, Chapter 4 presents surface pressure-area isotherms and BAM images of an anionic DPPG monolayer spread also on a pure water subphase. Finally, Chapter 5 summarizes the main results and gives some conclusions.

1.1 Pulmonary Alveoli: Structure and Function

The primary function of the lungs is to obtain and transport oxygen from the atmosphere into the bloodstream during the inspiration phase and release carbon dioxide from the bloodstream back into the atmosphere during the expiration phase.[2] The lungs are divided into two systems, the conducting airways which comprise the trachea, bronchi, bronchioles, and the alveoli which act as the respiratory units (Fig. 1.1). As air enters the nose or mouth it then travels down the trachea to reach the left and right bronchus. These breathing tubes then further divide into the bronchioles. The last order of these bronchioles (also known as respiratory bronchioles) have two to nine generations of alveolar ducts, the last of which ends in grape-like clusters of tiny, thin-walled air sacs or alveoli (from the Italian, "bunch of grapes") called acinus.[4] Each acinus contains approximately 2000 alveoli which amount to an estimated 300 million alveoli for two healthy adult lungs.[5-6] The alveoli are approximately 200 μm in diameter and are surrounded by a network of capillaries where all gas exchange takes place. Gas transfer is

maximized at the alveolar epithelium; for example, at full lung capacity, the gas exchange of a 70 kg adult can be carried over a total surface of about 70 m^2, an area equivalent to that of a tennis court.[7] Moreover, the distance between the alveolar air phase boundary and capillary blood can range between 0.5 to 1.5 µm and allows for rapid gas diffusion.[4]

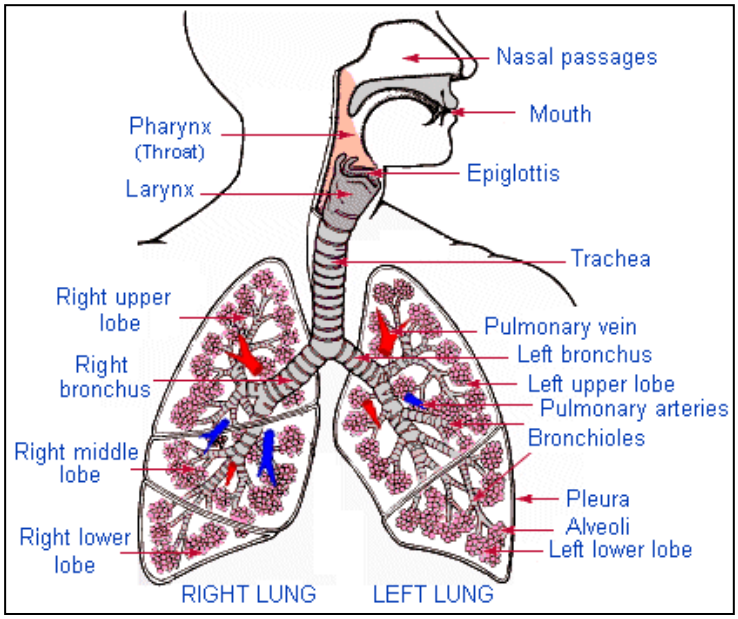

Figure 1.1 Respiratory system comprising conducting airways (trachea, bronchi, and bronchioles) and respiratory units in the form of alveoli[8]

The large surface area and its direct interaction with the atmosphere through every inhalation make the lungs more susceptible to infection, inflammation, and exposure to oxidant gases and small particles.[9] The lungs therefore must have some form of host

defense system in place, whose response is regulated to avoid causing injury to these delicate tissues. This protection mechanism of the lungs against injury however, will not be discussed in this thesis.

The normal alveolar epithelium is composed of two principal cell types, namely type I and type II epithelial cells (Fig. 1.2). Type I (or squamous alveolar) cells form ~90% of the alveolar surface area and their primary function is to prevent fluid loss and facilitate gas exchange.[3] Type II (or great alveolar) cells constitute the remaining of the alveolar surface area and their primary function involves the production, secretion, and recycling of PS components.[2-3] Besides epithelial cells, another type of cell called alveolar macrophages is also present in the lungs. Macrophages are motile phagocytic cells whose main function is to destroy and ingest foreign matter such as air-borne pathogens and particulate matter.[10] Studies done by Quintero *et al.* illustrated that alveolar macrophages can also play a role in the degradation of PS.[11]

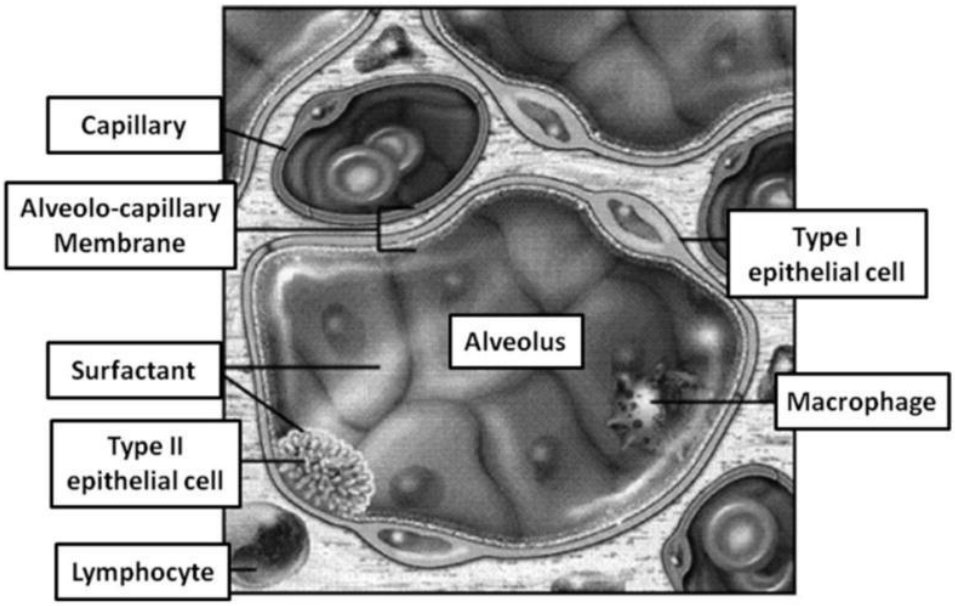

Figure 1.2 Picture illustrating an alveolus with type I, II and macrophage cells.[12]

1.2 Pulmonary Lung Surfactant and Respiratory Distress Syndromes

1.2.1 Pulmonary Surfactants

As mentioned previously, (PS) is a complex mixture of lipids and proteins that lines the alveolar/air liquid interface of the mammalian lung.[13] The primary function of PS is to reduce surface tension at the alveolar air/liquid interface and thereby facilitate breathing and stabilize the alveoli against collapse during expiration.[14-16] PS exist not only in the alveoli, but also in the bronchioles and the small airways.[1] In addition to reducing surface tension, PS are also involved in the antibacterial and antiviral activity, as well as in specific and non-specific host defense.[1, 10, 17-18] The surface tension at the alveolar air/liquid interface without PS is ~70 mN/m.[19-20] Low surface tension in

the lung is associated with the surface of the alveoli becoming enriched with some PS while some components are progressively removed or squeezed out from the surface during expiration.[2] Through this squeezing out mechanism, some PS components are either lost to the subphase or stored in reservoirs in the vicinity of the monolayer to facilitate readsorption when the surface tension is lowered upon inspiration.[21-24] By reducing surface tension in the alveoli, PS greatly reduces the energy expenditure required in breathing.[25-26]

The complex mixture of lipids and proteins that make up PS are produced, secreted, and recycled by type II alveolar cells.[2] The composition of the PS at the surface of the alveoli is ~90% phospholipids and ~10% proteins in weight.[2] It is important to note that the composition of these surfactants may vary depending on the method used during extraction and the source used to obtain the surfactant as there are compositional differences between mammals.[2] However the most prevalent lipids in the lung have a phosphatidylcholine (PC) headgroup, which accounts for approximately 80% of the total phospholipids extracted from the lung lavage of most animal species (Table 1.1). The PC headgroup of lipids have either saturated or unsaturated acyl chains, whose length and saturation have an impact on the fluidity of the lipid.[2]

The predominant lipid component of PS which accounts for approximately 40% of all PC, is DPPC, a disaturated 16 carbon chain lipid mainly responsible for reducing surface tension values to near-zero values upon film compression.[27] Despite its high capacity to reduce surface tension, DPPC does not adsorb or respread to the surface quickly enough *in vivo*.[27] At 37 ^{o}C, DPPC typically exists in a gel phase, i.e., with its

acyl chains in a rigid close-packed arrangement such that it can form a condensed monolayer upon compression and withstand high surface pressures. In contrast, unsaturated lipids at 37 ^{o}C exist in a liquid crystalline phase and cannot form a condensed monolayer in a highly compressed state. Unsaturated lipids are more fluid-like because of the double bond and thus respread quicker than their saturated counterparts. Therefore the presence of unsaturated lipids in the PS helps in fluidizing and respreading DPPC and other saturated lipids.[2] These two desirable properties, stability and fluidity, are possessed by no single lipid component hence many different lipid components are needed *in vivo* for proper PS functioning.

Other phospholipids classes that are also present in lung surfactants, although in smaller amounts, include phosphatidylethanolamine (PE), phosphatidylglycerol (PG), phosphatidylinositol (PI), and phosphatidylserine (PS). Their abundance in the human lung is summarized in Table 1.1. These lipids also help in the adsorption and respreading of DPPC. At physiological pH, PC and PE lipids are zwitterionic, i.e. carry no net electrical charge, while PG, PI and PS lipids are anionic or negatively charged. The anionic phospholipids have been shown to interact with the cationic surfactant protein B (see below), with PG showing the greatest preference.[28-29] It is believed that the interaction between anionic phospholipids and surfactant protein B are critical for the proper functioning of PS at the air/alveolar liquid interface. The neutral lipids constitute 10% by weight of the PS with cholesterol accounting for approximately 80-90% by weight.[2] The main function of cholesterol lies in its ability to maintain the balance between fluidic and rigid lipid phases in lung surfactant.[2]

Table 1.1 Human lung PS lipid composition.[2, 30]

Lipid type	*% Weight*
Disaturated PC	55
Unsatured PC	25
PG	5.4-8.2
PE	3.3-4.1
PI	4.1-6.7
Sphingomyelin	1.7-2.5
Other lipids	1.7-2.0

Besides the aforementioned lipidic components, four surfactant proteins (SPs) are also present in the PS, namely SP-A, SP-B, SP-C, and SP-D.[31] SP-A is a large multimeric hydrophilic glycoprotein consisting of 18 monomers, each weighing 28-36 kDa.[32-33] SP-A has multiple functions including aiding in lipids adsorption and respreading at the alveolus surface and in the innate immune defense of the lung.[34-35] SP-D (43 kDa) is the other hydrophilic protein that is involved in the first line of defense against fungal, bacterial, and viral infections.[36] Both of these two proteins enhance the phagocytosis of bacteria and viruses and exert regulatory effects on type II cells. The other two proteins, SP-B (8 kDA) and SP-C (4 kDa), are hydrophobic and are relatively small in size compared to SP-A and SP-D. Because of their hydrophobicity, these two proteins interact with the lipids in the monolayer as oppose to the hydrophilic proteins.

SP-B however, is the most active among the surfactant proteins in promoting adsorption of the PS at the air/alveolar liquid interface.[37] Table 1.2 summarized some characteristics of the surfactant proteins.

Table 1.2 List of surfactant proteins.[38]

Protein Type	***Molecular Weight [kDa]***	***Surface Activity***
SP-A	26-38	-----
SP-B	8	high
SP-C	4	very high
SP-D	43	------

1.2.2 Life Cycle of Pulmonary Surfactants

The life cycle of PS involves many steps and has been described in several reviews and will only be briefly discussed here.[30, 39] Before PS is adsorbed to the air/alveolar liquid interface, lamellar bodies containing the PS are secreted into the liquid lining of the alveoli hypophase by way of exocytosis across the type II cell membrane (Fig. 1.2). The lamellar bodies then swell and unfold to form tubular myelin (TM) mesh-like structures consisting of both lipids and proteins (mainly SP-A and SP-B). From the TM the lipids are either supplied directly to the alveolar air/alveolar liquid interface or are stored in surfactant reservoirs in its vicinity. The two hydrophobic proteins, SP-B and

SP-C, aid in the adsorption of the lipids to the interface. On compression of the surfactant film during expiration, some of the lipids are squeezed out from the monolayer into the reservoirs. However the exact mechanism is not yet fully understood. Nevertheless, recent modifications to the so-called squeeze-out model suggest that upon compression hydrophobic SPs induce the formation of unsaturated phospholipids-rich multilayers which remain associated with a monolayer enriched in saturated phospholipid species.[40] This restructuring of the air/alveolar liquid interface results in near-zero surface tension values during compression. After inspiration, some of the lipids in the reservoirs are readsorbed into the surface film. When the PS has performed their role they are removed from the interface; the PS is retaken by the type II cells via endocytosis where some of the surfactant components are recycled to avoid the need of *de novo* synthesis.[2]

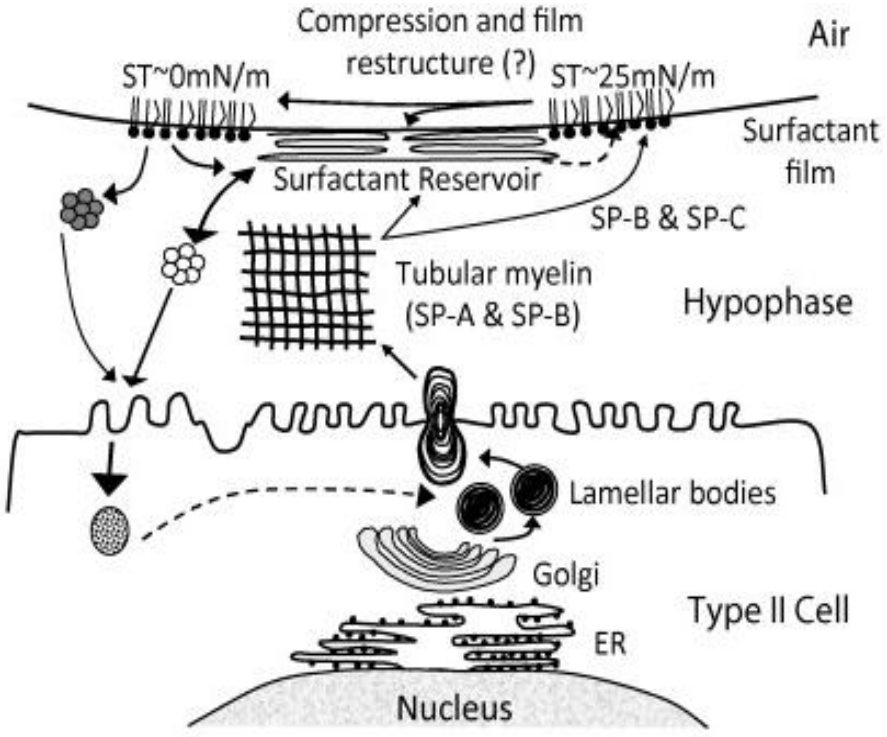

Figure 1.3 Schematic representation of the life cycle of PS. [41] [42]

1.2.3 Respiratory Distress Syndromes

PS is critical to our survival as a deficiency or dysfunction in any component of this complex mixture can result in a respiratory disorder. One such example, NRDS affects premature infants because of the structural immaturity of their lungs and consequent deficiencies of surfactant components.[43] NRDS is the leading cause of death in premature infants, affecting 1% of newborn infants yearly.[44] Another respiratory disorder, ARDS, can affect infants, children, and adults and generally is the result of lung injury. ARDS affects approximately 150,000 people per year in the USA and has a fatality rate of approximately 30-40%.[1, 45] A premature infant suffering with

NRDS exhibits labored breathing, decreased lung compliance, and alveolar collapse which is associated with a reduced functional capacity.[1-2] A patient suffering with ARDS has inhibition of the surfactant components resulting from leakage of serum proteins, hemoglobin, and certain lipids from the small capillaries that surround the alveoli.[1, 46] The leakage of these components in the lungs are generally the result of the inhalation of toxic gases, severe lung infections, inhalation of gastric contents, and circulatory shock near drowning or radiation damage.[3, 45] Patients diagnosed with RDS show signs of progressive lung failure, which is an indication of collapsed alveoli, decreased lung compliance, decreased functional residual capacity, and lung edema.[47]

The present treatment available for NRDS is (SRT), which consists in the application of exogenous animal lung surfactants directly into the airways.[48] One of the SRT surfactants most commonly used in the treatment of NRDS is Survanta™, a commercially available exogenous surfactant mixture consisting of organic extracts of bovine PS supplemented with synthetic palmitic acid (PA) and tripalmitin.[49] Administration of Survanta™ to infants afflicted with NRDS has proven to be a very effective method in the treatment of this disease. Even though SRT formulations have reduced mortality rates by 30-50%, many improvements are still needed.[49] Most SRTs are animal-derived with problems associated with the cost of purification, inadequate supply, as well as possible viral infections, and immunological responses.[48-49] These are just a few of the concerns that are behind the drive to develop fully synthetic and improved PS substitutes for which the exact formulation is known and that functions just

as well as those from animal sources. However, in order to do so, it is imperative to understand the complex interactions taking place between the different PS components.

1.3 Lipid Monolayers as Model of Pulmonary Surfactants

A Langmuir monolayer is a one-molecule thick film formed by an insoluble compound adsorbed or spread at the air/water interface. A molecule that has the ability to adsorb and form such a monolayer is called surface-active or simply a surfactant.[50] Surfactants are composed of two dissimilar parts, a polar headgroup that is soluble in water (hydrophilic) and a nonpolar tail that is insoluble in water (hydrophobic). As a result of this amphiphilic character, surfactants predominantly adsorb at the air/water interface with their tails located in the air phase and their headgroup solvated by the water subphase. Examples of surfactants are biological (macro)molecules such as lipids including fatty acids and phospholipids as well as some proteins.

1.3.1 Lipid Monolayers

Monolayer studies involving biologically-relevant phospholipids and their mixtures at the air/liquid interface have been studied extensively because of their ability to mimic biological membranes.[51-53] The wide variety of lipids in many biological systems and the specificity of the lipid composition of different types of membranes suggest that many of these lipids have specific roles to play.[51, 54] The possibilities they offer in measuring the effects of various physico-chemical parameters (lipid type,

subphase temperature, pH and ionic composition, cholesterol content, surface pressure, etc.) on the interactions between lipid molecules are endless.[55-56] Early studies have mainly focused on measuring surface pressure-area isotherms (see Chapter 2) on single-component phospholipid monolayers[57-58] or their mixtures with cholesterol.[59] Sincethen, many other studies have been done using imaging,[60-63] reflectivity,[64-65] and/or spectroscopic techniques[66-68] to look at the 2D structure and phase transitions of lipid monolayers at the air/water interface.[69-71]

1.3.2 Lipid Monolayers with Surfactant Components

Monolayer studies in recent years have become more complex as a more realistic model of biological membranes is needed to truly comprehend fundamental interactions in membranes.[25] Holten-Andersen *et al.* looked at PS components with a protein analogue to observe the structures formed in the collapse region of the monolayer with the use of a fluorescence microscopy.[72] In another study, Dhar *et al.* observed protein interactions with the lipid monolayer in the coexistence region to assess their impact on the lipid domain size and shape.[73] The protein used, SP-B preferred to remain in the fluid portion of the monolayer rather than in the liquid condensed phase thereby increasing the line tension resulting in an increase in the number of domains. In the case of cholesterol, experiments were done as early as 1986 to understand its impact on the domain shape of DPPC; it was found the cholesterol reduced the line tension of DPPC because of its preferential interaction with the solid phase as opposed to the fluid phase.[74] The domain shapes observed were different than those found in a pure DPPC

monolayer with the cholesterol narrowing the width of the domain.[74] These three experiments are just a few examples of studies focused on understanding the fundamental interactions between the lipids and other components.

2. THEORETICAL BACKGROUND AND TECHNIQUES

2.1 Surface Tensiometry theory

2.1.1 Gibbs Adsorption Equation

To fully understand surfactant adsorption, one must first look at the thermodynamics of two bulk phases, for example a liquid (*l*) and its vapor (*g*), in contact with each other.[75] This physical system can be represented by a liquid column containing the two bulk phases *g* and *l*, each with a number of components (n_i), and separated by an interfacial region *g*/*l* (defined between the planes G and L) (Fig. 2.1); as such, this system could be considered as a real representation of an actual interface. Evidently, this system is known to be inhomogeneous, especially in the interfacial region, such that a simplified system is usually devised. In the ideal system the two phases *g* and *l* are not separated by an actual interfacial phase but by a mathematical plane called the Gibbs dividing surface (GDS) that is placed at an arbitrary position parallel to planes G or L in phase *g* and *l*, respectively.

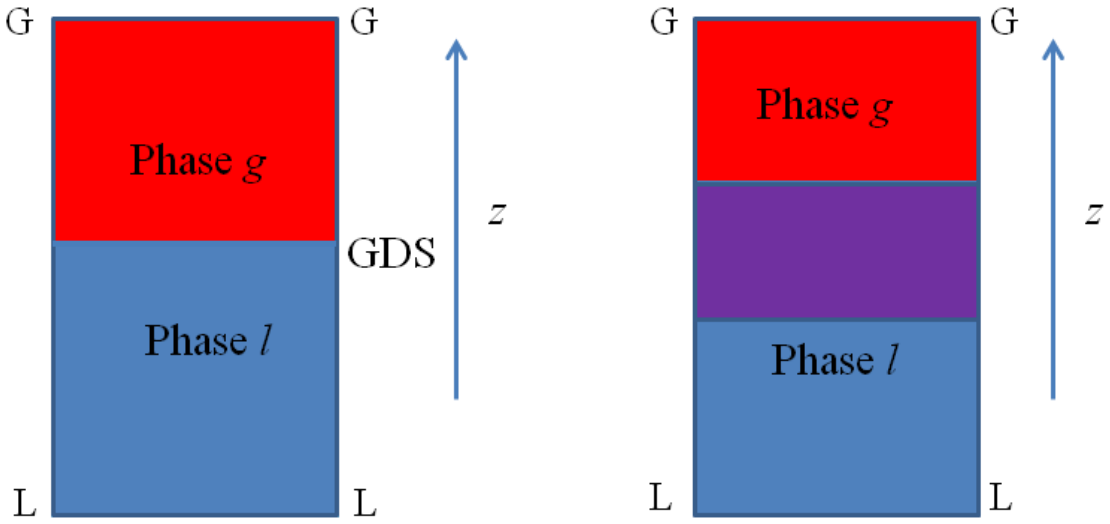

Figure 2.1 Liquid column made of two phases g and l

To define the system by using thermodynamics, one can first look at the surface excess internal energy $E^{(g/l)}$ and the entropy $S^{(g/l)}$ defined by[75]

$$E^{(g/l)} = E - \left(E^{(g)} + E^{(l)}\right), \tag{2.1}$$

and

$$S^{(g/l)} = S - \left(S^{(g)} + S^{(l)}\right), \tag{2.2}$$

where E, S represent the total internal energy and entropy of the actual system, whereas $E^{(i)}$, and $S^{(i)}$ (i: g, l) denote the internal energy and entropy of phases g and l in the ideal system.

The internal energy and the entropy can vary depending on the position of the plane of the GDS, and can either be negative, positive, or zero. The change in the total internal energy for the real system can be represented by

$$dE = TdS - \left(P^{(g)}dV^{(g)} + P^{(l)}dV^{(l)} - \gamma dA\right) + \sum_{i=1}^{N}\mu_i dn, \tag{2.3}$$

where $P^{(i)}$ and $V^{(i)}$ (i: g, l) represent the actual volume and pressure of the phases g and l in the real system. A denotes the area with regards to the liquid surface, γ the surface tension of the liquid phase, and T the (absolute) temperature. Since the volume of the interfacial region is negligible, the total volume of the system is usually $V_t \approx V^{(g)} + V^{(l)}$. Moreover, if the surface is almost planar then $P^{(g)} = P^{(l)}$.

Similarly, the differential changes in the internal energy of the two phases g and l in the ideal system due to changes in heat and work in a reversible process can be expressed by

$$dE^{(g)} = TdS^{(g)} - PdV^{(g)} + \sum_{i=1}^{N}\mu_i dn_i^{(g)}, \tag{2.4}$$

and

$$dE^{(l)} = TdS^{(l)} - PdV^{(l)} + \sum_{i=1}^{N}\mu_i dn_i^{(l)}. \tag{2.5}$$

In the ideal system $V_t = V_g = V_l$ and, as in the real system, $P_g = P_l$ such that the pressure terms in Eqs. (2.4) and (2.5) can be represented by PdV_t. The surface energy term (γdA) is neglected in the ideal system since only the two bulk phases exist. To obtain the change

in surface excess internal energy of the interfacial region, Eqs. (2.4) and (2.5) (ideal system) are added and then subtracted from Eq. (2.3) (real system). The obtained result is

$$dE^{(g/l)} = TdS^{(g/l)} + \gamma dA + \sum_{i=1}^{N} \mu_i dn_i^{(g/l)}. \tag{2.6}$$

Eq. (2.6) can then be integrated only over the extensive properties (S, V, n_i) and keeping the intensive properties (T, γ, μ_i) constant such that[75]

$$E^{(g/l)} = TS^{(g/l)} + \gamma A + \sum_{i=1}^{N} \mu_i n_i^{(g/l)}. \tag{2.7}$$

Differentiating Eq. (2.7) yields

$$dE^{(g/l)} = \left(TdS^{(g/l)} + S^{(g/l)}dT\right) + (\gamma dA + Ad\gamma) + \sum_{i=1}^{N} \left(\mu_i dn_i^{(g/l)} + n_i d\mu_i^{(g/l)}\right). \tag{2.8}$$

Adding Eqs. (2.6) and (2.8) finally gives

$$-Ad\gamma = S^{(g/l)}dT + \sum_{i=1}^{N} n_i^{(g/l)} d\mu_i, \tag{2.9}$$

or

$$-d\gamma = S_\sigma^{(g/l)}dT + \sum_{i=1}^{N} \Gamma_i^{(g/l)} d\mu_i, \tag{2.10}$$

with the surface excess entropy and surface excess moles of the i-th component defined as

$$S_\sigma^{(g/l)} \equiv \frac{S^{(g/l)}}{A}, \tag{2.11}$$

$$\Gamma_{\mathrm{i}}^{(\mathrm{g}/l)} \equiv \frac{n_i^{(g/l)}}{A}. \tag{2.12}$$

At constant temperature, Eq. (2.10) reduces to a surface (two-dimensional) version of the well-known Gibbs-Duhem equation for the bulk phases.

Unfortunately, the values of $S_\sigma^{(g/l)}$ and $\Gamma_i^{(g/l)}$ in Eq. (2.10) are dependent on the arbitrary position of the GDS. To make this equation physically more meaningful, the GDS can be shifted along the *z*-direction. For a phase *l* with two components, e.g. the solvent (*l*) and a solute (*s*) such as a surfactant molecule, the GDS can be fixed at a particular location where $n_l = n_l^{(g)} + n_l^{(l)}$. Under this condition, $n_l^{(g/l)} = 0$ (since $n_l^{(g/l)} = n_l - (n_l^{(g)} + n_l^{(l)})$) and $\Gamma_l^{(g/l)} = 0$ by virtue of Eq. (2.12), and Eq. (2.10) becomes at constant temperature

$$-d\gamma = \Gamma_s^{(g/l)} d\mu_s, \tag{2.13}$$

or

$$\Gamma_s^{(g/l)} = -\frac{d\gamma}{d\mu_s}, \tag{2.14}$$

where $\Gamma_s^{(g/1)}$ are now defined as relative surface excess moles per unit area of the solute. It represents the amount of solute accumulated in excess or adsorbed at the interface.

The differential change of the chemical potential of the solute is related to its molar fraction such as

$$d\mu_s = RTd(\ln a_{s,l}) = RTd(\ln \gamma_s x_s), \tag{2.15}$$

where $a_{s,l}$, γ_s x_s, and R refers to the relative activity of s in l, the activity coefficient and molar fraction of s, and the ideal gas constant. Putting Eq. (2.15) into Eq. (2.14) and assuming dilute solution ($\gamma_s \approx 1 \Rightarrow x_s \approx c_s$) finally yields[75]

$$\Gamma_s^{(g/l)} = -\frac{1}{RT}\left[\frac{d\gamma}{d(\ln c_s)}\right] = -\frac{c_s}{RT}\frac{d\gamma}{dc_s}. \tag{2.16}$$

This equation is referred to as the Gibbs adsorption equation. From Eq. (2.16), it is obvious that an increase in surface excess (i.e. more solute is adsorbed to the surface) results in a decrease in surface tension (because of the negative slope).

2.1.2 Surface Free Energy and Surface Tension

As mentioned previously the interfacial region is very thin, inhomogeneous, and as such not well defined. Nevertheless, one can define a region of arbitrary thickness as an imaginary surface phase. From Eq. (2.6), the change in total internal energy of this phase is given by

$$dE^{(g/l)} = TdS^{(g/l)} + \gamma dA + \sum_{i=1}^{N} \mu_i dn_i^{(g/l)}. \tag{2.17}$$

Since $E^{(g/l)} = G^{(g/l)} - PV^{(g/l)} + TS^{(g/l)}$, then Eq. (2.12) can be rewritten as

$$dG^{(g/l)} = -S^{(g/l)}dT + V^{(g/l)}dP + \gamma dA + \sum_{i=1}^{N} \mu_i dn_i^{(g/l)}, \tag{2.18}$$

where $S^{(g/l)}$, $V^{(g/l)}$, and $n_i^{(g/l)}$ are the extensive properties that are related to the surface phase. Keeping these properties constant, Eq. (2.18) can then be reduced to:[75]

$$\gamma = \left(\frac{\partial G^{(g/l)}}{\partial A}\right)\Big|_{T,P,n_i^{(g/l)}}, \tag{2.19}$$

where the surface tension γ represents the rate of change of the Gibbs free energy of the interface per unit area at constant T, P, and $n_i^{(g/l)}$. Hence, surface tension can be defined as the work required to increase the area of a surface reversibly and isothermally by a unit amount.[76]

Physically, the surface tension of a liquid involves the contraction of an interface resulting in the reduction of the total interfacial area. The reduction of the area can best be explained by the imbalance of the cohesive forces in the interfacial region. Indeed a pure liquid in contact with a vapor phase that are immiscible with each other have different chemical potentials, densities, and molecular interactions. At the molecular scale, if one looks in the bulk of the liquid phase in which the attraction between the molecules are van der Waals or dispersive forces, one sees that the molecules are equally attracted to one another because all the molecules are surrounded by essentially an identical force field. However, at the surface of the liquid the molecules experience a distorted field because the forces of attraction coming from the gaseous and liquid phases are different, thus resulting in the pulling of the interfacial molecules towards the bulk of the liquid and a reduction of the interfacial area. At room temperature the surface tension of most liquids ranges between 10-80 mN/m.[75] In comparison to other liquids, water at

room temperature exhibits a rather high surface tension of approximately 72 mN/m because of its strong hydrogen bonding ability.

2.1.3 Experimental Measuring Techniques of the Surface Tension of PS Monolayers

There are many different experimental techniques that have been developed to study the PS in a monolayer. The three most widely used techniques are the Langmuir-Wilhelmy balance (LWB), pulsating bubble surfactometer (PBS), and the captive bubble surfactometer (CBS).[1] Another method that has been recently developed is the double injection axisymmetric drop shape analysis-constrained sessile drop (ADSA-CSD).[77] A brief overview will be given for all these techniques, however emphasis will be put on the LWB method as this was the technique used in this thesis.

The LWB is a well established and widely used technique to characterize the physical state of an adsorbed Langmuir monolayer.[78] The basic instrumentation consists in a Langmuir trough are one or two movable barriers and a Wilhelmy plate tensiometer. In a typical experiment, a small amount of surfactant is first dissolved in an organic solvent, and then carefully deposited on the surface of a subphase contained in the trough. The solvent then evaporates leaving only the surfactant molecules on the subphase to spread and occupy all the available surface area to form a monomolecular layer. The monolayer that is then formed on the interface can then exert a surface pressure in two dimensions.[75] The surface pressure and, in turn, the physical state of the monolayer can then be increased or decreased by compressing or expanding the trough's barriers, respectively. The measurement of the surface tension is accomplished

by means of the Wilhelmy plate whose principle is based on the pulling forces needed for detachment from the fluid/liquid interface.[79] Experiments involving Langmuir monolayers are quite easy to perform because the temperature and the surface pressure can be varied in a controlled manner.[80] The other parameters that can also be manipulated are surfactant type and composition, as well as pH, ionic strength of the subphase and the compression rate of the monolayer. Due to the ease in which these experimental constraints can be manipulated, a Langmuir monolayer can serve as an excellent model in the study of many different systems, for example biological and chemical reactions in two dimensions.[80]

The basic principle of the Wilhelmy plate measurement relies on the pulling forces, a sum of the contribution from gravity, buoyancy, and surface tension, which act on a thin, vertical plate.[2] Traditionally, the plate was made of platinum but because of its sensitivity to cleanliness and difficulties in obtaining reproducible contact angles, modern instruments now use ashless filter paper as a cheaper alternative. When the filter comes into direct contact with the interface, an equilibrium of forces acting on the plate is established between an upward force, the buoyancy, and downward forces like gravity and surface tension pull. The contact angle of the plate relative to the subphase should be zero as the surface tension is at a maximum at this angle. The magnitude of the surface tension is also dependent on the perimeter and the depth of the plate. The resulting downward forces on the plate is given by[75]

$$\begin{aligned} F &= F_{surf} + F_{gravity} + F_{buoyancy} \\ &= 2\gamma_w(W+T)\cos\theta + (WTL)\rho_p\, g - (WTh)\rho_w g, \end{aligned} \tag{2.20}$$

where *W*, *T*, and *L* correspond to the width, thickness, and length of the plate, *h* is the height of the plate that is submerged into the subphase, γ_w is the surface tension of the subphase (water or aqueous solution), θ is the contact angle, ρ_p is the density of the plate, g is the acceleration of gravity, and ρ_w is the density of the liquid subphase. Eq. (2.20) can be used to measure the difference in the surface tension forces at the air/water interface with or without surfactant monolayer coverage. Assuming that the filter paper has constant dimensions and immersion depth as well as full wetting of the paper plate ($\cos\theta \approx 1$), the difference in surface forces termed surface pressure (π) is then given by

$$\pi = \gamma_w - \gamma_s, \tag{2.21}$$

where γ_s is the surface tension of subphase covered with a surfactant monolayer.

There are many advantages and disadvantages related to the LBW technique. One advantage is its ability to be used in tandem with microscopic and spectroscopic techniques.[1] Another advantage lies in the fact that the surface pressure per molecule can be precisely determined be varying the amount of the molecule that is deposited onto the subphase. However drawbacks associated with this technique include, the amount of material that can be studied must be not smaller than a few milliliters, the compression-expansion rate used has to be relatively slow approximately 5 min per cycle.[2, 77] The slow compression rate of Langmuir trough is thus not physiologically relevant to simulate breathing. Another limitation with this method is the film leakage induced by subphase surface meniscus inversion at high surface pressures. At high surface pressure i.e. low

surface tension the surfactant molecules can spread from the air/water interface onto the surrounding areas of the trough. This occurs because thermodynamically this process reduces the free energy of the system; only with specially designed Langmuir troughs can this condition be overcome.[81-82] The environmental conditions under which the experiments are performed also have an impact on the surface pressure-area isotherms. For instance, the subphase temperature and the relative humidity can be difficult to control with this technique.

PBS is another surface tension measuring technique that was first introduced by Enhorning in 1977.[1, 83] The equipment needed for this particular technique include a sample chamber, the pulsator unit and a pressure recording device.[83] The sample chambers are disposable and usually made of polyacrylamide; this chamber can contain 20 μl of the test liquid that is then immersed in a temperature bath. Air from the atmosphere is then allowed to enter the instrument via a capillary tube that then forms a bubble. To reach the cyclic change in size of the bubble, a pulsator attached to the instrument makes the bubble radius oscillate between two fixed positions, a minimum radius of 0.4 mm and a maximum radius of 0.55 mm. To simulate breathing with this technique, a cycling frequency of 20 cycles/min is used. An optical microscope then monitors the contraction and expansion of the bubble. The pressure gradient (ΔP) generated across the bubble is measured by a pressure transducer and the surface tension can finally be calculated by using the Laplace equation:

$$\Delta P = \frac{2\gamma}{R} \tag{2.22}$$

where *R* corresponds to the radius of the bubble. From Eq. (2.22) it is easy to see that with a small radius the pressure gradient will be large and vice versa.

One of the advantages with this technique is the time taken to perform experiments which typically is of the order of a few minutes. Two important parameters can be determined by this method, first the adsorption rate of the surfactant molecule can be observed when the bubble has a maximum radius, and can be simply determined by looking at the surface tension.[1] Secondly the ability of the surfactant molecule used to reach low surface tension values when the bubble has a minimum radius. One important advantage that this technique has on the LWB method is the fact that it has a physiologically-relevant cycling rate. The disadvantages associated with this technique include leakage, flexibility in accessing the surface activity and finally low surface tension measurements which are often not reliable.

The CBS technique was first developed by Schurch *et al.* in 1989.[1, 84] An air bubble with diameter ranging between 2-7 mm is introduced into a chamber where it floats against its ceiling coated with 1% agar gel. The agar is attached to the walls of the chamber with its main purpose to render the ceiling of the chamber hydrophilic. The end result is to have the bubble surrounded by a thin layer of wetting film that prevent the bubble from adhering to the ceiling bear surface therefore eliminating any potential for leaks. A film of surfactant is then spread on the surface of the bubble with a microsyringe. When the film is formed, the bubble can then be compressed or expanded by varying the hydraulic pressure in the chamber. In this case, the surface tension is

determined by the Young-Laplace equation which takes into account the balance of forces between applied and hydrostatic pressure:

$$\Delta P = \frac{2\gamma}{R_o} = \Delta\rho g z - \gamma\left(\frac{1}{R_1} + \frac{1}{R_2}\right), \tag{2.23}$$

where R_1 and R_2 are the two principal radii curvature at the points of the surface to be studied, that determine the shape of the bubble. R_o is the radius of curvature at the apex of the bubble; $\Delta\rho$ corresponds to the difference in density across the interface; g is the local gravitational acceleration and z is the vertical distance from the apex to the studied point.

The advantages associated with this technique include no leakage, and the fact that the collapse region and compressibility of monolayers can be studied. Another advantage with this technique is the capability to have an environment similar to that of the alveoli. The drawbacks of this technique include the difficulty involved in operating and cleaning up the instrument, limitation associated with the concentration of the surfactant that can be used and the impossibility in varying relative humidity.

The CSD technique involves the formation of a sessile drop on a pedestal with sharp knife edges that confines the drop from over spreading, and, in turn, prevent the leakage of material. The sessile drop is connected to a surfactant reservoir that is constantly stirred. The volume of the drop that is formed is then regulated by a computer controlled motor-driven syringe that flows in and out the surfactant sample from a reservoir. During a typical experiment the drop and pedestal are enclosed in a chamber

that allows for the control of the gas composition and temperature. A CCD camera is then used to acquire images of the drop throughout the experiment. To analyze the data, the ADSA determines the surface tension by numerically fitting the shape of the drops to a theoretical profile generated using the Laplace equation.[85] The advantages associated with this technique include, being leakproof, easy to clean and operate, the environmental conditions are easy to control, use of small amount of sample, and an accurate determination of the surface tension when used in conjunction with the ADSA.

2.1.4 Surface Pressure-Molecular Area Isotherm and 2D Equations of State

The study of Langmuir monolayer phase transition is important in many ways because they are quasi-two dimensional (2-D) systems and are therefore easier to examine and explain theoretically than their three dimensional (3-D) counterparts.[86] The shape of the surface pressure-molecular area (π-A) isotherm gives information on the monolayer formation, phases, and stability, etc. The π-A isotherms are a direct measure of the physical force interacting between alkyl chains, polar headgroups, as well as between headgroups and the liquid subphase. When the molecules approach each other in a monolayer there is a change in the interacting forces which results in changes of the orientation and packing density of the monolayer. The π-A isotherm for a film are analogous to the 3-D pressure-volume isotherm of a gas.[75] For instance, increasing the pressure of a gas in a volume leads to phase changes of the gas; in the same way, increasing the surface pressure on a film also induces the appearance of different phases. Despite this analogy, these two systems have a striking difference. For a gas molecule in

a 3-D system the molecules are in close contact to neighboring molecules and may also interact with other molecules that are 5 to 10 molecular dimensions away.[75] In contrast, for a surfactant molecule in a 2-D monolayer the molecules have fewer interactions with each other since the polar headgroups are oriented towards the liquid subphase and the alkyl tail away from it.

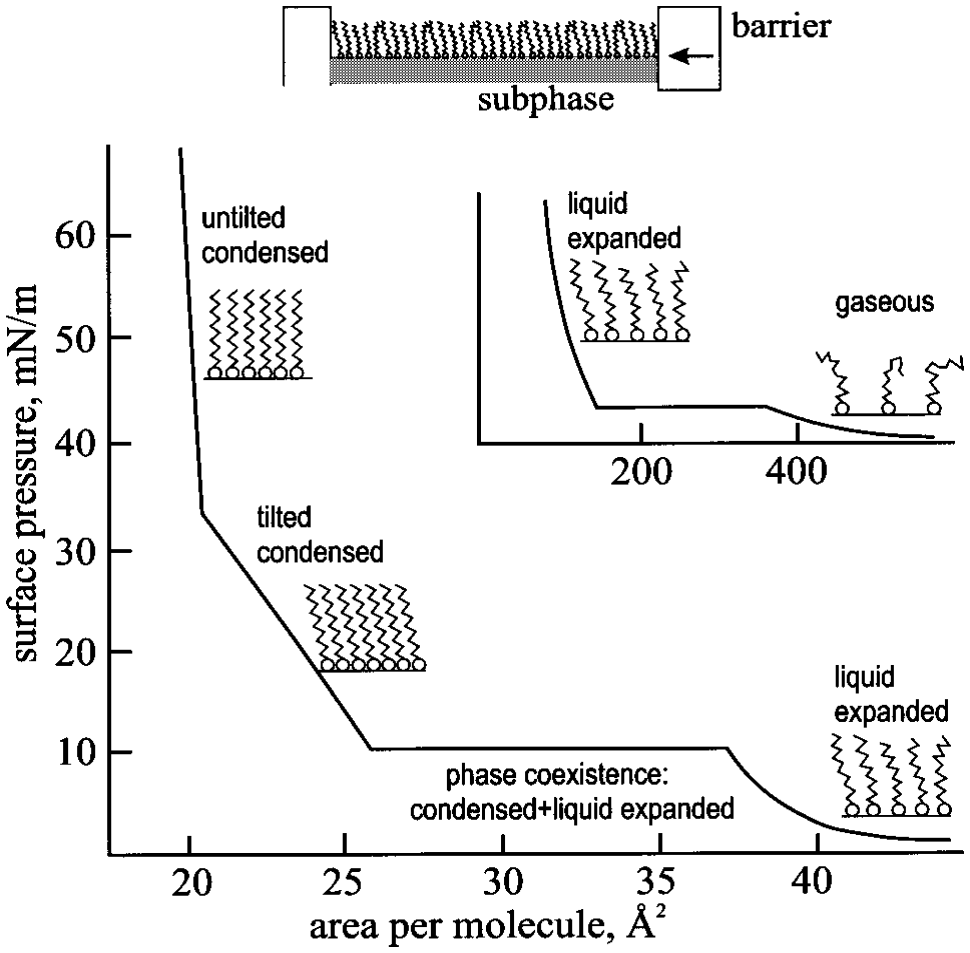

Figure 2.2 A schematic diagram of a Langmuir trough (top) and a generalized isotherm of a Langmuir monolayer.[80]

As in the 3-D phase diagrams of gaseous and condensed matter, the 2-D Langmuir monolayers can also undergo phase changes as a function of temperature and surface pressure. The chemical nature of the amphiphilic molecules dictates the magnitude of the forces acting in a monolayer, for instance, dispersive (van der Waals) interactions between the nonpolar alkyl chains, electrostatic (coulombic) repulsive interactions between the polar headgroups as well as other types of interactions like hydrogen bonding between the polar head group and water molecules from the subphase. The interplay between these forces, ultimately determines the shape of the π-A isotherm and phase diagram. Hence, the surface pressure is the result of many different forces at the air/water interface:

$$\pi = \pi_{kin} + \pi_{disp} + \pi_{elec} + \pi_{other}, \tag{2.24}$$

where π_{kin}, π_{disp}, π_{elec} and π_{other} correspond to the pressure due to kinetic forces, dispersive (van der Waals) forces between the alkyl chains of the molecules and the electrostatic (charge-charge repulsion) forces, and all other remaining forces (steric, hydrogen bonding, etc.), respectively.

Gaseous Phase

In a typical experiment with Langmuir monolayers, the surfactant molecules spread on the liquid subphase are usually in the gas (G) phase, where molecules in the monolayer are far apart from each other such that the van der Waals forces (i.e. alkyl-alkyl interactions) are negligible. The electrostatic interactions between headgroups are

also absent. However, there is sufficient interaction between the polar head group and the subphase to make the monolayer non-volatile and insoluble. The molecules in the gas phase have an average kinetic energy, $\frac{1}{2}\ k_B T$ for each degree of freedom, where k_B is the Boltzmann constant. The gaseous monolayers usually obey a 2-D version of the ideal gas equation of state[75]

$$\pi A = k_B T. \tag{2.25}$$

where *A* is the mean molecular area.

Liquid Phases

At moderate surface pressures Langmuir monolayers can have two different types of liquid phases, namely the liquid-expanded (LE) and the liquid-condensed (LC) phases. As the trough barriers are compressed, the molecules in the monolayer are brought closer to each other resulting in increased interactions between the alkyl chains, while the interactions between the headgroups remain negligible; this corresponds to the LE phase. At the onset of the LE transition, a lift off on the isotherm is observed; this phase has a relativity high compressibility.

Further compression along the π-*A* isotherm then leads to the appearance of the LC phase where there is greater alkyl-alkyl chains interactions and a reduction in compressibility. Typically, in this phase, the alkyl chains are relatively well-ordered and almost upright. The lipid monolayers in the liquid states usually obey van der Waals-like equation of state[75]

$$\left(\pi - \pi_{disp}(A_0)\right)(A - A_0) = k_B T, \tag{2.26}$$

where $A_0 = \pi d^2/2$ is twice the area defined by the distance, d, of closest approach.

Coexistence Phase and Phase Transitions

The coexistence phase in the π-A isotherm is illustrated by a horizontal plateau, where the LE and LC phases are in equilibrium with one another. Physically when two phases are in equilibrium with each other the Gibbs free energy for both phases are equal to zero, this transition is called a first-order phase transition. In a 2-D system the density of the lipids of the two phases are different from one another, the coexistence region therefore has a density that is intermediate between the two phases. The onset of the LE/LC phase is represented by a sharp transition (kink) in the π-A isotherm. This transition results in no change in the Gibbs free energy, however there is a change in the enthalpy and the mean molecular area which are indicated by the change of the slopes of the chemical potentials of the different phases on either side of the transition.

According to Ehrenfest classification, a transition for which the first derivative of the chemical potential with respect to temperature is discontinuous is classified as a first-order phase transition.[87]. A second-order phase transition is one in which the first derivative of the chemical potential with respect to temperature is continuous but its second derivative is discontinuous.[87]

Solid Phase

In a solid-condensed (SC) film where π_c is the collapse pressure, the molecules are strongly interacting via van der Waals forces between the chains, steric forces between the headgroups, and hydrogen bonding between the polar group and the subphase. In this phase, the alkyl chains and headgroups are highly oriented and are not easily compressed. SC monolayers obey an equation of state of the form:[75]

$$a\pi = b - A, \tag{2.27}$$

where *a* and *b* are constants.

Collapse Phase

As a monolayer is compressed the insoluble film will eventually reach a limiting molecular area beyond which it can no longer be compressed. The monolayer can then (i) fracture and break, (ii) buckle at constant area, or (iii) lose material. The propensity of a monolayer to reach these particular attributes are dependent on the elastic and solubility properties of the monolayer.[88] The information that is obtained by the collapse surface pressure in fact not only determines the minimum surface pressure achieved by a particular monolayer but also the mechanism by which a monolayer collapses. The collapse mechanism also determines what fraction of the monolayer remains at the interface and also how the monolayer respreads after there is a decrease in the surface pressure.

2.2 Lipid Domain Size and Shape

Domain morphology in phospholipid monolayers has been a topic of intensive research for almost three decades. The interest in domain morphology began with the optical investigation of lipid monolayers in the coexistence region. For many years, the non-horizontality in the plateau region of isotherms and, in turn, the existence of a true coexistence region was strongly debated.[89-91] This issue however was later resolved with the application of fluorescence microscopy and later on with BAM which demonstrated domains in the coexistence region.[56, 92]

The domain shapes that are observed in the coexistence regions of phospholipids below their transition temperatures are not random but are indeed governed by intermolecular interactions between the lipid molecules. These interactions are the line tension, electrostatic repulsion and the local molecular chirality of the molecule.[93] However in this thesis attention will be focused mainly on the first two energy contributions.

The energy-dependent shape of a lipid domain is mainly determined by the competition between the line tension energy (F_{φ}) and electrostatic (dipolar) repulsion energy (F_e). The overall free energy that determines the overall shape of a domain is therefore:[70]

$$F = F_{\varphi} + F_e, \tag{2.28}$$

where the line tension energy (interfacial free energy) is given by

$$F_{\varphi} = 2\varphi l, \tag{2.29}$$

and where φ corresponds to the line tension and l to the perimeter of the domain. Line tension is defined as the free energy per unit length of a boundary between coexisting phases in quasi 2-D molecular systems, it is also a 2-D analog of surface tension which is (3-D).[94] The line tension is the result of the cohesion forces between the lipid molecules. The molecular interaction between the lipid molecules that determines the line tension interaction is the length of the alkyl chain as longer chains have greater van der Waals forces. Line tension therefore favors circular domains as this reduces the perimeter of the domain and therefore the line tension energy.

The electrostatic free energy of an isolated domain is: [70]

$$F_e = \frac{1}{2}\,\tau^2 \iint |r - r'|^{-3}\, dA\, dA', \tag{2.30}$$

where r - r' corresponds to the distance between points within the domain and $\tau = \tau_{LC} - \tau_{LE}$ corresponds to the dipole density difference between solid (LC) and fluid (LE) phases, dA is the area within the LE phase and dA' is the area outside of the LC area. Each lipid molecule carries a small net dipole moment resulting from the dipole moments from the alkyl chains, headgroups as well as from polarized water molecules in their vicinity. Therefore, a lipid monolayer can be viewed as an array of dipoles at the interface.[70]

To explain the net dipole moment from a lipid molecule all contributions will be briefly discussed. The hydrophobic section of the lipid has a very small dipole moment on the terminal methyl and the carbonyl end groups.[95] The dipole moments in the hydrophilic region of the molecule are much larger than the dipole moments of the hydrophobic tails, however in a monolayer they are dominated by the smaller dipole moments in the hydrophobic tails.[95] One reason for this observation lies in the fact that the headgroup region is embedded in a medium with a higher dieletric constant than the acyl chains. Another reason for this discrepancy is due to the fact that the dipole moments of the headgroup at the air/water interface are aligned in such a way that the in-plane components and their image dipoles are aligned while their normal components cancel each other. In a monolayer, there can be misalignment between neighboring molecules with respect to azimuthal orientation hence the contribution to electrostatic repulsion will be small. The acyl chain dipole moments have normal components that are collinear while their in-plane components oppose each other, hence the net dipole moment from the hydrophobic part of the molecule are dominated by the normal components have which will have a larger contribution to electrostatic repulsion.

In a monolayer the molecular orientation of lipid molecules will impact the shape of the domains in a coexistence region. Lipid molecules that are parallel and highly aligned to the surface normal are more repulsive. These interactions are therefore repulsive in the LC region and can therefore be reduced by the elongation of the domain structure increasing the perimeter of the domain.[74] This process however, does not continue indefinitely as this will result in the breaking of the domain structure into

smaller pieces, hence elongation is eventually stopped by increasing interfacial free energy.[74]

When a monolayer is compressed in the coexistence region the domains formed are not in equilibrium and therefore their sizes change upon further compression. This can be seen because of the increase in area of the domains. If a domain starts off with a circular-like shaped as in observed (Fig. 2.3) the domain reaches a critical area where it is no longer stable. The domain will then transition into another shape that may be branched.

Figure 2.3 A schematic diagram of a change in domain shape as area is increased

2.3 Nucleation theory

Nucleation involves the process of creating a nucleus (more dense) in the presence of the bulk phase (less dense), these conditions can only take place in the first-order phase transition region. Nucleation plays a very important role in determining whether processes like condensation, precipitation, crystallization, sublimation can occur.[96] The nucleation process is initiated by random fluctuations which are able to overcome the energy barrier for the phase transition; once this barrier has been overcome

the growth process become energetically more favorable. Nucleation can take place in the presence or absence of foreign matter. Homogenous nucleation can occur without the presence of foreign matter in a supersaturated system while heterogeneous nucleation occurs in the presence of foreign matter, however only the former will be discussed here. According to the nucleation theory there are certain situations in which this theory cannot be applied, for instance if the critical nucleus is too small (20-50 molecules), or the molecules are too polar.[97]

Before the critical area (start of LE-LC coexistence region) is reached in an isotherm, the monolayer is homogenous. When the critical area is reached, the system becomes heterogeneous with the formation of a denser phase and a 1-D interface. The energy difference between these two processes determines if a stable nucleus can be formed. If the energy required to create an interface is larger than the energy released by the creation of the dense phase, nucleation will not occur.

The equation that determines if nucleation can take place in 2-D is [98-99]

$$\Delta G = -n\Delta\mu + 2\pi r\varphi, \tag{2.31}$$

where n corresponds to the number of molecules in the domain, $\Delta\mu$ corresponds to the difference between the chemical potential between the two phases, r is the radius of the domain and φ is the line tension between the two phases. The nucleation process is therefore affected by the relative magnitude of the line tension, and the chemical potential difference.[98]

The line tension between the two phases is as previously mentioned dependent on the temperature. For instance in monolayers, an increase in temperature reduces the line tension therefore increasing the number of nucleation sites observed. As the temperature of the monolayer approaches the main phase transition temperature, nucleation decreases until no domains are observed.[98] In regards to the compression rate, as the compression rate is increased in a monolayer, the molecules in the monolayer undergo more collisions increasing the chances of nucleation.

The conversion of the monomers (individual molecules) in a monolayer into clusters (domains) will be briefly discussed here in terms of a rate equation. In the development of the rate equation for the formation of clusters, there are certain assumptions that are made. One assumption is that the clusters observed grows and shrinks via the acquisition or loss of a single molecule. Another assumption made is that cluster-cluster collisions and cluster fission events are rare and can be ignored. Figure 2.10 shows the rate of cluster growth and evaporation. According to thermodynamics the system or monolayer is in equilibrium when the forward process matches the reverse process. An equation to explain this process is

$$\frac{dN_i}{dt} = \beta_{i-1} N_{i-1}(t) - \chi_i N_i(t) - \beta_i N_i(t) + \chi_{i+1} N_{i+1}(t), \qquad (2.32)$$

where N_i is the number concentration of clusters containing i molecules (monomers), β_i is the forward reaction rate constant for the collision of monomers with a cluster of size i and χ_i is the reverse rate constant for the evaporation of monomers.[96]

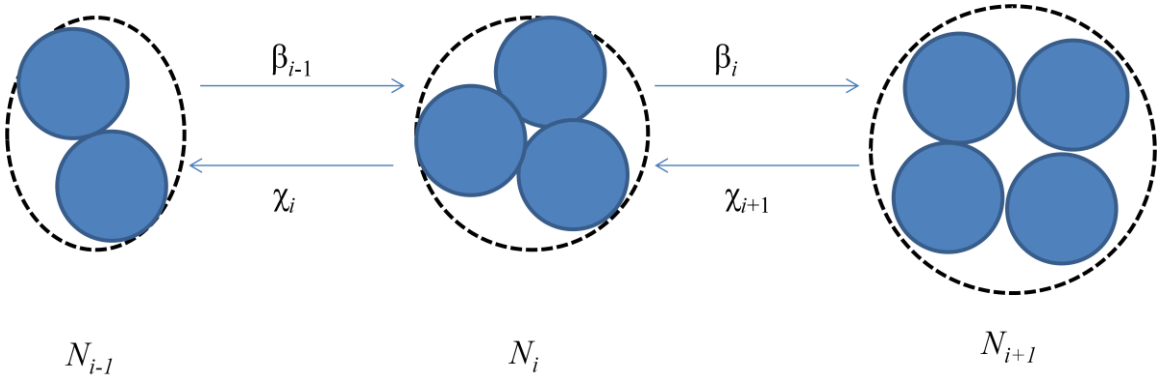

Figure 2.4 Cluster growth and evaporation processes.

The rate at which the clusters of size *i* become cluster of size *i*+1 is given by

$$J_{i+1/2} = \beta_i N_i - \chi_{i+1} N_{i+1}. \tag{2.33}$$

2.4 Surface Tensiometry Instrumentation

Surface pressure-area per molecule (π-A) isotherm measurements were performed on a film balance system with a deposition apparatus (model KSV minitrough) from KSV Instruments Ltd., Finland. The Teflon trough (176.5 mm × 85 mm) has two barriers coated with Delrin, a hydrophilic material, to symmetrically compress the monolayer on the subphase. The surface pressure and mean molecular area per molecule (MMA) were monitored during compression of the monolayer via the Wilhelmy plate technique with (Ashless Whatman) Chromatography filter paper serving as plate). The trough was thoroughly clean with ethanol and then rinsed several times with nanopure water to remove any impurities. Once clean the trough was then filled with water as the subphase, to ensure that there were no impurities to compromise the experiments that barriers were

compressed and the surface pressure monitored for increases greater than 0.1 mN/m. If the subphase had values greater than 0.1 mN/m it was discarded and replaced with more water. A measured volume of the lipid solution was then spread on the water subphase with the barriers in the expanded position, a 50 μl microsyringe (Hamilton Co., USA) was used to deposit the solution on the interface. The solvent used to deposit the lipid was then left to evaporate for a minimum of 10 minutes to leave only the lipid at the interface. The compression rate of the barrier was varied and will be discussed in further detail in the rest of this thesis. The temperature was varied with a Julabo water circulator connected to the Langmuir trough.

2.5 Brewster Angle Microscopy Theory

BAM is a non-invasive imaging technique based on the condition of minimal reflectance of *p*-polarized light at the Brewster angle obtained at the air/water interface.[100] Similar to fluorescence microscopy, this technique can provides a valuable insight into the various phase transitions that occur in insoluble monolayers at the air/water interface. However, unlike fluorescence microscopy, it does not require the use of a probe molecule to obtain imaging contrast.

In the following sections, a brief outline of the principles and theory involved in BAM imaging will be discussed. Emphasis will be placed on describing basic notions of reflection and refraction laws, Brewster angle, Fresnel reflection coefficients, and reflectance.

2.5.1 Plane Harmonic Electromagnetic Wave

Light refers to the electromagnetic (EM) radiation at a given wavelength λ emitted (in the far-field) by moving charges. As it propagates in a medium, this EM radiation behaves as a wave composed of both electric (**E**) and magnetic (**H**) fields, which stand in a fixed ratio of intensity to each other, and oscillate in phase perpendicular to each other and perpendicular to the direction of propagation given by the wave vector (**k**).[101] Figure 2.5 depicts the electric and magnetic fields associated with an EM wave.

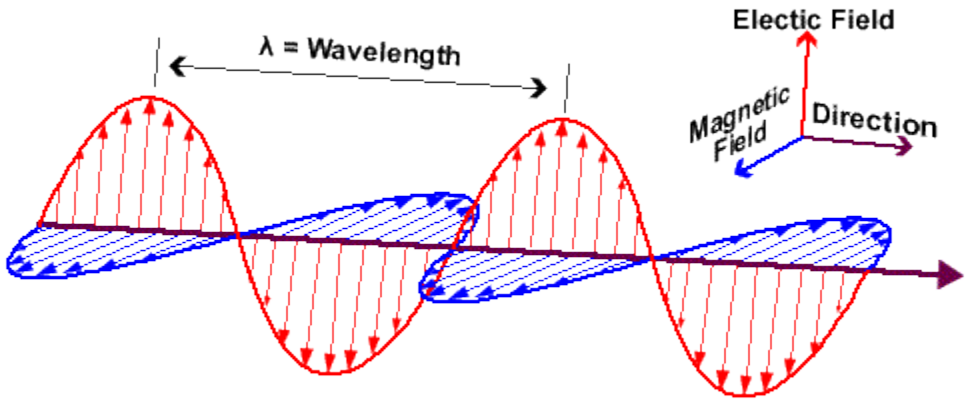

Figure 2.5 Schematic representation of an EM wave.[102]

The simplest description of an EM wave is that of a plane harmonic wave for which the **E** field varies sinusoidally in time and is uniform across all planes that are perpendicular to **k**. In other terms, it can be thought of as a series of infinite sheets of uniform **E** field moving in the direction of **k**. Formally, this can simply be written as

$$\mathbf{E}(\mathbf{r}, t) = \mathbf{E}_0 e^{i(\mathbf{k}\cdot\mathbf{r}-\omega t)}, \quad (2.34)$$

where $\mathbf{E}_0$ and ω represents the (vectorial) amplitude and the frequency of the **E** field. The direction of propagation of this (travelling) wave is given by the scalar product between **k** and **r**, the position vector.

For the remainder of this chapter, it will be assumed that the plane EM wave is propagating in an isotropic medium, i.e., a medium which is homogeneous, linear and non-conducting (or dielectric) and whose refractive index (*n*) does not depend upon its direction of propagation. In addition, it will be assumed that the amplitude of the **E** field is not too intense such that the polarization in the medium oscillates at the same frequency (linear regime).[103]

2.5.2 Polarization States

Figure 2.6 illustrates the different polarization states the an EM wave can have. In optics, the direction of the electric field is used to designate the direction of polarization of the EM wave.[103-104] In an isotropic media, an **E** field with a given polarization state can be broken down into two arbitrary orthogonal polarization components (e.g. $\mathbf{E}_u$ and $\mathbf{E}_v$), each containing the individual phase information for the specified direction. For simplicity, these components are usually set along rectangular axes (e.g. $\mathbf{E}_x$ and $\mathbf{E}_y$) or along directions parallel and perpendicular to the plane of incidence (e.g. $\mathbf{E}_p$ and $\mathbf{E}_s$) respectively. In the latter case, these components are referred to as *p*- and *s*-polarized

components, respectively. Depending on the magnitude and relative phase between of each of these components, the **E** field can adopt different polarization states.[105] For instance, if one of the components is zero ($E_{0u} = 0$ or $E_{0v} = 0$), the **E** field oscillation is restricted into one plane, under this condition one has a linearly polarized light. However, if the two orthogonal polarizations components have equal non-zero magnitude ($E_{0u} = E_{0v}$) but relative phase difference of 90^{o}, then the **E** field oscillation is varying with time and will described a circular trajectory in space. In this case, one speaks of circular polarized light. Finally, in the case polarization components with different amplitudes ($E_{0u} \neq E_{0v}$) and also different relative phase, the magnitude and direction of the **E** field will also vary with time and follow an elliptical trajectory.

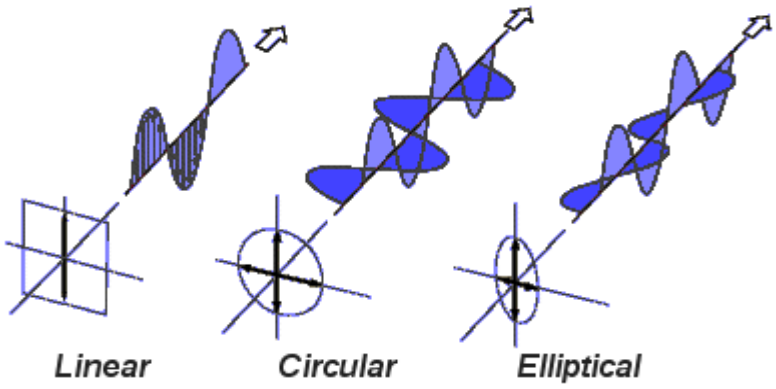

Figure 2.6 Different polarization states of an EM wave.[106]

When a plane harmonic EM wave propagates from one isotropic medium to another both reflection and refraction can take place.[103] Figure 2.7 illustrates a plane harmonic wave impinging at an incident angle θ_{1i} upon a plane interface separating two different isotropic media M_1 and M_2 with refractive indices n_1 and n_2 ($n_1 < n_2$),

respectively. At the point of contact on the boundary, the plane harmonic wave generates a wave reflected at an angle θ_{1r} in M_1 and another transmitted (or refracted) at an angle θ_{2t} in M_2. The expressions of the **E** fields of these three waves are given by

$$\mathbf{E}_{1i}(\mathbf{r},t) = \mathbf{E}_{1i0}e^{i(\mathbf{k}_{1i}\cdot\mathbf{r}-\omega t)}, \quad (2.35)$$
$$\mathbf{E}_{1r}(\mathbf{r},t) = \mathbf{E}_{1r0}e^{i(\mathbf{k}_{1r}\cdot\mathbf{r}-\omega t)}, \quad (2.36)$$
$$\mathbf{E}_{2t}(\mathbf{r},t) = \mathbf{E}_{2t0}e^{i(\mathbf{k}_{2t}\cdot\mathbf{r}-\omega t)}, \quad (2.37)$$

with

$$\mathbf{k}_{1i} = \mathbf{k}_{1i,y} + \mathbf{k}_{1i,z} = k_{1i}(\sin\theta_{1i}\hat{\mathbf{y}} - \sin\theta_{1i}\hat{\mathbf{z}}), \quad (2.38)$$
$$\mathbf{k}_{1r} = \mathbf{k}_{1r,y} + \mathbf{k}_{1r,z} = k_{1r}(\sin\theta_{1r}\hat{\mathbf{y}} + \sin\theta_{1r}\hat{\mathbf{z}}), \quad (2.39)$$
$$\mathbf{k}_{2t} = \mathbf{k}_{2t,y} + \mathbf{k}_{2t,z} = k_{2t}(\sin\theta_{2t}\hat{\mathbf{y}} - \sin\theta_{2t}\hat{\mathbf{z}}), \quad (2.40)$$

where $\mathbf{E}_{\alpha 0}$, and $\mathbf{k}_{\alpha}$, (α: *i*, *r*, *t*) are the amplitude and wave vectors of the incident, reflected and transmitted plane harmonic EM waves in the various media, respectively.

The plane of incidence in Fig. 2.7 is in the *yOz* plane and the normal to the interface is along the *Oz*-axis. Each of the **E** field vectors (incident, reflected, and transmitted) can then be decomposed into *p*- and *s*-polarized components.

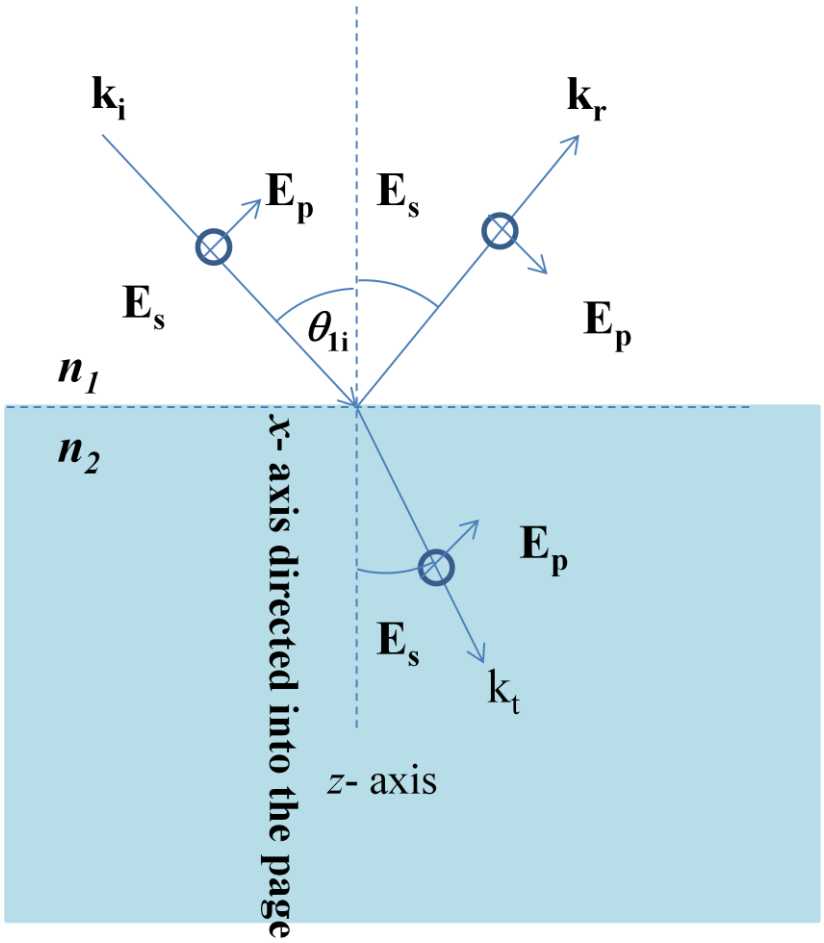

Figure 2.7 Reflection and transmission of a plane harmonic EM wave at the boundary of two isotropic media.

According to Maxwell equations, the tangential components (i.e. along the *Oy* axis) of the **E** fields must be continuous at the boundary:

$$\mathbf{E}_{1\mathrm{i},y}(y,t) + \mathbf{E}_{1\mathrm{r},y}(y,t) = \mathbf{E}_{2\mathrm{t},y}(y,t), \tag{2.41}$$

or

$$E_{1\mathrm{i}0,y}e^{i(k_{1\mathrm{i}}\sin\theta_{1\mathrm{i}}-\omega t)} + E_{1\mathrm{r}0,y}e^{i(k_{1\mathrm{r}}\sin\theta_{1\mathrm{r}}-\omega t)} = E_{2\mathrm{t}0,y}e^{i(k_{2\mathrm{t}}\sin\theta_{2\mathrm{t}}-\omega t)}. \tag{2.42}$$

A constant relationship can exist for all the points of the boundary and for all the values of *t*, if all arguments of the three exponential functions are equal at the boundary:

$$k_{1\mathrm{i}}\sin\theta_{1\mathrm{i}} = k_{1\mathrm{r}}\sin\theta_{1\mathrm{r}} = k_{2\mathrm{t}}\sin\theta_{2\mathrm{t}}. \tag{2.43}$$

Since both the incident and the reflected waves are in the same medium (M_1) as a result their wave vectors have the same magnitude ($k_{1\mathrm{i}} = k_{1\mathrm{r}}$) and the first part of Eq. (2.43) reduces to

$$\theta_{1\mathrm{i}} = \theta_{1\mathrm{r}}. \tag{2.44}$$

This is Snell's first law or reflection law.

If one then looks at the relationship between the incident and transmitted waves, one has that

$$\frac{k_{2\mathrm{t}}}{k_{1\mathrm{i}}} = \frac{n_2}{n_1} = \frac{\sin\theta_{1\mathrm{i}}}{\sin\theta_{2\mathrm{t}}}, \tag{2.45}$$

or

$$n_1\sin\theta_{1\mathrm{i}} = n_2\sin\theta_{2\mathrm{t}}. \tag{2.46}$$

This is Snell's second law or refraction law.

2.5.3 Fresnel Coefficients

The relationship between the amplitudes of the reflected and transmitted waves to that of the incident wave at a single interface are given by the Fresnel coefficients:[103]

$$r_{12}^{p}(\theta_{1i}) = \frac{E_{1r0}^{p}}{E_{1i0}^{p}} = -\frac{\tan(\theta_{1i}-\theta_{2t})}{\tan(\theta_{1i}+\theta_{2t})}, \tag{2.47}$$

$$r_{12}^{s}(\theta_{1i}) = \frac{E_{1r0}^{s}}{E_{1i0}^{s}} = -\frac{\sin(\theta_{1i}-\theta_{2t})}{\sin(\theta_{1i}+\theta_{2t})}, \tag{2.48}$$

and

$$t_{12}^{p}(\theta_{1i}) = \frac{E_{1t0}^{p}}{E_{1i0}^{p}} = \frac{2\cos\theta_{1i}\sin\theta_{2t}}{\sin(\theta_{1i}+\theta_{2t})\cos(\theta_{1i}+\theta_{2t})}, \tag{2.49}$$

$$t_{12}^{s}(\theta_{1i}) = \frac{E_{1t0}^{s}}{E_{1i0}^{s}} = \frac{2\cos\theta_{1i}\sin\theta_{2t}}{\sin(\theta_{1i}+\theta_{2t})}, \tag{2.50}$$

where $r_{12}{}^{\alpha}$ and $t_{12}{}^{\alpha}$ ($\alpha: p, s$) are the *p*- and *s*-polarized Fresnel reflection and transmission coefficients. The angle θ_{2t} is calculated through Eq. (2.46).

The reflectance is defined as the fraction of the incident light intensity that is reflected. For *p*- and *s*-polarized light, these are given in terms of Fresnel coefficients as

$$R_{12}^{\alpha}(\theta_{1i}) = \frac{I_r^{(12)}}{I_i} = |r_{12}^{\alpha}(\theta_{1i})|^2 \quad (\alpha: p, s), \tag{2.51}$$

where $I_r{}^{(12)}$ is the intensity of the light reflected from the single interface. Upon inspection of Eqs. (2.47) and (2.48), it can be seen that the amount incident light which is refracted or reflected is dependent upon the angle of incidence as well as the polarization of the **E** field. For example, Fig. 2.8 illustrates the change in reflectance at the air/water interface as the angle of incidence changes with respect to the polarization of the light.

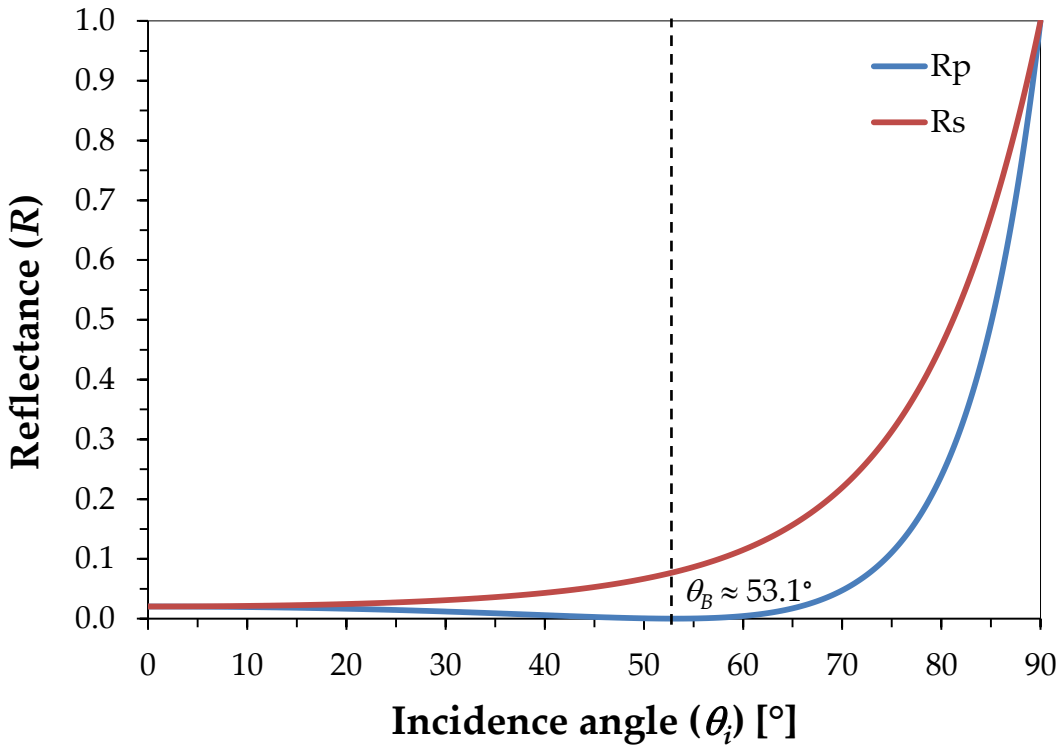

Figure 2.8 *p*- and *s*-polarized reflectances at the air/water interface (n_1 = 1.00, n_2 = 1.33 at λ = 633 nm). (courtesy of Dr. Dominique Verreault).

For a two-interface system constituted by an intermediary layer M_2 of refractive index n_2 and thickness d_2 embedded between two isotropic media M_1 and M_3 (e.g. a lipid monolayer spread at the air/water interface), one also needs to take into account the multiple reflections of the transmitted EM wave in the intermediate layer. In this case, it can be shown that the overall Fresnel reflection coefficients for this layered system are given by[103]

$$r^{\alpha}_{123}(\theta_{1i}) = \frac{E^{\alpha}_{1r0}}{E^{\alpha}_{1i0}} = \frac{r^{\alpha}_{12}+r^{\alpha}_{23}e^{2i\delta_2}}{1+r^{\alpha}_{12}r^{\alpha}_{23}e^{2i\delta_2}} \quad (\alpha: p, s), \tag{2.52}$$

and the overall reflectance by

$$R_{123}^{\alpha}(\theta_{1\mathrm{i}}) = \frac{I_{\mathrm{r}}^{(123)}}{I_{\mathrm{i}}} = |r_{123}^{\alpha}(\theta_{1\mathrm{i}})|^2 \quad (\alpha: p, s), \tag{2.53}$$

with the phase difference induced by the multiple reflections defined as

$$\delta_2 = 2\pi \frac{d_2}{\lambda} \cos\theta_2 = 2\pi \frac{d_2}{\lambda} \left(n_2^2 - n_1^2 \sin^2\theta_1\right)^{1/2}, \tag{2.54}$$

where $I_{\mathrm{r}}^{(123)}$ is the intensity of the light reflected from the layered two-interface system. For very thin films ($d_2 << \lambda$), the interference effect in the layer can be neglected ($e^{2i\delta_2} \rightarrow 1$).

2.5.4 Brewster Angle

In Fig. 2.8, the curves of $R_{12}{}^{p}$ go to zero at a certain angle, which basically corresponds to a no-reflection condition for the *p*-polarized light. By taking a second look at Eq. (2.47), one notes that

$$R_{12}^{p}(\theta_{1\mathrm{i}}) = \left|\frac{\tan(\theta_{1\mathrm{i}} - \theta_{2\mathrm{t}})}{\tan(\theta_{1\mathrm{i}} + \theta_{2\mathrm{t}})}\right|^2 \rightarrow 0 \quad \text{when} \quad \theta_{1\mathrm{i}} + \theta_{1\mathrm{t}} = \frac{\pi}{2}. \tag{2.55}$$

The no-reflection condition for the *p*-polarized light is a result of the reflected and transmitted wave vectors ($\mathbf{k}_{\mathrm{r}}$ and $\mathbf{k}_{\mathrm{t}}$) being perpendicular to one another. The angle of incidence that gives rise to this condition is determined by Snell's second law:

$$n_1 \sin \theta_{1i} = n_2 \sin \left(\frac{\pi}{2} - \theta_{1i}\right) = n_2 \cos \theta_{1i}, \quad (2.56)$$

or

$$\theta_{1i,B} = \tan^{-1} \left(\frac{n_2}{n_1}\right), \quad (2.57)$$

where $\theta_{1i,B}$ is the so-called Brewster angle.

2.5.5 Factors Influencing the Intensity of the Reflected Light

The condition of zero reflectance at the Brewster angle is valid only for a perfect interface, i.e., an interface without interfacial layer and with no roughness.[107] A boundary for which this condition holds is called a Fresnel interface. The Fresnel interface is a plane interface for which the refractive index changes abruptly in going from the lower medium to the upper medium.[100] At a real interface, however, the refractive index does not change abruptly from one medium to another; the interface is not smooth and as a result one has a minimal but non-zero reflectance at the Brewster angle. For an ideal air/water interface, the Brewster angle is 53.1°. In practice, the reflectance of pure water at the Brewster angle is non-zero (hence the use of the more correct term *pseudo-Brewster angle*) but very low (1.2×10^{-8}) such that it can still be used to study monolayers (Fig 2.9a). This Brewster angle condition enables one to study monolayers adsorbed at the air/water interface because the refractive index of the surfactant monolayer is different than that of either air or water, the conditions that satisfy the Brewster's angle are now changed with the reflectance being strongly affected (Fig 2.9b) For example, for a DPPC lipid monolayer in the LE/LC coexistence phase, the

thickness of the monolayer is ~0.15 nm. and has a refractive index of ~1.4 which can increase the reflectance by a factor of 35.[100, 108] The difference in reflectance at the air/water with and without a monolayer film being present is very large and can be used as imaging contrast. The reflectance at the air/water interface is strongly dependent on the interface properties such as the molecular density and the optical anisotropy ($n_{xy} \neq n_z$) in the interfacial region.[107]

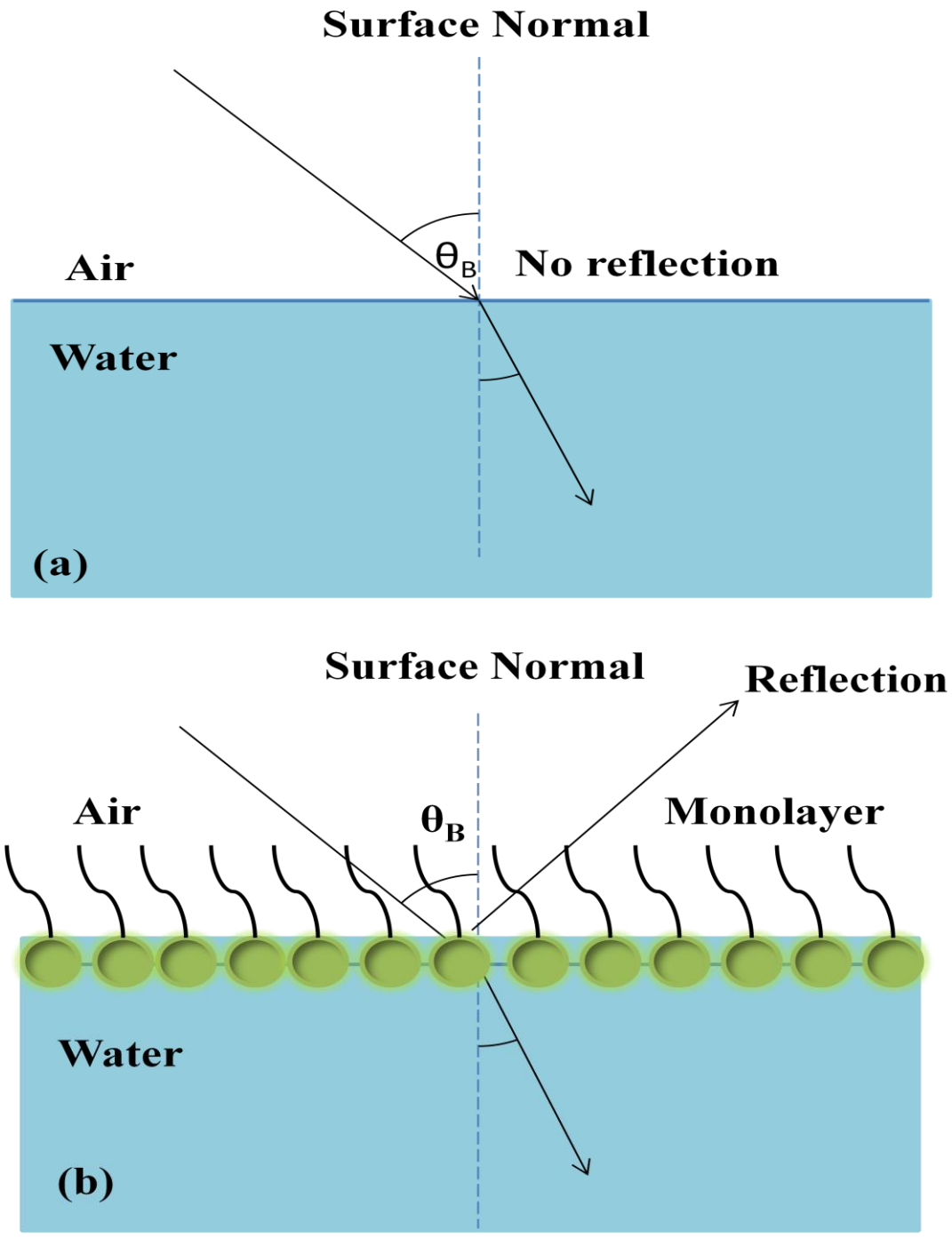

Figure 2.9 Schematic diagram of the BAM principle. In (a), water surface is illuminated with pure vertically linearly polarized light at the Brewster angle (n_{water} = 1.33). In (b), addition of monolayer film and illumination with pure vertically linearly polarized light at the Brewster angle.

2.6 Brewster Angle Microscopy Instrumentation

The BAM setup used in this work was custom-built by L. Antal (Machine Shop of the Department of Chemistry and Biochemistry, The Ohio State University) and assembled and optimized by H. Castada. It is composed of a goniometer on which an emission and detection arms are fixed, a small black cabinet encloses the setup (Fig. 2.10). The goniometer permits the angular positioning of the arms in a range from 40 to 60°. The arms support all the opto-mechanical components of the BAM setup: the laser source is found on the emission arm, while an objective lens, a tube lens, a polarizer, and a charge-coupled device (CCD) camera are found on the detection arm. Finally, a large black-coated plexiglass housing with sliding doors of easy access. The housing protects the setup against air currents and dust as well as to eliminate any external parasitic light. A black glass plate (BGP Nima black glass plate for MircoBAM) was placed to rest at the bottom of the trough before filling with water. The black glass serves to absorb the refracted beam from reaching the detector. Most of the final images taken were cropped from a 600 μm x 600 μm size to a narrow strip to show the most resolved regions of the images. No other additional image processing was done with the images. In the following sections, a brief instrumental overview of the above-mentioned opto-mechanical components will be given. For further details concerning the BAM setup, the reader is referred to the M.Sc. thesis of H. Castada.[109]

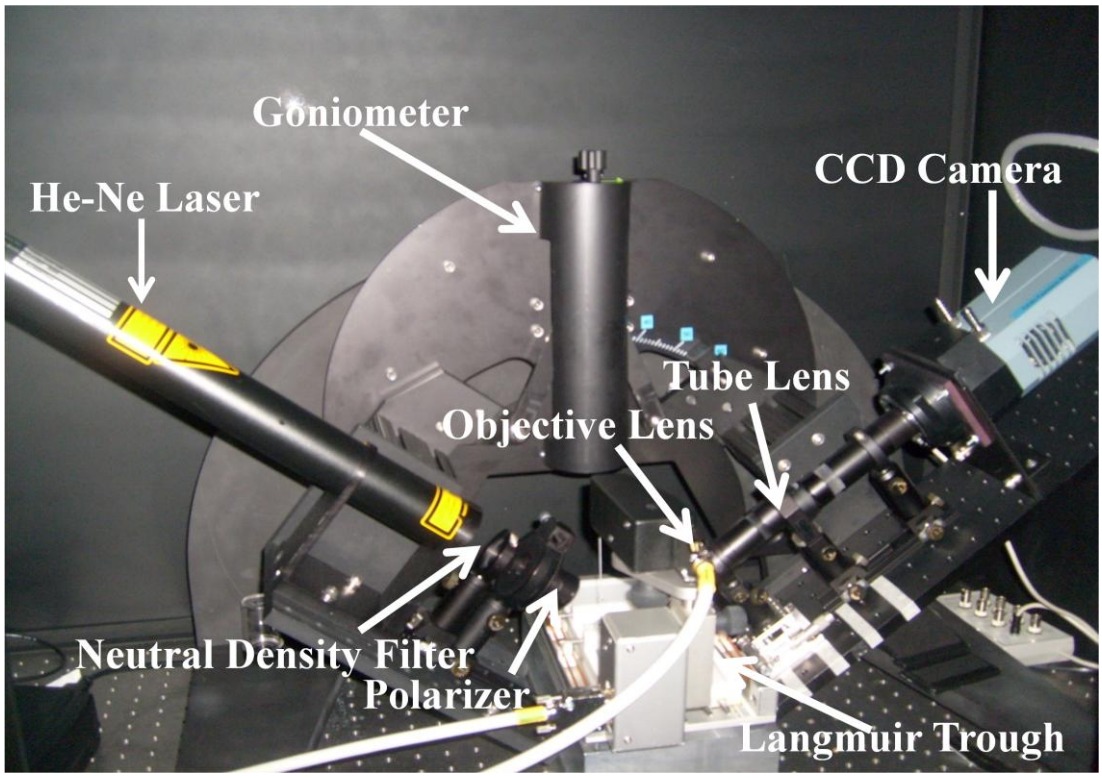

Figure 2.10 Brewster angle microscope and KSV Langmuir trough.

2.6.1 Opto-mechanical Components

He-Ne Laser Source

A He-Ne laser (Research Electro-Optics) acts as the light source for the BAM and provides a highly *p*-polarized (> 500:1) light beam at 632.8 nm wavelength with an output power of 17.0 mW.

Neutral Density Filter, Polarizer, Objective lens, and Tube Lens

The power of the output light is first attenuated by a neutral density filter CVI Melles Griot) located between the laser source and the polarizer. The highly *p*-polarized (500:1) output light from the laser source is then further filtered with a Glan-Laser calcite

polarizer (GL 10A, Thorlabs; 12 mm × 13.7 mm (W × L) with a 10 mm × 10 mm aperture, wavelength range: 350-700 nm, extinction ratio: 100000:1, damage threshold: 10 J/cm^2 @ 532 nm).

The objective lens used in the BAM setup is an infinity-corrected Nikon CF Plan EPI lens (courtesy of Dr. James Rathman of the Department of Chemical and Biomolecular Engineering, The Ohio State University). It has a working distance of 20.5 mm, "chrome-free" (CF) with a linear magnification 20×, and a numerical aperture (NA) of 0.35. The infinity-corrected lens is used with a tube lens that has a focal length of 200 mm (MXA22018 CFI; Nikon). The tube lens is needed to focus the collimated light onto the CCD.

CCD Camera

The BAM images were recorded with a back-illuminated anti-reflective CCD camera (DV 412-BV, Andor Technology, Ireland; wavelength range: 350-1000 nm) The CCD camera has 512 × 512 active pixels, each with a pixel size of 24 μm × 24 μm (W × H), thus giving an image viewing area of 12.3 mm × 12.3 mm. The image acquisition was performed with the Andor Solis software and CCI-010 PCI controller card with 16-bit 1MHz, 500KHz, 62KHz and 31KHz pixel readout rate options.

2.6.2 Alignment Procedure

The alignment of the CCD camera with the optical axis is done by placing a gold mirror is on a sample stage located between the two arms of the goniometer. The He-Ne

laser source is then turned on and the output light then passes through the neutral density filter and then the polarizer. The light then impinges and reflects on the gold mirror at the Brewster angle. The reflected light then passes through the objective and tube lens to finally reach the CCD. For optimization purposes and to avoid damaging the CCD camera, the polarizer is slightly rotated such that only a small amount of light is allowed to reach the CCD. An image can then be taken and its horizontal (*x*-axis) and vertical (*y*-axis) can then be adjusted; if the image is offset too low or too high from the center, the knob at the back of the goniometer can be used for adjustment. If the image obtained from the CCD is too much to the left or to the right of the objective lens, a Vernier micro-caliper on which the objective lens is mounted has the ability to be adjusted in both the *x* and *y* directions.

2.6.3 Image Focusing Procedure

The image focusing is done with the help of a micrometer-graduated glass ruler. The graduation lines on the ruler are separated by an equal distance of 20 μm. The stage micrometer ruler was then placed onto the sample stage on top of a black background. The Brewster angle was then adjusted to obtain a minimum reflection. Images are then taken to completely resolve the lines on the micrometer. The knob at the back of the goniometer as previously mentioned and the Vernier caliper on which the objective lens is mounted are used in this process.

2.6.4 Image Quality, Optical Artifacts, and BAM Resolution

The images obtained with the BAM setup are not without artifacts. For example, the oblique positioning of the CCD camera and objective lens relative to the surface results in proper focusing only in the middle of the image. As mentioned previously the low intensity of the reflected light due to the absence of an abrupt change in the refractive index at the interface can affect the contrast in the images observed. In addition, a small amount of scattering of the incident light beam along its trajectory resulting from defects of the optical components induces interference fringes and/or parasitic light which also decreases imaging contrast. Hence, the optics that are in the path of the incident beam must be of good quality.[100]

The BAM resolution is determined by the numerical aperture (NA) of the objective lens. Formally, the resolution (R) is defined by the simple mathematical relation

$$R = \lambda/(2NA) \tag{2.55}$$

where λ refers to the wavelength. Hence, considering an objective lens with a 20× magnification, 0.35 NA and a laser source that emits at a 633 nm wavelength, calculated BAM resolution is therefore 2.2 μm.[110]

2.6.5 BAM Imaging

To reduce the amount of light that may reach the CCD a black plate was purchased from (Biolin Scientific, Inc.). The dimensions of the glass plate are 40 mm ×

30 mm and 4 mm thickness. The black plate was laid flat at the bottom of the trough to absorb the refracted light and prevents diffraction of the laser beam and therefore minimizes the scattering of light which therefore contributes to a shaper BAM image.

3. ZWITTERIONIC PHOSPHOLIPID MONOLAYERS AT THE AIR/WATER INTERFACE WITH VARIED TEMPERATURE AND COMPRESSION RATES

DPPC and DPPE two zwitterionic phospholipids that are found in PS (Fig. 3.1). Both phospholipids have two saturated 16 carbon alkyl tails but differ with respect to the headgroup, therefore any differences in the properties between both lipids can be attributed to the headgroup. These properties include the electrostatic charge, molecular size, state of hydration, and hydrogen bonding ability between the headgroups.[111] In the coexistence region of a monolayer the domain morphology observed are a direct indication of the molecular interactions between the lipids. The differences of the domain morphology with respect to temperature and compression rate can therefore shed some insight on the intermolecular interactions between the lipids.

The main phase transition temperature is a very important parameter that is dependent on the molecular interactions of the lipid.[51] The main phase transition temperatures (gel phase to liquid crystalline phase) of the bilayers of DPPC and DPPE are 41 and 63 ^{o}C, respectively which also corresponds to the transition temperature in a monolayer.[112-114] Even though both lipids are zwitterionic, DPPE's transition temperature is significantly greater than DPPC. To explain this difference it is important to describe the types of molecular interactions between the lipids. The headgroup of DPPC has three methyl groups attached to a nitrogen atom, while DPPE has three

hydrogens, thus giving DPPC and DPPE cross-sectional areas of ~46.6 $Å^2$ and ~38 $Å^2$, respectively.[112, 115] Also at small MMAs, DPPE can exist in an untilted conformation because of the smaller headgroup unlike DPPC. DPPC exist in a tilted conformation at a low MMA to avoid the strong electrostatic repulsive interactions between the headgroups. DPPE molecules however interact via hydrogen bonding and can therefore overcome these repulsive interactions which will be explained later.[54] The smaller headgroup of DPPE also increases the van der Waals interaction between the alkyl tails.[54] Van der Waals interactions alone cannot explain the large difference in the transition temperature. It is believed that the hydrogen bonding between the phosphate and ammonium groups headgroups in DPPE are responsible for the higher transition temperature.[54, 111] In PE, each amine and phosphate can participate in two hydrogen bonds.[54] The strength of one N-H---O is approximately (8 kJ/mol), however the length of the hydrogen bond also plays a role.[116]

In relation to hydration, infrared (IR) spectroscopy has been used to investigate hydration sites of lipids and how the hydrogen bonding network is affected in the presence of different headgroups.[117-118] IR spectroscopy studies have shown that water molecules that reside at the air/water interface of polar headgroups act as hydrogen donors and form strong hydrogen bonds with the lipid phosphate and carbonyl groups.[117] Water molecules hydrate the lipid molecules and therefore reduce lipid-lipid interactions. Adsorption isotherms of PE and PC illustrated that PC has a greater affinity for water then PE.[119] It is believed that lipids participating in hydrogen bonding with each other have a lower affinity for water.[54]

The experiments presented in this chapter used a Langmuir trough coupled with a BAM to obtain isotherms and images of domain morphology from a pure insoluble monolayer of one of the lipids compressed isothermally on a pure water at pH 5.5. To understand the lipid domain morphology, three different temperatures and compression rates for each phospholipid were used. The temperatures used were 23, 32 and 37 ^{o}C for DPPC. The temperatures used in the study of DPPE were 23, 35.5 and 37.5 ^{o}C because of its higher transition temperature in a monolayer. The compression rates used in this study for both DPPC and DPPE were 3.0, 5.0, and 7.0 Å^{2}/molecule/min.

3.1 Materials

1,2-dipalmitoyl-*sn*-glycero-3-phosphocholine (DPPC), and 1,2-dipalmitoyl-*sn*-glycero-3-phosphoethanolamine (DPPE) (> 99% purity Avanti Polar Lipids, Alabaster, AL) were used without further purification. Methanol and chloroform (spectrophotometric grades) were purchased from Fisher Scientific. Nanopure water was obtained from a Barnstead Nanopure filtration system and had a resistivity of 18.3 MΩ cm and a measured pH of 5.5.The temperature was measured with an uncertainty of +/- 1 ^{o}C. To vary the temperature of the subphase a thermostated water circulator from Julabo was used.

3.2 Sample Preparation

Stock solution of DPPC with 1mM concentration was made in chloroform. Stock solution of DPPE with 1 mM concentration was made using a chloroform/methanol mixture with a 2:1 (v/v) ratio.

3.3 Results and Discussion

3.3.1 DPPC

The phase behavior of DPPC on a water subphase has been extensively studied over the years and is very well known.[113, 120-122] The compression rate used in many DPPC studies has also been varied; for instance, Weis *et al*. used a rate of 1.92 $Å^2$/molecule/min, McConlogue *et al.* used two compression rates of 0.86 and 17.2 $Å^2$/molecule/min, and Weidemann *et al.* used compression rates that were larger than 10.0 $Å^2$/molecule/min.[112, 122-123] Many of these studies illustrated that the compression rate had an impact on domain morphology.[112] Experiments in which slow compression rates are used are more susceptible to contaminants from the air as the time spent to complete data may exceed 1 hr. Fast compression rates however can yield highly unstable domains that exhibit dendritic or fractal shapes.[112] Studies have also been done to investigate the compression rate dependence of DPPC monolayers on a water subphase and its impact on the isotherm.[124] The compression rates used in this study were 3.8, 5.6, 11.9, 23.8 and 31.8 $Å^2$/molecule/min and it was determined that the shape of the isotherms were not significantly affected.[124] The compression rates used in this

study are therefore in an intermediate range with what has been done previously in the literature.

3.3.2 Surface Pressure-Area Isotherms of DPPC

Surface Pressure-Area Isotherms of DPPC monolayers at 23, 32, and 37 ^{o}C

Figure 3.2 shows the three DPPC isotherms at 23 ^{o}C at compression rates of 3.0, 5.0, and 7.0 Å^{2}/molecule/min. The following distinct phases were identified during monolayer compression (i.e. decrease in MMA): G-LE, (>96 MMA), LE (~96-78 MMA), LE-LC (~78-55 MMA), and LC (~55 MMA). The collapse phases were not shown because of the limitation associated with the trough design, however the collapse pressure is usually observed at ~72 mN/m at room temperature.[2] The three isotherms almost perfectly overlapped illustrating that the compression rate had no significant impact on the shape of the isotherm.[124] The characteristic LE-LC phase transition was found in the surface pressure range of 4.5 to 7.5 mN/m.

Figure 3.3 shows the three DPPC isotherms at 32 ^{o}C with the same compression rates used at 23 ^{o}C. The lift offs from the G-LE phase into the LE phase occurred at 98 MMA, the lift off differs by ~2 Å^{2} from those at 23 ^{o}C. The following distinct phases were identified: G-LE (>98 MMA), LE (~98-68 MMA), LE-LC (~68-55 MMA), and LC (~55 MMA) again the collapse phase was not shown in the isotherm. The LE-LC phase was found in the surface pressure range of 20 to 25 mN/m, and at a lower MMA than at 23 ^{o}C.

Figure 3.4 shows the DPPC isotherms at 37 ^{o}C with the same compression rates used at 23 and 32 ^{o}C. The following distinct phases were identified during monolayer compression: G-LE (>100 MMA), LE (~100-60 MMA), LE-LC (~60-55 MMA), LC (~55 MMA); the collapse phase also is not shown. The onset of the LE-LC coexistence region occurred at an even higher surface pressure ranging from 30-35 mN/m. The compression rate had no significant effect on the shape of the isotherms at 32 and 37 ^{o}C.

3.3.3 BAM Images of DPPC domains

BAM Images of DPPC domains at 23 ^{o}C

Figure 3.5 shows the BAM images of DPPC domains on a water subphase at 23 ^{o}C at the slowest compression rate (3.0 Å^2/molecule/min). The images shown are consistent with DPPC monolayer in the LE-LC coexistences region.[112, 122, 125] At the start of the LE-LC coexistence region the appearance of domains were observed at ~79 MMA. The bright domains corresponding to the LC phase appear to be round at the start of nucleation, however due to limits in the resolution of the microscope, their precise shape could not be definitively identified. On further compression the sizes of the domains increased as the DPPC molecules transitioned from the LE phase into the LC phase. The morphology of the domains also becomes more apparent as the size of the domains increase. At 75 MMA some the observed domains were S-shaped, tri-lobed and a few were bean-shaped with diameters of ~10 μm. According to McConlogue *et al*. the fundamental shape of DPPC is a bean, however the compression rate used in that study was very slow (0.86 Å^2/molecule/min).[122] The compression rate used here was

approximately three times greater hence the reason for fewer observed bean-shaped domains. At 73 MMA almost all of the domains were S-shaped, with a diameter of ~20 μm. At 70 MMA some of the S-shaped domains transitioned into a tri-lobed configuration but the majority of the domains kept their S-shape until fusing into the LC phase with continued compression.

Figure 3.6 shows domain formation at the intermediate compression rate (5.0 $Å^2$/molecule/min), which first appeared at ~78 MMA illustrating that the compression rate did not affect the onset of the LE-LC region. The domains at 78 MMA appeared almost circular, however at 75 MMA as the diameter of the domains increased, the domains that could be definitively identified were either S-shaped or tri-lobed. At 71 MMA most of the domains were either tri-lobed or multi-lobed with a domain diameter of ~20 μm. With continued compression most of the domains maintained either a tri-lobed or multi-lobed configuration until fusing into the LC phase.

Figure 3.7 shows domain formation at the fastest compression rate (7.0 $Å^2$/molecule/min) which first appeared at ~79 MMA. At 73 MMA multi-lobed domains can be definitively identified with an approximate diameter of 20 μm. The multi-lobed domains at the fastest compression rate have a slightly larger diameter then those at the slower rates.

As mentioned in previous studies, the fundamental shape of DPPC domains is the bean-shaped as shown by McConlogue *et al.*[122] The bean-shape configuration however was not observed as a predominate shape in the data presented here because the compression rates were not slow enough. At the fastest compression rate the domain

shapes were ~50 μm in diameter, while at the slower compression rates the diameters of the domains before fusing into the LC phase were no larger than 40 μm. It is a well known fact that the compression rate of a monolayer can have a direct impact on the domain morphology in a monolayer.[122] The increase in the diameter of the domains also corresponds to an increase in the perimeter of the domain and therefore an increase in electrostatic repulsion. As electrostatic repulsion increases, the observed domains became more multi-lobed.

The interesting array of domain shapes observed in a monolayer are as previously mentioned determined by the line tension term that favors compact circular shapes and the repulsive electrostatic term that favors elongated shapes. To determine which particular term has the greatest impact on the domain morphology, a dimensionless shape parameter is used and defined as

.

$$\Gamma = \tau^2/\varphi, \tag{3.1}$$

where τ^2 is the in-plane dipole moment density and φ the line tension.[126] From this equation, it can be deduced that as the τ^2 increases, more complex domain morphologies will become more apparent.

To explain the domain shapes observed, the effects of temperature and compression rate used must also be taken into consideration. According to classical nucleation theory, a faster compression rate is usually associated with a larger number of nucleation sites.[127-128] A similar experiment was performed with

dilauroylphosphatidylethanolamine (DLPE) to determine the impact of the compression rate and temperature on domain formation. It was observed that increasing the temperature and compression rate increased the number of nucleation sites.[129] An equation was developed to look at the number of domains formed as the temperature was varied.[129] The equation that modeled this phenomenon is given by

$$N(T) \propto e^{-\frac{c}{T}}, \tag{3.2}$$

where N is the number of domains formed, T the temperature and c is a constant. According to Eq. (3.2) the number of domains formed should increase as the temperature is increased.

An equation was also developed to determine the maximum number of nucleation sites as a function of compression rate:

$$N = N_{max}(1 - e^{k_n t}), \tag{3.3}$$

where N is the number of nucleation sites, N_{max} is the maximum number of domains that can be formed and k_n is the nucleation rate constant.[127] It can be postulated that an increase in the compression rate should yield a greater number of nucleation sites. To determine if an increase in the compression rate increased the number of domains, experiments were reproduced three times and the domains within an area of 100 × 100 μm were counted to obtain an average number of domain formed per compression rate.

Table 3.1 shows the impact of temperature and compression rate on the observed number of nucleation sites. The average number of nucleation sites observed at 23 ^{o}C with the slowest, intermediate and fastest compression rates were 11.6 ± 3.1, 10.5 ± 1.3, and 9.7 ± 2.5, respectively, the error bar readings are quoted as the standard deviation related to three measurements. Hence, within an equivalent area, there was a small reduction in the number of observed nucleation sites as the compression rate increased, a direct contradiction to what was expected. To explain this observation, closer attention was then placed on the sizes of the domains at each individual compression rate. The domains at the slowest compression rate appear to have an identical diameter of about 40 μm before fusing into the LC phase. At the intermediate compression rate, the domains appear to have a bimodal distribution in size, while at the fastest compression rate the domains have a diameter of ~50 μm. The small increase in the diameter of the domains as the compression rate increased suggest the fusion of small individual domains that are in close proximity to each other. According to the nucleation theory the number of molecules needed to form a stable nucleation site is greater than 40 molecules. A domain with a diameter of 2 μm, i.e. the resolution of the BAM, can have thousands of DPPC molecules before they can be observed with the BAM. McConlogue *et al.* in a previous experiment with DPPC monolayers at room temperature also observed multi-lobed domains when a compression rate of 17.2 Å^2/molecule/min was used. To explain the multi-lobed domains, the explanation given was the fusion of up to two mature but joined domains. The fastest compression rate used here also point towards the fusion of

domains. As a result the larger more multi-lobed domains observed at the fastest compression rate was the result of the fusion of domains.

BAM images of DPPC domains at 32 ^{o}C

Figures 3.7-3.9 show BAM images of DPPC domains in the LE-LC phase at the slowest, intermediate, and fastest compression rates, respectively. The first appearance of the domains occurred at ~65, 67 and 68 MMA for each compression rate. The domains appear circular at the onset of the coexistence region at all compression rates with an approximate diameter of 10 μm. As the monolayer was further compressed the sizes of the domains for all compression rates increased.

The number of observed nucleation sites was also counted within a 100 × 100 μm area at 32 ^{o}C for all compression rates. The average numbers of nucleation sites formed at the slowest, intermediate, and fastest compression rates were 15.6 ± 2.1, 19.3 ± 2.9, and 24 ± 3.6, while the average sizes of the domains were 35, 30 and 25 μm, respectively (Table 3.1).

The circular domains at 32 ^{o}C goes back to the molecular interactions mentioned previously (see Section 2.2) in regards to the competition between line tension and electrostatic repulsion. Both the line tension and electrostatic repulsion decrease as the temperature is increased.[94] The line tension decreases because of the weakened van der Waals interactions between the alkyl tails. Electrostatic repulsion also decreases because the alignment of the molecules within a domain is decreased. The circular domains at 32 ^{o}C indicates that line tension dominates over electrostatic repulsion.

BAM images of DPPC domains at 37 ^{o}C

Figures 3.11-3.13 show the images of DPPC domains at 37 ^{o}C at the slowest, intermediate, and fastest compression rates, respectively. The first appearance of domains was seen at ~60 MMA with the domains also appearing circular. As the domains grew in size the circular shape was maintained for all compression rates. The observed number of domains also increased as the temperature increased to 37 ^{o}C. The average numbers of nucleation sites at the slowest, intermediate, and fastest compression rates were 65.3 ± 2.3, 64.6 ± 3.1 and 62 ± 2.0, respectively (Table 3.1). The maximum diameter of the domains at all compression rates was ~15 μm. The observed number of domains for all compression rates were almost the same, therefore the compression rate did not have a significant impact. One possible reason for this observation may be that the critical number of domains that can be formed at 37 ^{o}C has been reached.

In Eq. (3.1) the number of observed nucleation sites was dependent on the temperature in which the data was collected. To express this type of relationship, an Arrhenius equation, which expresses the temperature dependence for a reaction rate can be used. In the data presented here the number of observed nucleation sites are directly proportional to the rate constant hence the ln of the number of observed nucleation sites versus 1/temperature was plotted for all three compression rates to observed if they is indeed Arrhenius (Figure 3.14). The compression rate at 3.0 Å^2/molecule/min appeared to closely follow an Arrhenius-like behavior, followed by the compression rate at 7.0 Å^2/molecule/min, then at 5.0 Å^2/molecule/min.

Table 3.1 Number of observed nucleation sites for DPPC monolayers at three temperatures and three compression rates in the π range of 4.5 to 7.5 mN/m.

Temperature [°C]	**Compression rate** [Å^2/molecule/min]		
	3.0	5.0	7.0
23	11.6 ± 3.1	10.5 ± 1.3	9.7 ± 2.5
32	15.6 ± 2.1	19.3 ± 2.9	24.0 ± 3.6
37	65.3 ± 2.3	64.6 ± 3.1	62.0 ± 2.0

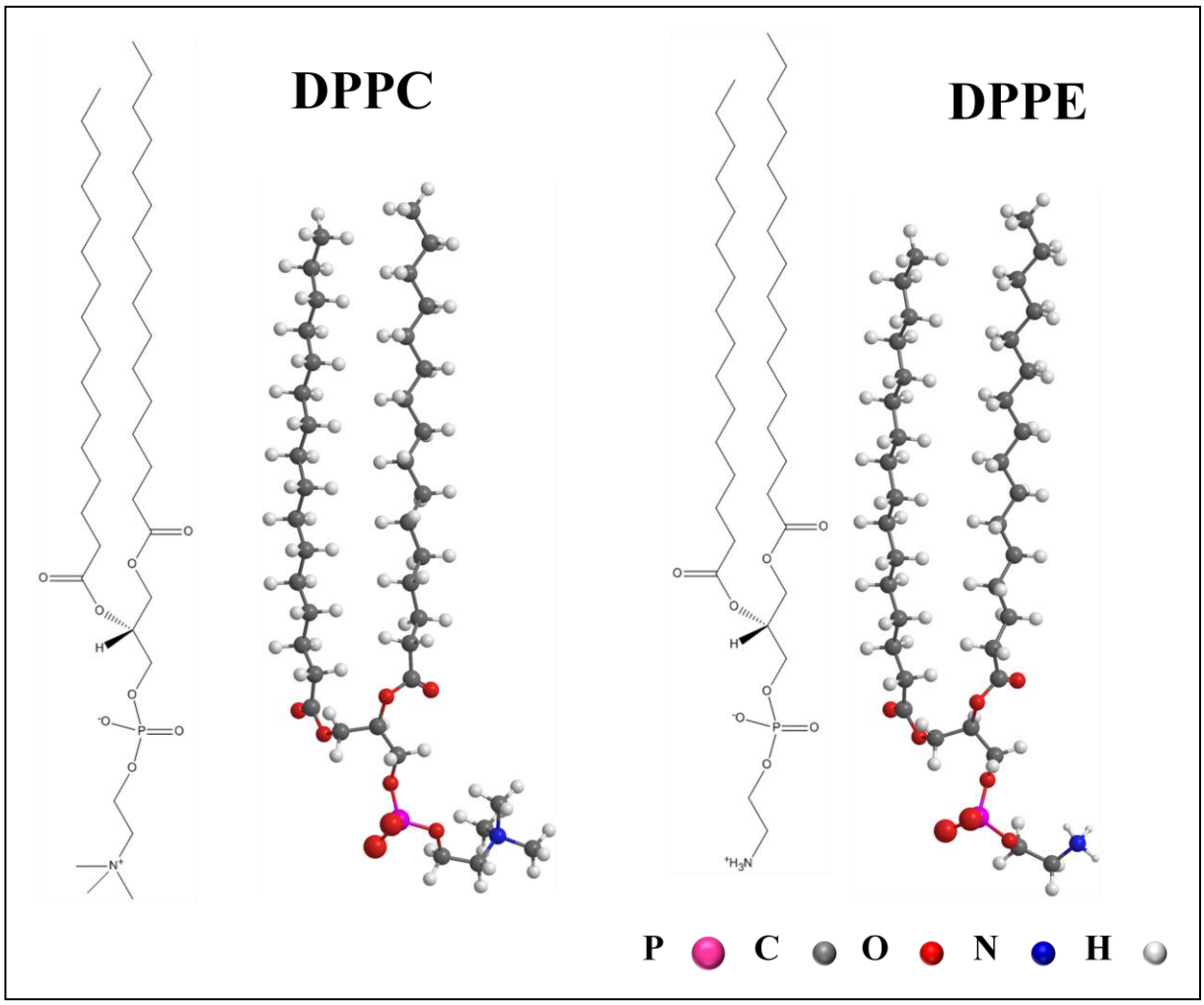

Figure 3.1 The molecular structures of DPPC and DPPE.

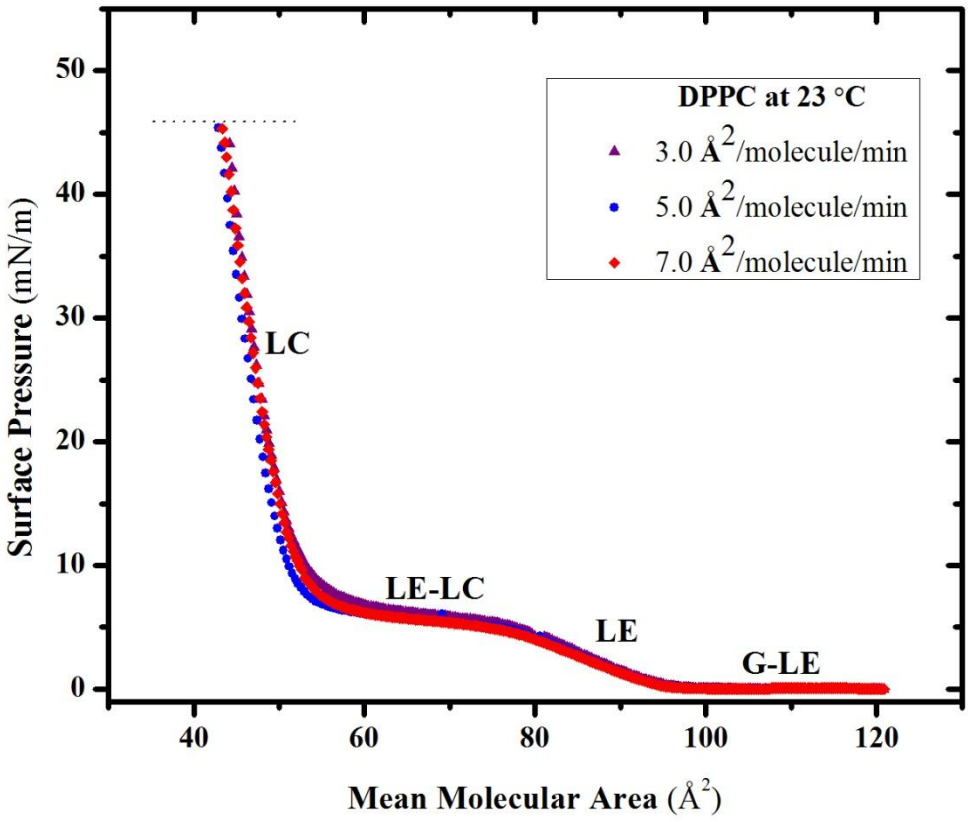

Figure 3.2 Surface pressure-area isotherms of DPPC monolayers spread on water at 23 ^{o}C and for three compression rates.

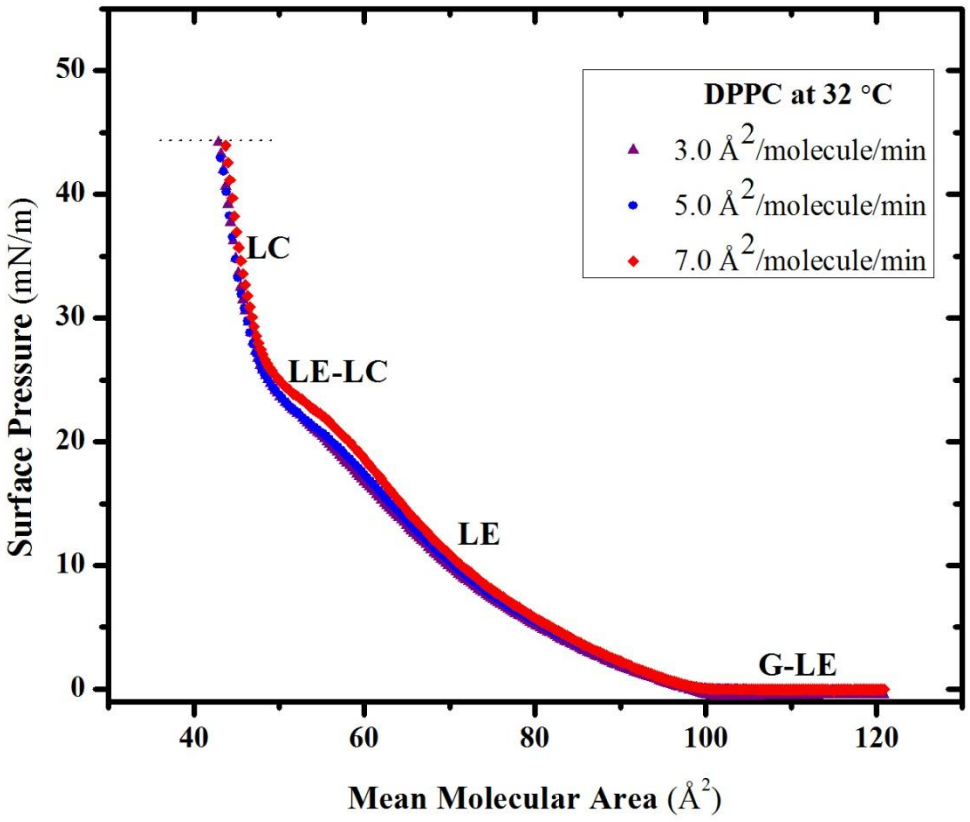

Figure 3.3 Surface pressure-area isotherms of DPPC monolayers spread on water at 32 ^{o}C and for three compression rates.

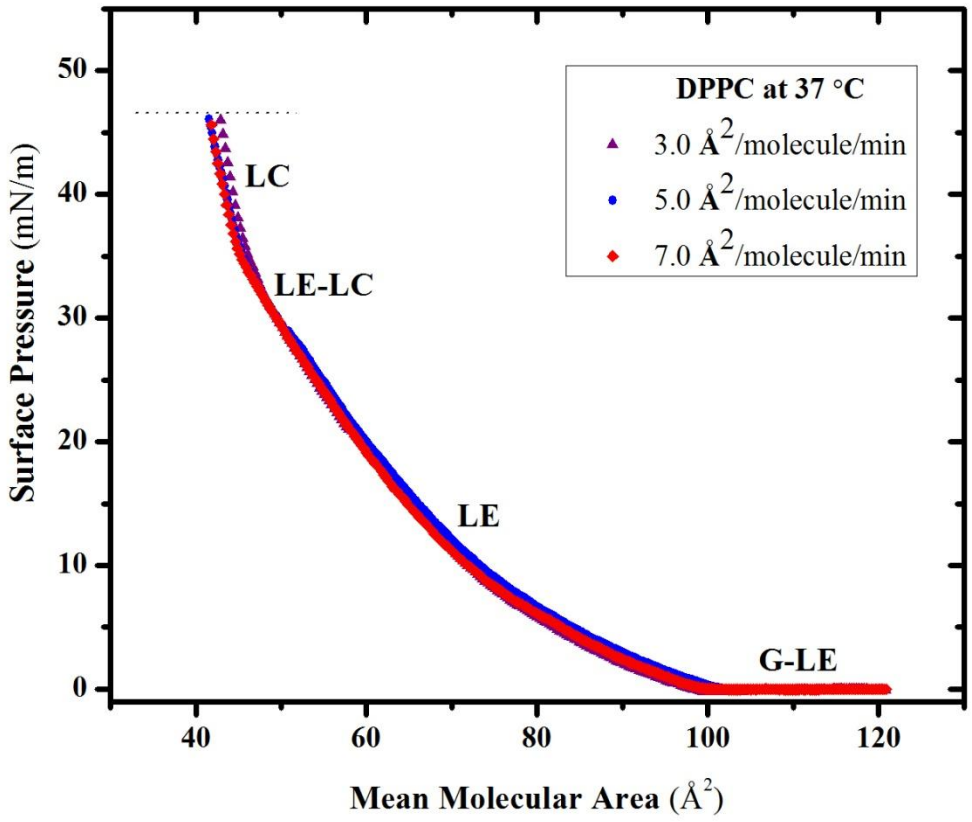

Figure 3.4 Surface pressure-area isotherms of DPPC monolayers spread on water at 37 ^{o}C and for three compression rates.

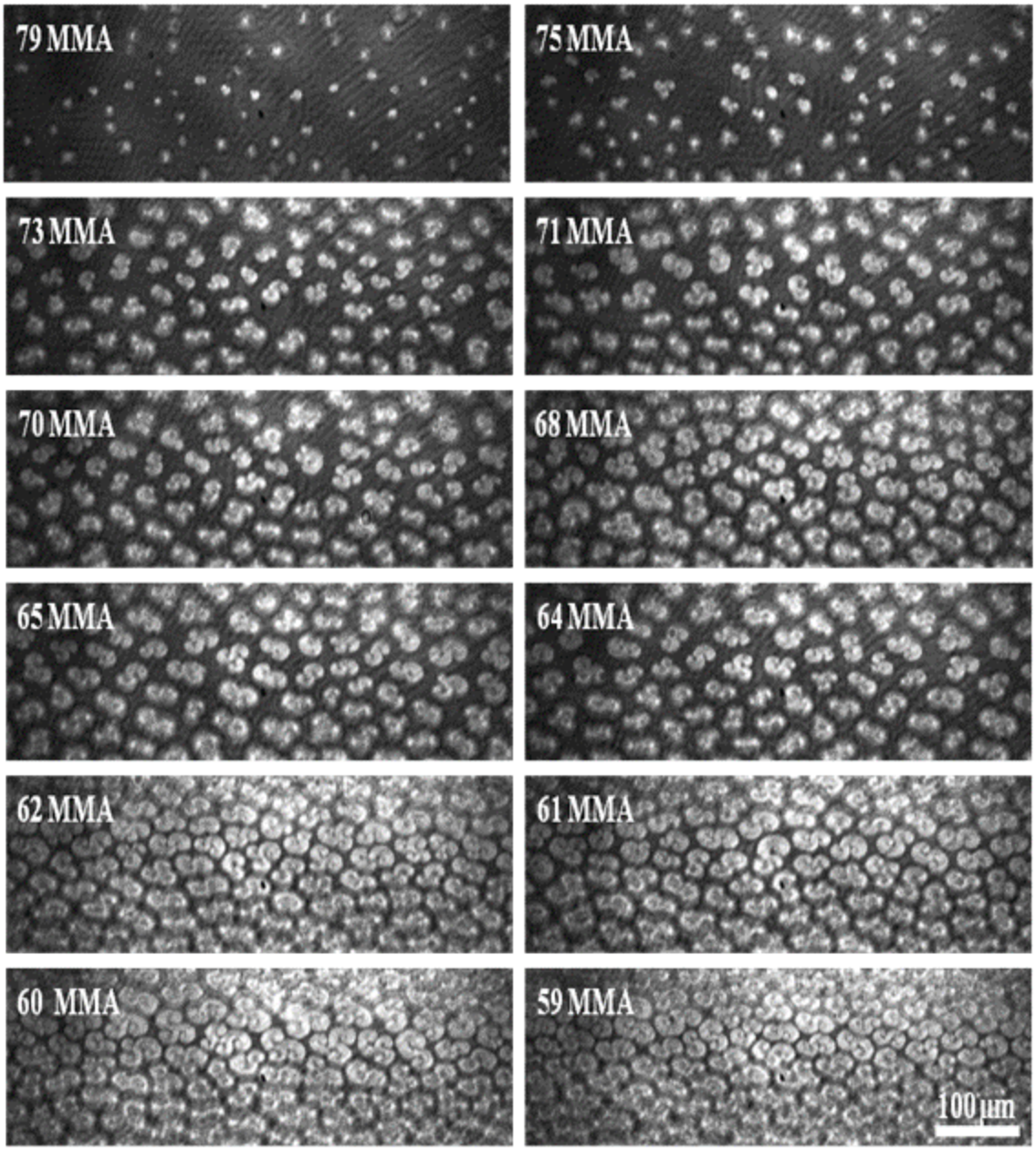

Figure 3.5 BAM images of DPPC domains formation at 23 ^{o}C and for a compression rate of 3.0 Å^{2}/molecule/min.

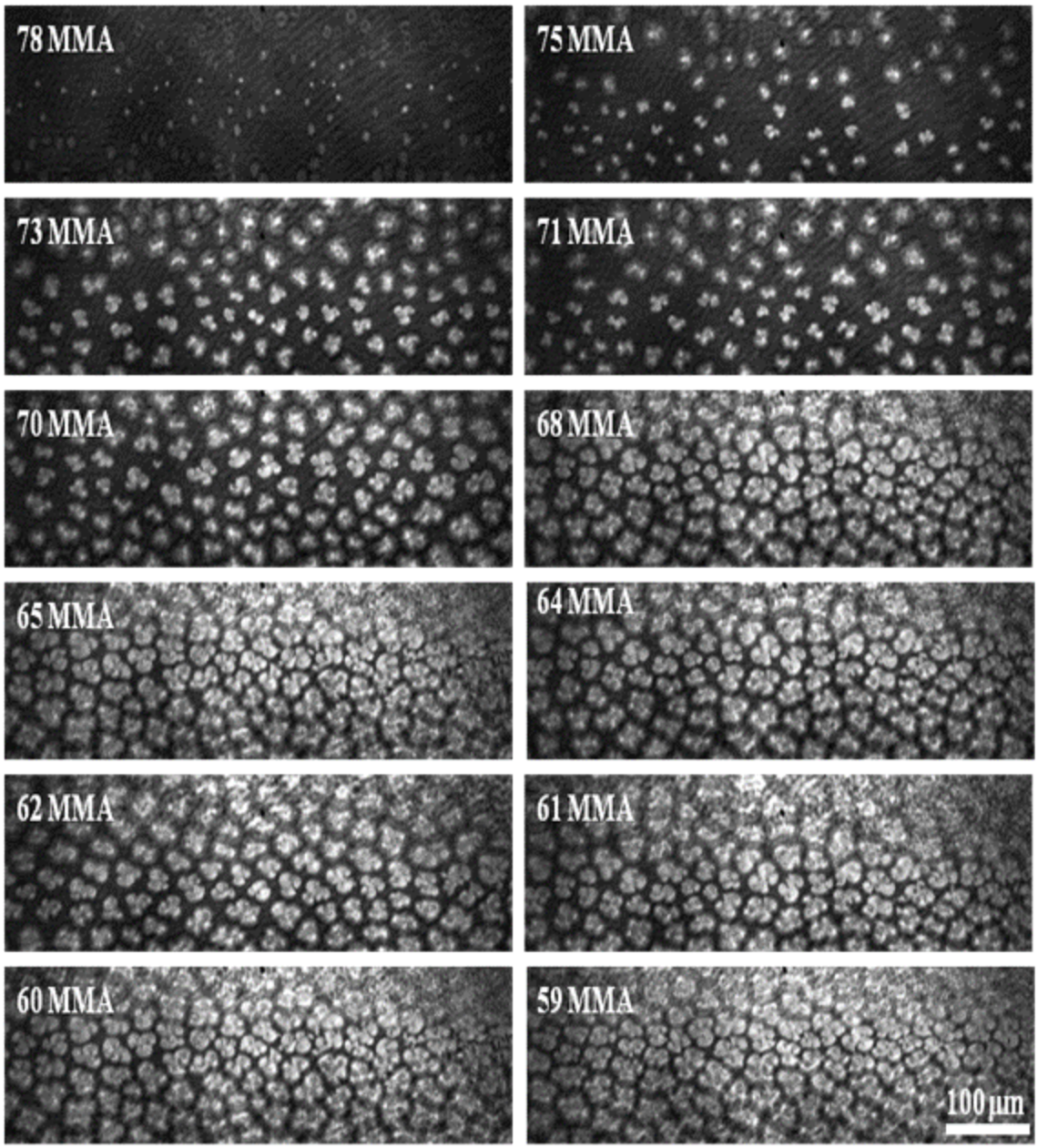

Figure 3.6 BAM images of DPPC domains formation at 23 ^{o}C and for a compression rate of 5.0 Å^{2}/molecule/min.

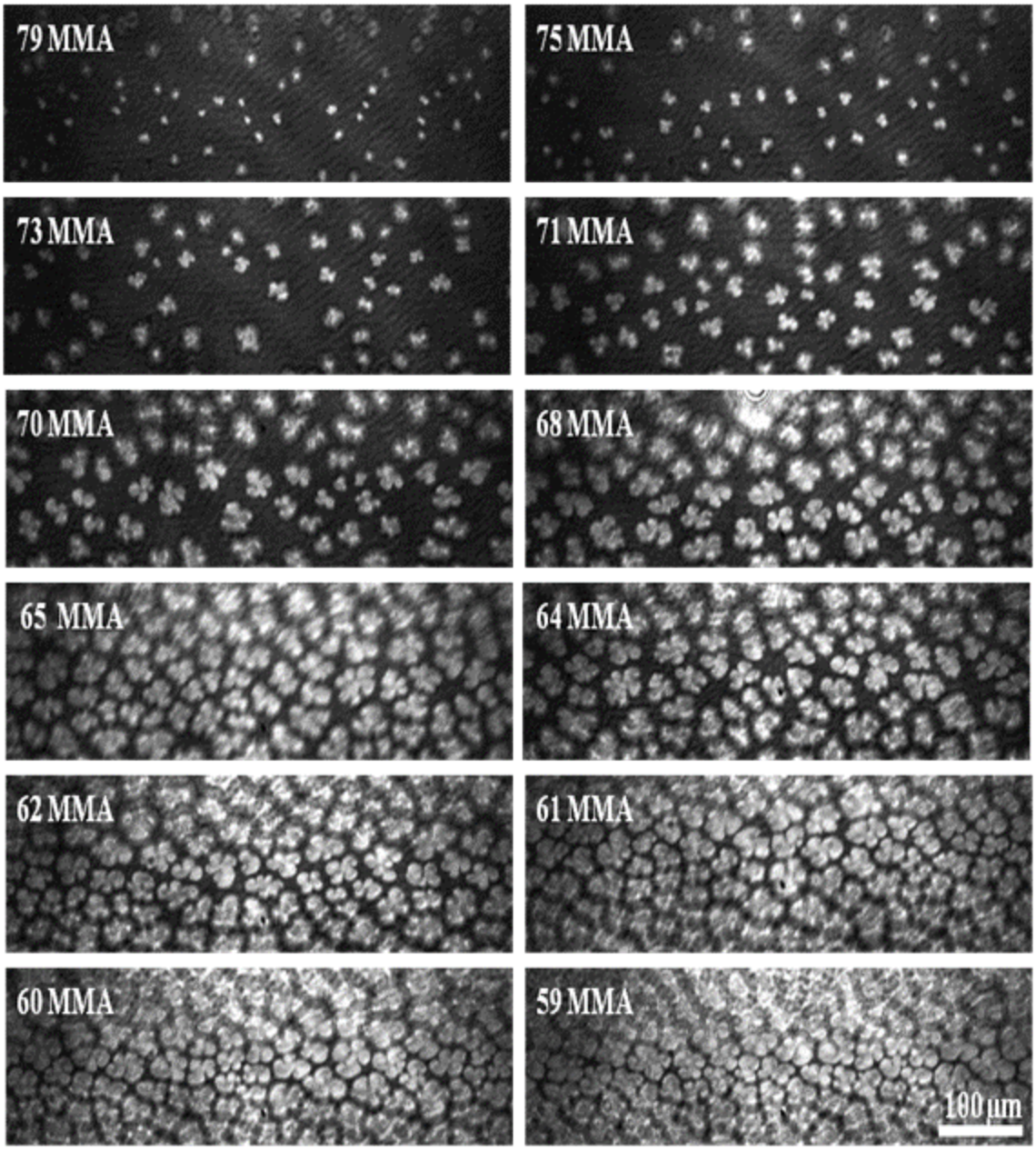

Figure 3.7 BAM images of DPPC domains formation at 23 ^{o}C and for a compression rate of 7.0 Å^{2}/molecule/min.

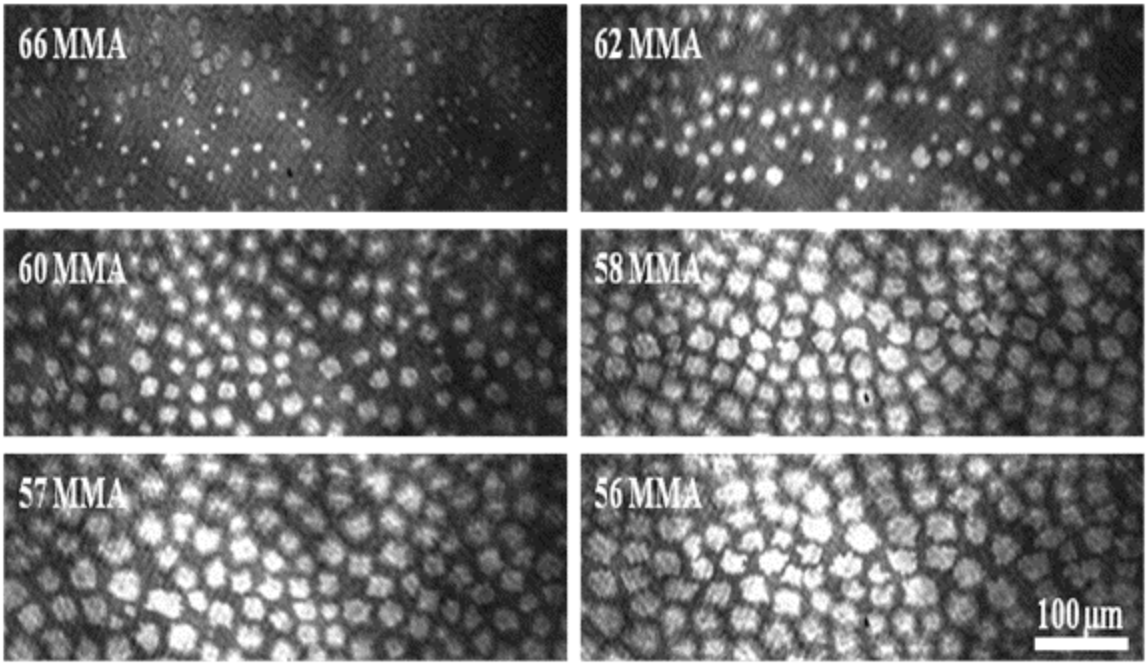

Figure 3.8 BAM images of DPPC domains formation at 32 ^{o}C and for a compression rate of 3.0Å^{2}/molecule/min

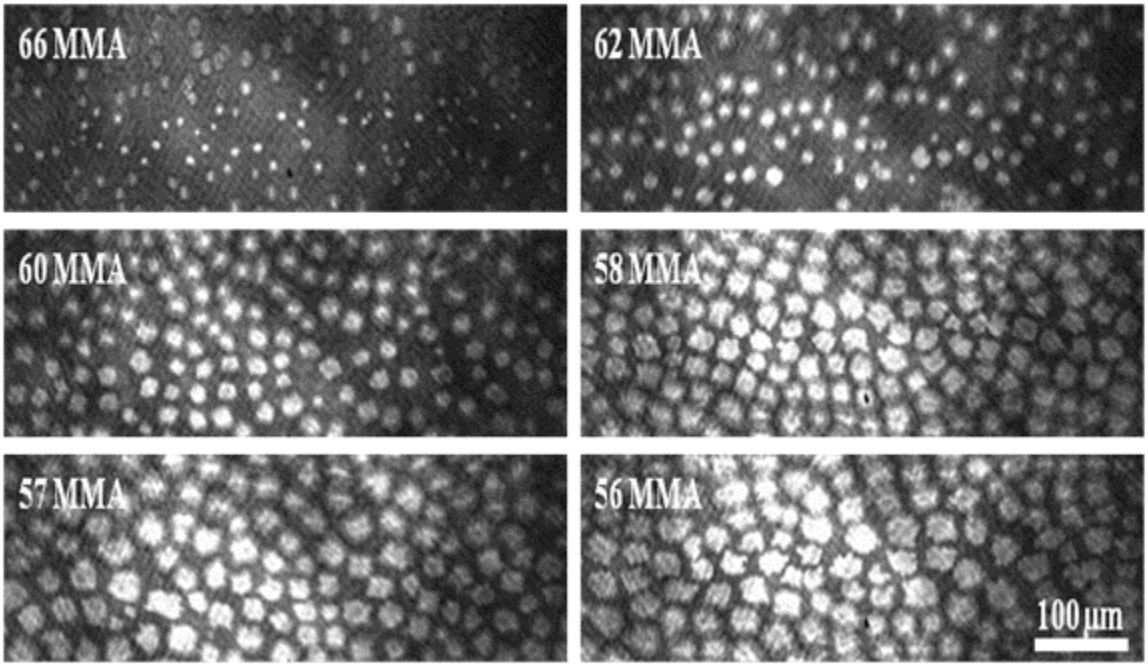

Figure 3.9 BAM images of DPPC domains formation at 32 ^{o}C and for a compression rate of 5.0 Å^{2}/molecule/min.

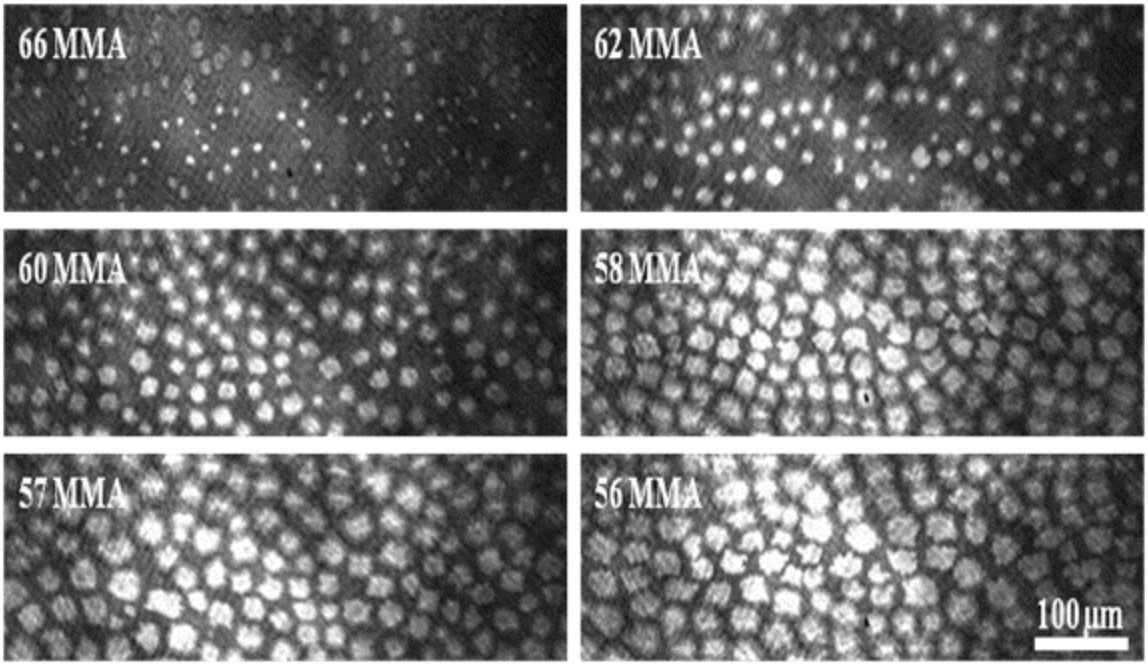

Figure 3.10 BAM images of DPPC domains formation at 32 ^{o}C and for a compression rate of 7.0 Å^{2}/molecule/min.

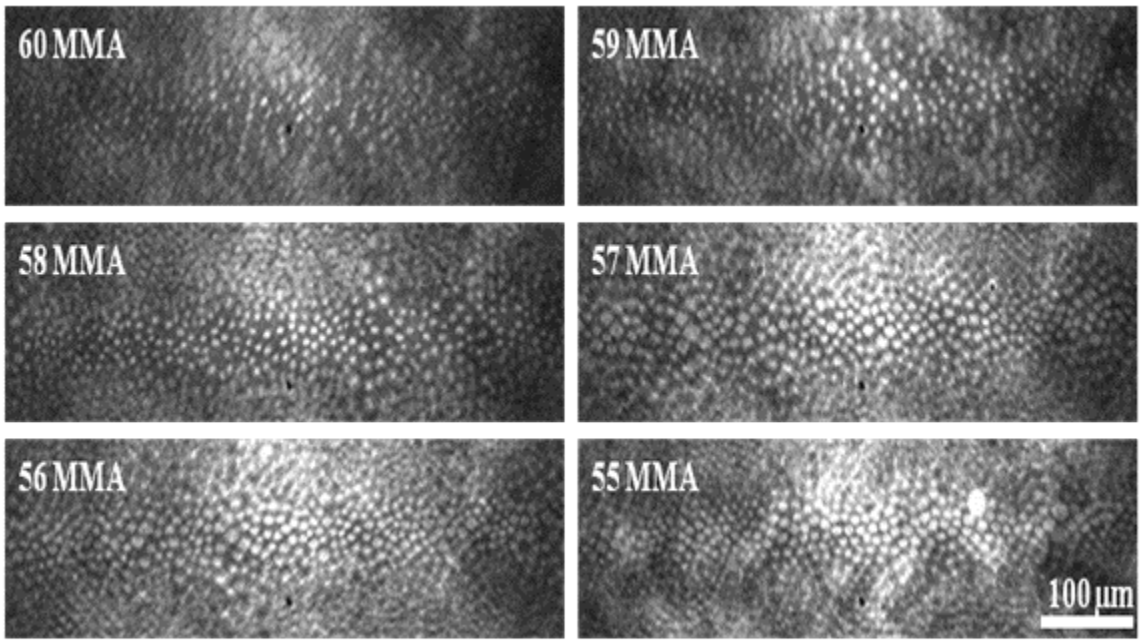

Figure 3.11 BAM images of DPPC domains formation at 37 ^{o}C and for a compression rate of 3.0 Å^{2}/molecule/min.

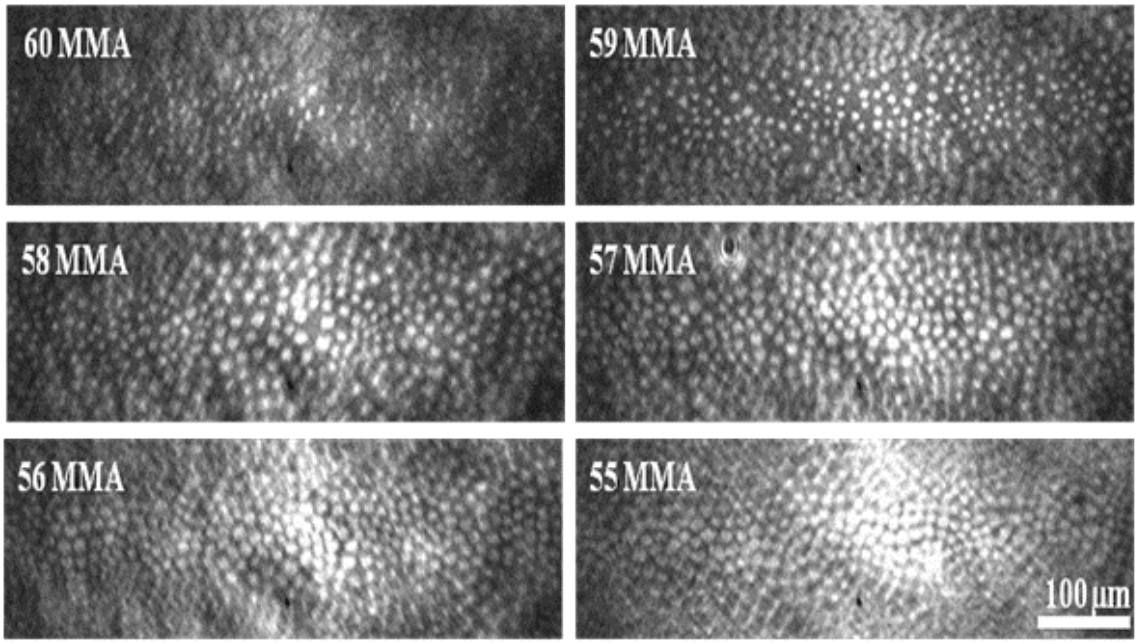

Figure 3.12 BAM images of DPPC domains formation at 37 ^{o}C and for a compression rate of 5.0 Å^{2}/molecule/min.

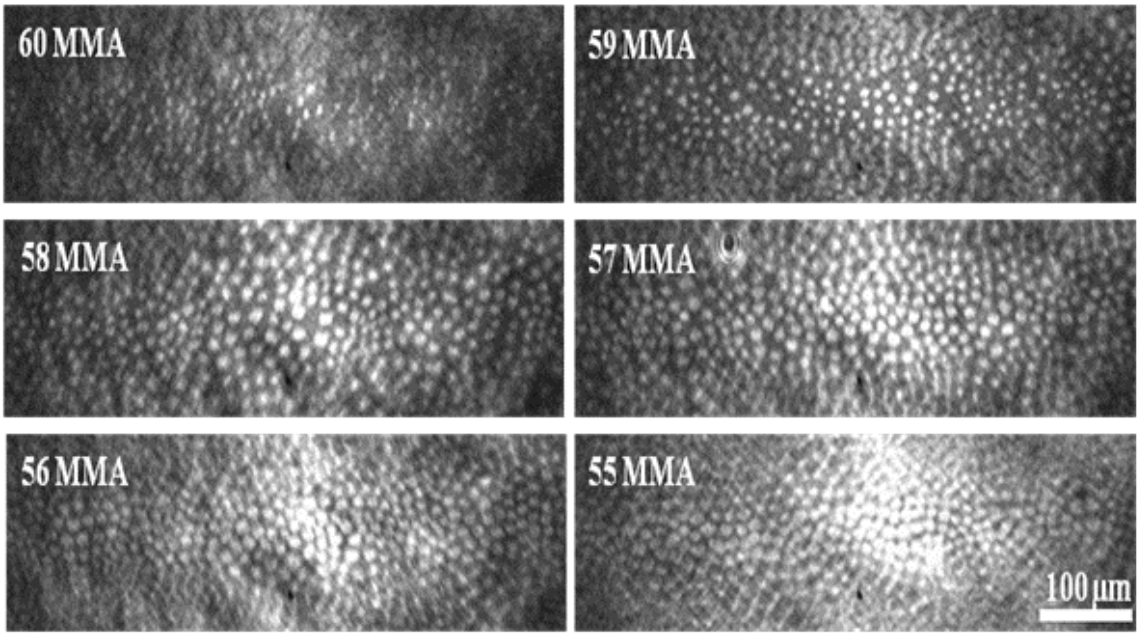

Figure 3.13 BAM images of DPPC domains formation at 37 ^{o}C and for a compression rate of 7.0 Å^{2}/molecule/min.

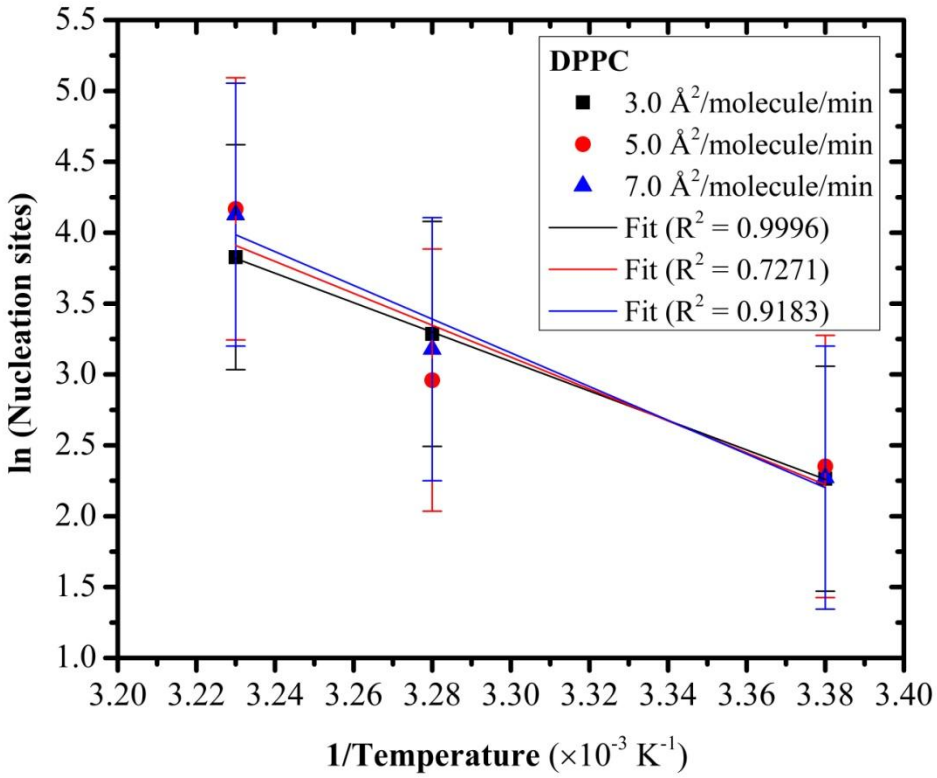

Figure 3.14 Ln Nucleation sites vs 1/Temperature of DPPC on water at compression rates 3.0, 5.0 and 7.0 $Å^2$/molecule/min

3.3.4 DPPE

The phase behavior of DPPE has also been studied extensively.[52, 61, 130] In regards to compression rate studies, Yu *et al.* used a compression rate of 1 $Å^2$/molecule/min and also varied the temperature. Weidemann *et al.* used a compression rate of ~10 $Å^2$/molecule/min but the temperatures used in that study was 44 ^oC. In this section the temperatures used to look at the DPPE domain morphology were 23, 35.5 and 37.5 ^oC.[131]

3.3.5 Surface Pressure-Area Isotherms of DPPE

Surface Pressure-Area Isotherms of DPPE monolayers at 23, 35.5, and 37.5 ^oC

Figure 3.15 shows the isotherms of DPPE monolayers at 23 ^oC for compression rates 3.0, 5.0 and 7.0 $Å^2$/molecule/min. The following distinct phases were identified during monolayer compression: G-LC, (>49 MMA)(idenified by the BAM images), tilted LC (~49-42 MMA), SC (<42 MMA) and a collapse phase at ~40 MMA. The DPPE isotherms are quite different than those of DPPC as there is no plateau region. Another notable difference between both isotherms at 23 ^oC is the fact that at about 38 mN/m DPPE undergoes a phase transition from a tilted condensed phase (LC) to an untilted or (SC).[132]

Figure 3.16 shows the isotherms at 35.5 ^oC with the same compression rates used at 23 ^oC. The following phases were identified during monolayer compression: G-LE-LC (170-60 MMA) (identified by the BAM images), LE-LC (60-45 MMA), SC (<42 MMA)

and a collapse phase at ~40 MMA. The difference in the lift offs between 23 ^{o}C and 35.5 ^{o}C was ~9 MMA. There was also no distinct plateau region.

Figure 3.17 shows the DPPE isotherms at 37.5 ^{o}C with the same compression rates used at 23 and 35.5 ^{o}C. The following phases were identified during monolayer compression: G-LE-LC (~170-75 MMA) identified with the use of the BAM, LE-LC (~75-45 MMA), LC (~45-42),SC (~42-40 MMA) and a collapse phase at ~40 MMA. The change in the lift off from 23 to 37.5 ^{o}C was ~23 MMA. There was also no distinct plateau region observed and the compression rate also had no significant impact on the shape of the isotherms.

3.3.6 BAM Images of DPPE domains

BAM images of DPPE domains at 23 ^{o}C

Figure 3.18 shows the BAM images of DPPE domains for compression rate 7.0 Å^{2}/molecule/min. The solid nature of the domains was not influenced by the compression rate and hence the images in Fig 3.18 represents the images for all three compression rates. At 160 MMA the monolayer is in the G-LC coexistence region. The LC phase is clearly visible as large bright domains with the dark background corresponding to the G phase. At the lift off of the isotherm at 49 MMA, the coexistence region changes into a LC phase as the BAM image is totally bright.

BAM images of DPPE domains at 35.5 ^{o}C

Figures 3.19-3.21 show the BAM images of DPPE domains at the slowest, intermediate, and fastest compression rates respectively. At 150 MMA the images shown for all compression rates revealed that the monolayer was in the G-LE-LC coexistence phase. The BAM images with respect to the G-LE-LC phases particularly at the larger MMA are variable as the observed domain morphology differed each time the experiments was repeated (see Appendix A). According to the nucleation theory (see Section 2.3), it involves the creation of a nucleation site from a homogenous bulk phase. However before the start of compression the LC phase was observed at a zero surface pressure. Any further creation of nucleation sites will therefore be affected by the preexisting LC phase.

The LC phase at 150 MMA has a network-like pattern with pockets of the LE and G phases. As the monolayer is compressed, at the slowest and intermediate compression rates, the network-like pattern increases in width. A few individual domains were also evident at 60 and 54 MMA at the slowest and intermediate compression rates, respectively. Nevertheless the predominant domain morphology at both compression rates was the network-like pattern.

The domain morphology observed at the fastest compression rate was different than those observed at the slowest and intermediate compression rates. At 130 MMA some circular-like domains were apparent as well as the network-like pattern. To explain the simultaneous cohabitation of the two types of domain morphology in terms of electrostatics, the fastest compression rate reduces the molecular orientation of the lipid

dipoles and, in turn, also reduces dipole-dipole repulsion, thus making circular domains possible. In terms of the nucleation theory the fastest compression rate induced more collisions of the DPPE molecules in the monolayer permitting more individual domains to be formed. Circular-like domains were also evident at 120 MMA but by 110 MMA the domains had six branches. At 70 MMA the network-like patterns completely disappeared as only domains with multiple branches were observed. At 59 MMA the number of domains with multiple branches increased and the average diameter of the domains was ~50 μm. However, by 56 MMA the number of domains decreased and the diameter increased to ~200 μm. This increase in the diameter of the domains was the result of the fusion of a few smaller neighboring domains to form larger ones.

Comparing the domain morphology of DPPE at 35.5 ^{o}C and DPPC at 23 ^{o}C (see Figures 3.22 and 3.7, respectively), the DPPE domains are more elongated and highly branched than DPPC. One reason for the difference in the domain morphology between the two lipids is the larger main phase transition temperature of DPPE. The larger transition temperature of DPPE means that the DPPE molecules in the monolayer are more aligned than DPPC. The highly aligned DPPE lipid molecules, in an attempt to reduce the repulsive interactions between each other, elongate the domain hence resulting in branching. Monte Carlo simulations studies to determine the shape of phospholipids domains also indicate that lobed domains are only possible at low temperatures.[133]

BAM images of DPPE domains at 37.5 ^{o}C

Figures 3.22-3.24 show the formation of DPPE domains at the slowest, intermediate, and fastest compression rates, respectively. At 150 MMA for all compression rates, the monolayer is in the G-LE-LC coexistence region. Upon further compression at 120 MMA different domain morphologies were observed as the compression rate was varied. At the slowest compression rate, network-like patterns were observed, while at the intermediate and fastest compression rates the domains had multiple branches. At 90 MMA with the slowest compression rate, individual domains were observed but with continued compression elongated domains were more evident. The elongated domains increased in width until they fused into the LC phase. The domain morphology was quite similar to the data reported at 35.5 ^{o}C with the two slower compression rates. Even at 37.5 ^{o}C the monolayer is still very solid-like hence the slowest compression rate does not perturb the DPPE molecules in the monolayer enough to have an increased number of domains.

The domain morphology at the intermediate and fastest compression rates is quite similar. At 65 MMA for both the intermediate and fastest compression rates, the domains have multiple branches. However the tips of the domains were slightly different for both compression rates. At the intermediate compression rate the domain tips are more elongated than the tips at the fastest compression rate which are more rounded. This rounding of the domains at the fastest compression rate suggests a slight reduction in electrostatic repulsion. At 66 and 62 MMA at the fastest and intermediate compression rate, respectively, the domain tips made contact with each other while still preserving

their individual shape. This phenomenon is known as the 'bridging' effect and is known to occur in lipid monolayers containing fewer methyl groups in the headgroup.[61] One possible reason for this effect is the very small line tension at the boundary of the domain resulting in the weakening at the domain boundary.

To determine the impact of the compression rate on the observed number of domains, BAM images of the domain formation at 37.5 ^{o}C for the intermediate and fastest compression rates were analyzed (see Figures 3.23 and 3.24). At 90 MMA and the fastest compression rate the average diameter of the domains observed was ~50 μm, while at the intermediate compression rate the average diameter was ~80 μm. The observed number of domains was also greater at the fastest compression rate, which is in agreement with the nucleation theory. However at 66 MMA the number of domains was greater at the intermediate compression rate ; the average diameters of the domains at the intermediate and fastest compression rate were 60 and 70 μm, respectively. These results indicate that as the compression rate increased the number of domains also increased at the start of domain formation, however with continued compression neighboring domains fuse to form larger ones. As the compression rate increases fluctuations in the monolayer should also increase. The presence of these fluctuations in the monolayer should also increase the probability of domain interactions hence the observed domain fusion.

Similarly, to determine the impact of temperature on the domain morphology and the sizes of the domains, BAM images at 35.5 and 37.5 ^{o}C were analyzed (see Figures 3.19-3.24). It was clearly evident that the area of the network-like domains observed at 35.5 ^{o}C was reduced at 37.5 ^{o}C. At 35.5^{o}C and the fastest compression rate from 59 to 57

MMA, the average diameter of the domains was ~50 μm, however by 56 MMA domain structures of diameters ranging from ~100 to 200 μm with a decrease in the number of domains. At 37.5 ^{o}C and the intermediate compression rate at 66 and 60 MMA the average diameter of the domains were ~60 μm, while at the fastest compression rate, the average diameter of the domains at 66 and 60 MMA was ~80 μm.

The DPPE data presented here relating the compression rate, the temperature and the number of observed nucleation sites are contradictory to the nucleation theory, as should be expected.

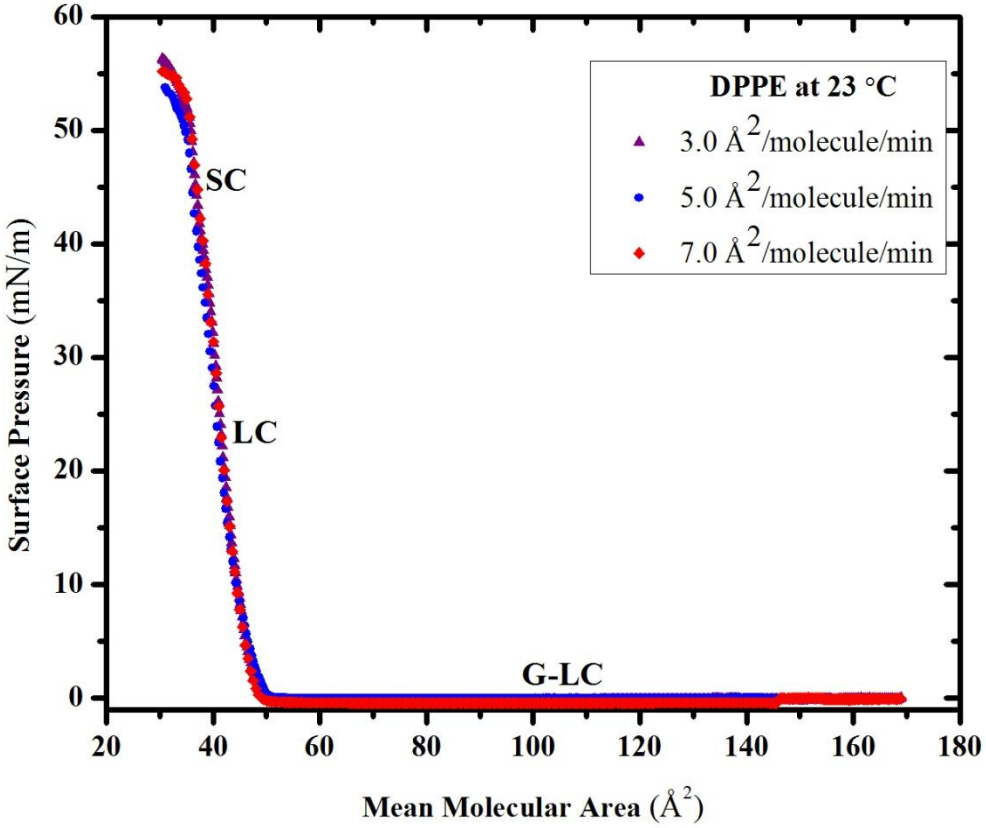

Figure 3.15 Surface pressure-area isotherm of DPPE monolayers spread on water at 23 ^{o}C and for three compression rates.

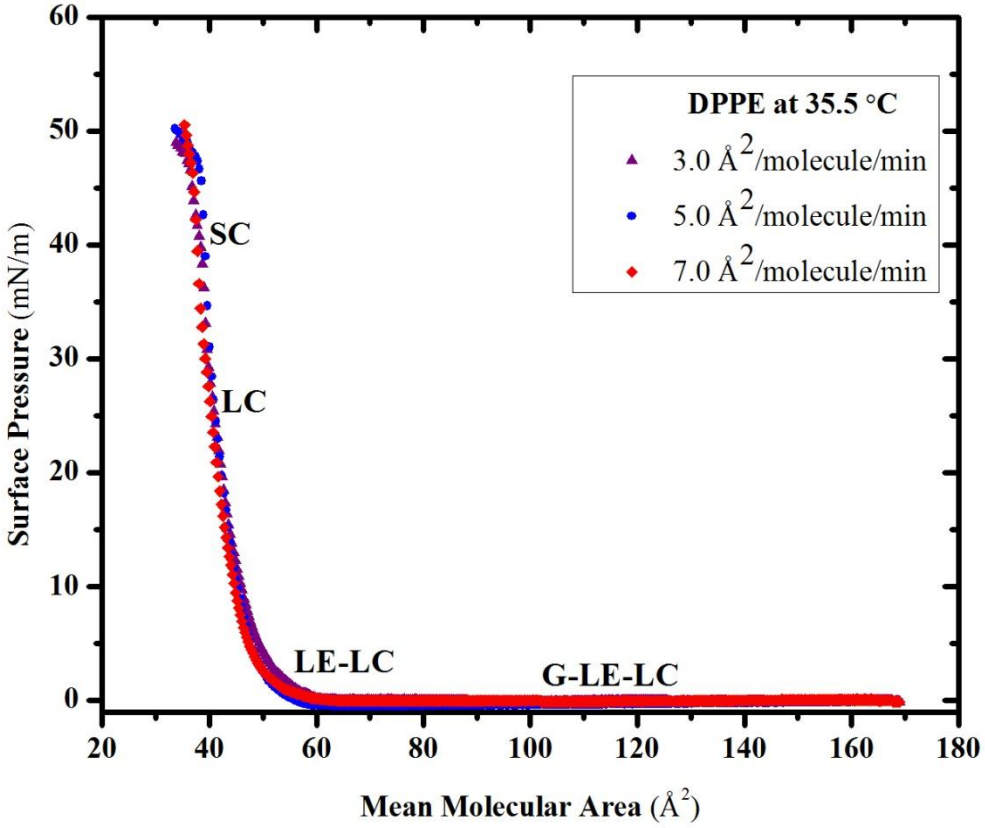

Figure 3.16 Surface pressure-area isotherms of DPPE monolayers spread on water at 35.5 ^{o}C and for three compression rates.

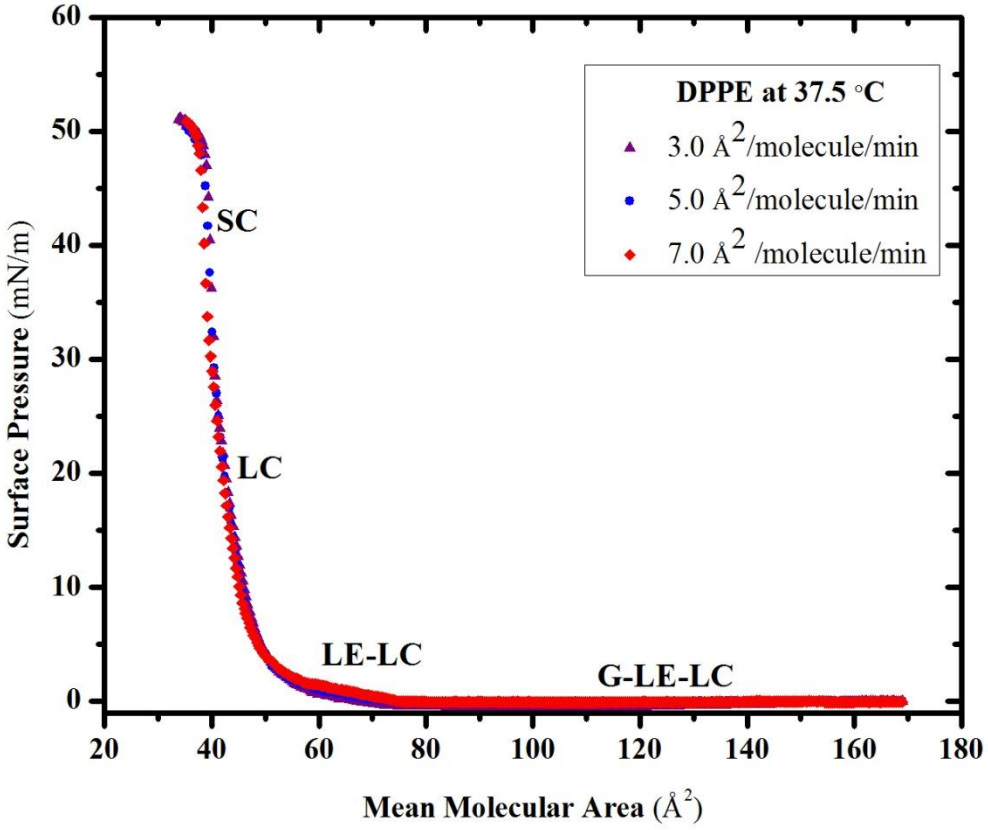

Figure 3.17 Surface pressure-area isotherms of DPPE monolayers spread on water at 35.5 ^{o}C and for three compression rates.

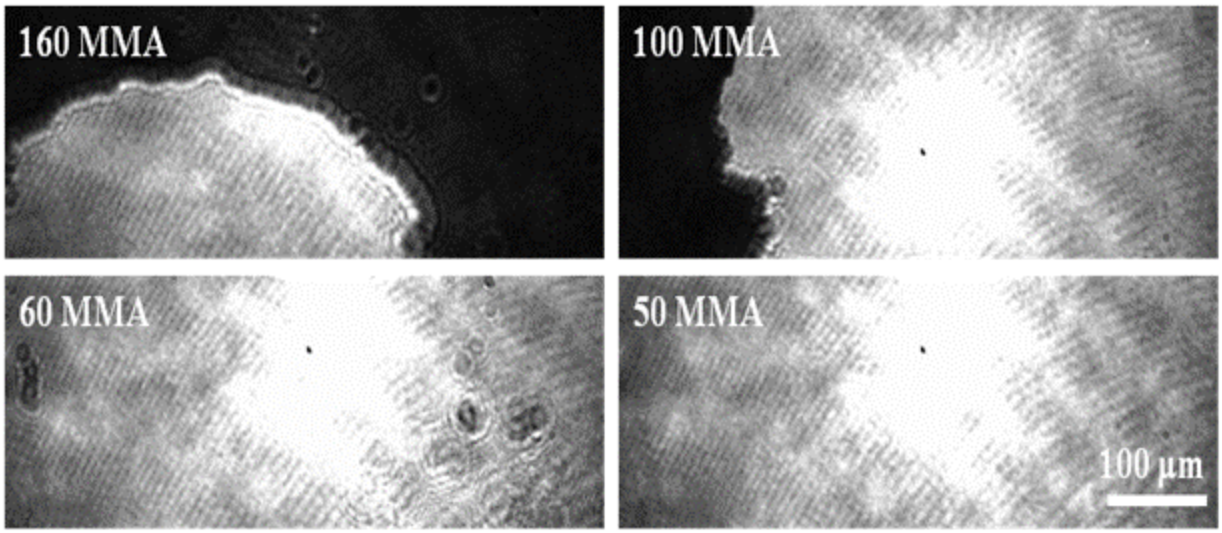

Figure 3.18 BAM images of DPPE domains at 23 ^{o}C for a compression rate of 7.0 Å^{2}/molecule/min. These images can be applied for all compression rates as the domain morphology was not affected.

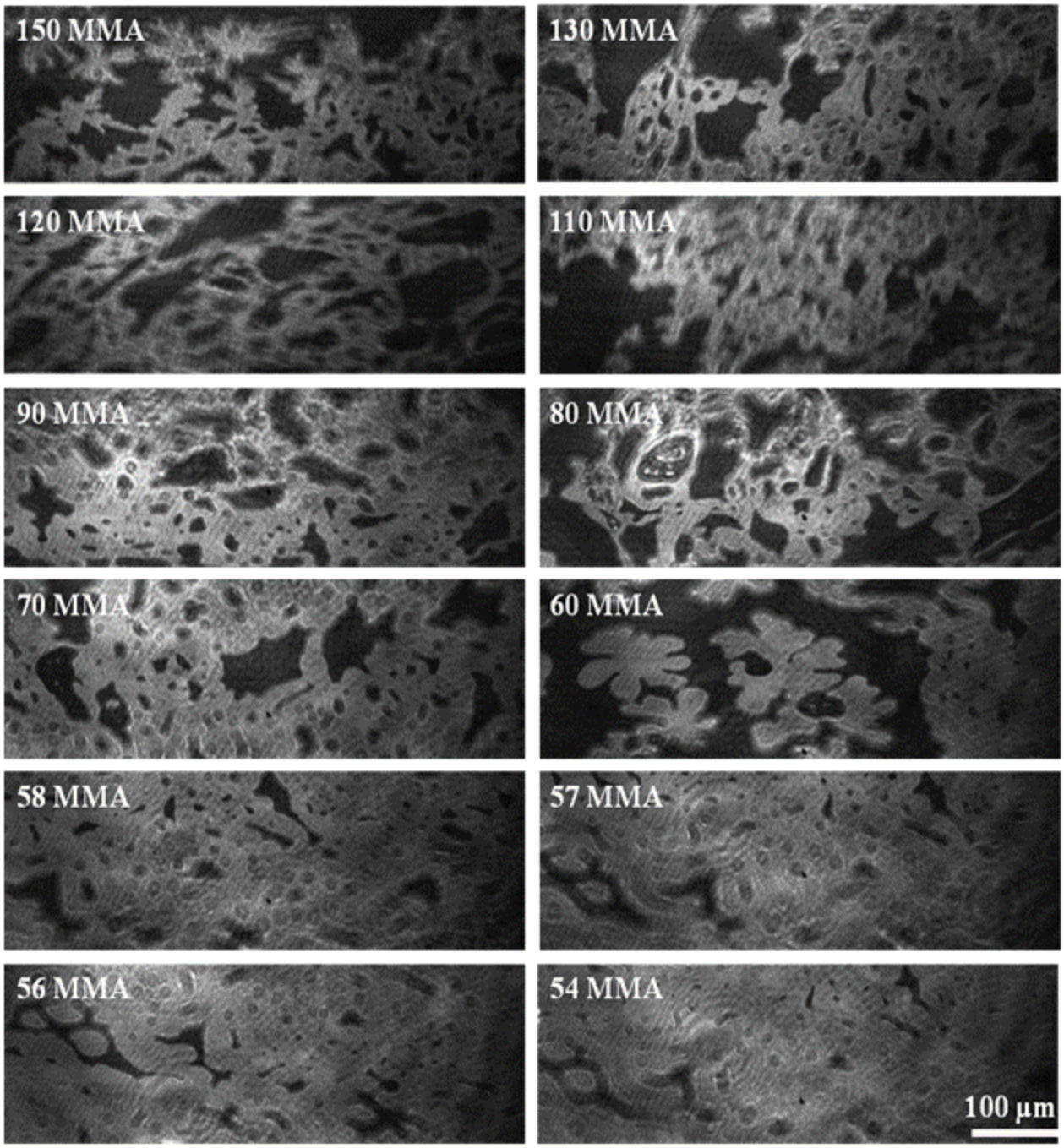

Figure 3.19 BAM images of DPPE domains at 35.5 ^{o}C and for a compression rate of 3.0 Å^{2}/molecule/min.

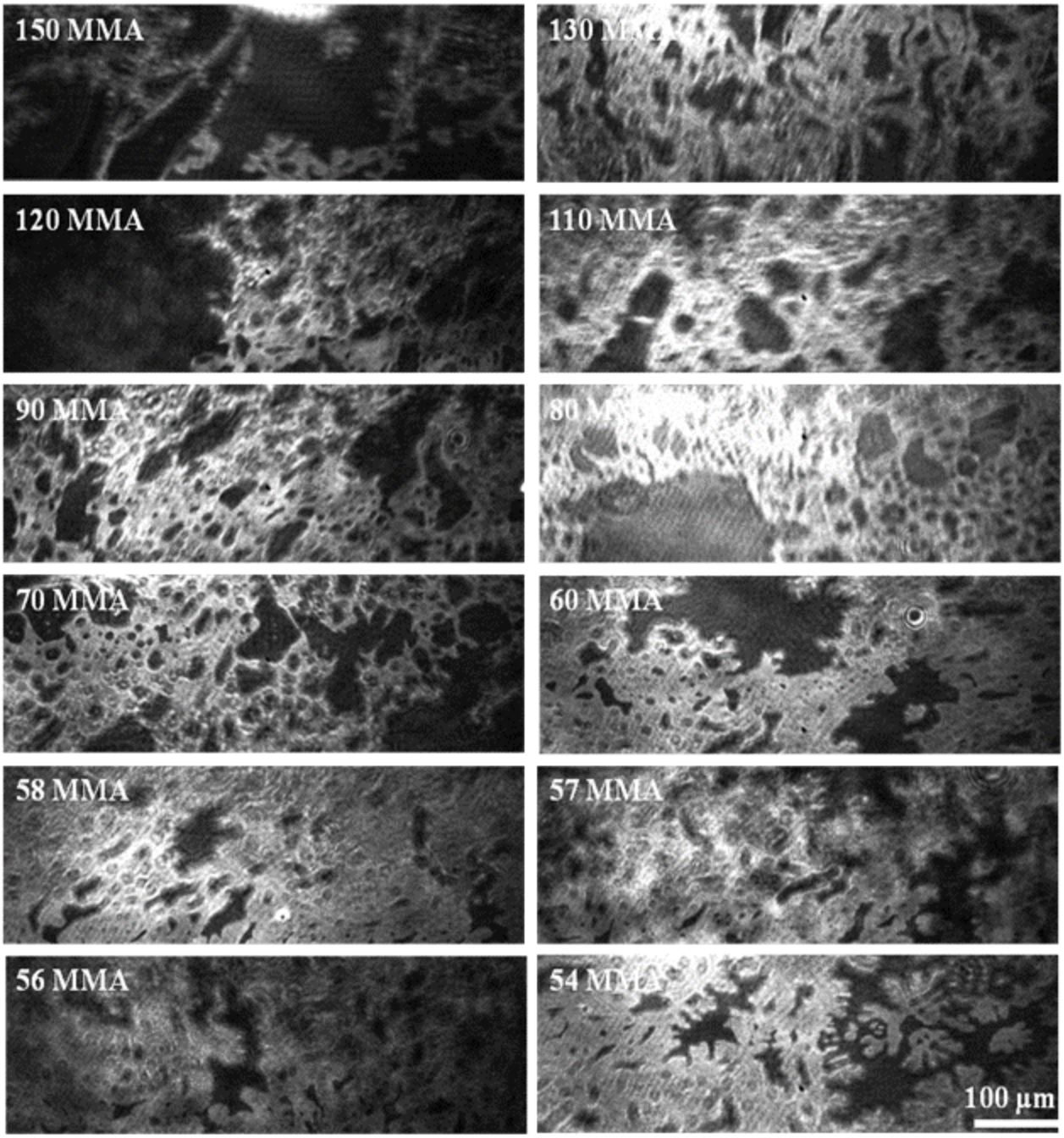

Figure 3.20 BAM images of DPPE domains at 35.5 ^{o}C and for a compression rate of 5.0 Å^{2}/molecule/min.

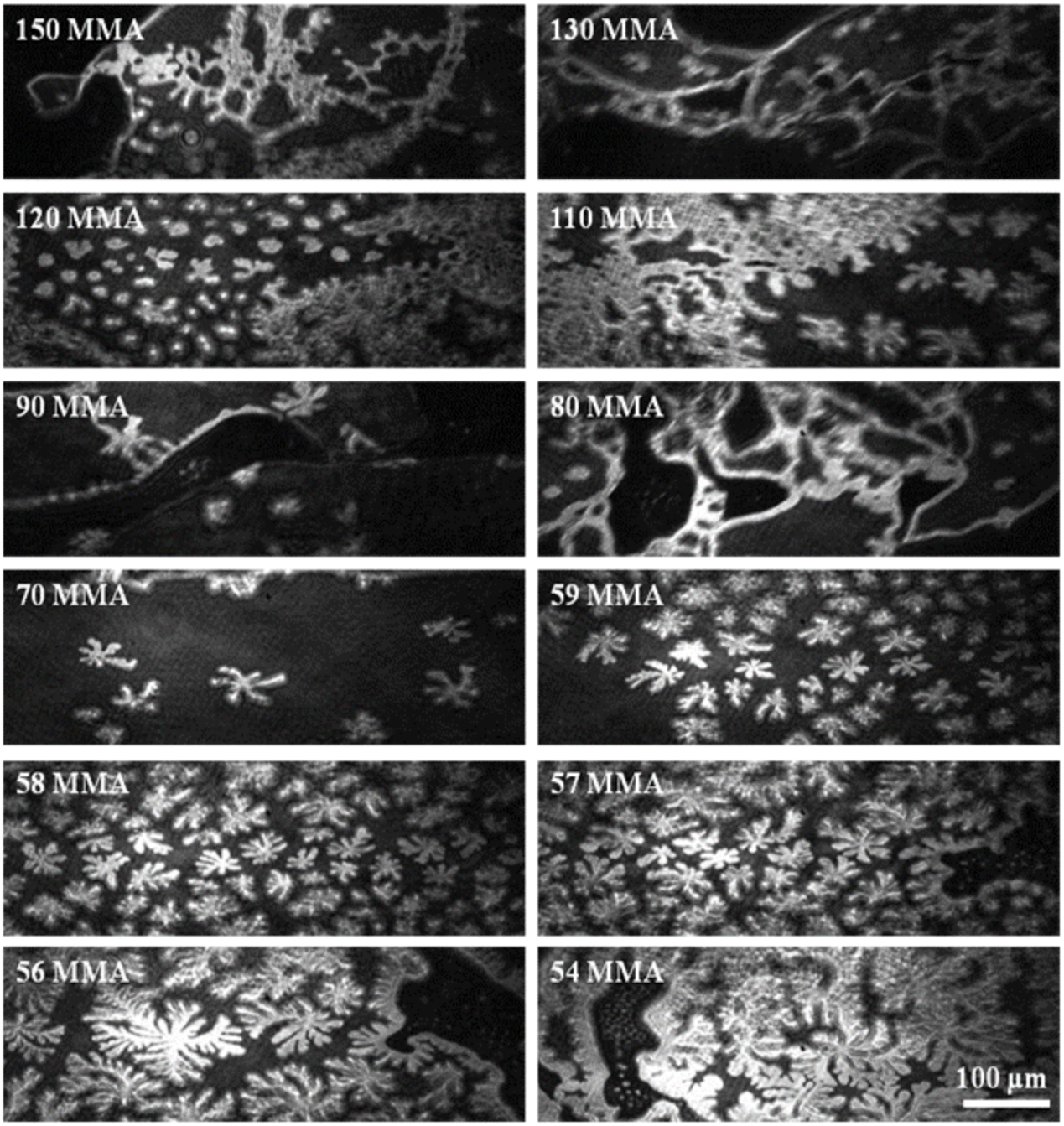

Figure 3.21 BAM images of DPPE domains at 35.5 ^{o}C and for a compression rate of 7.0 Å^{2}/molecule/min.

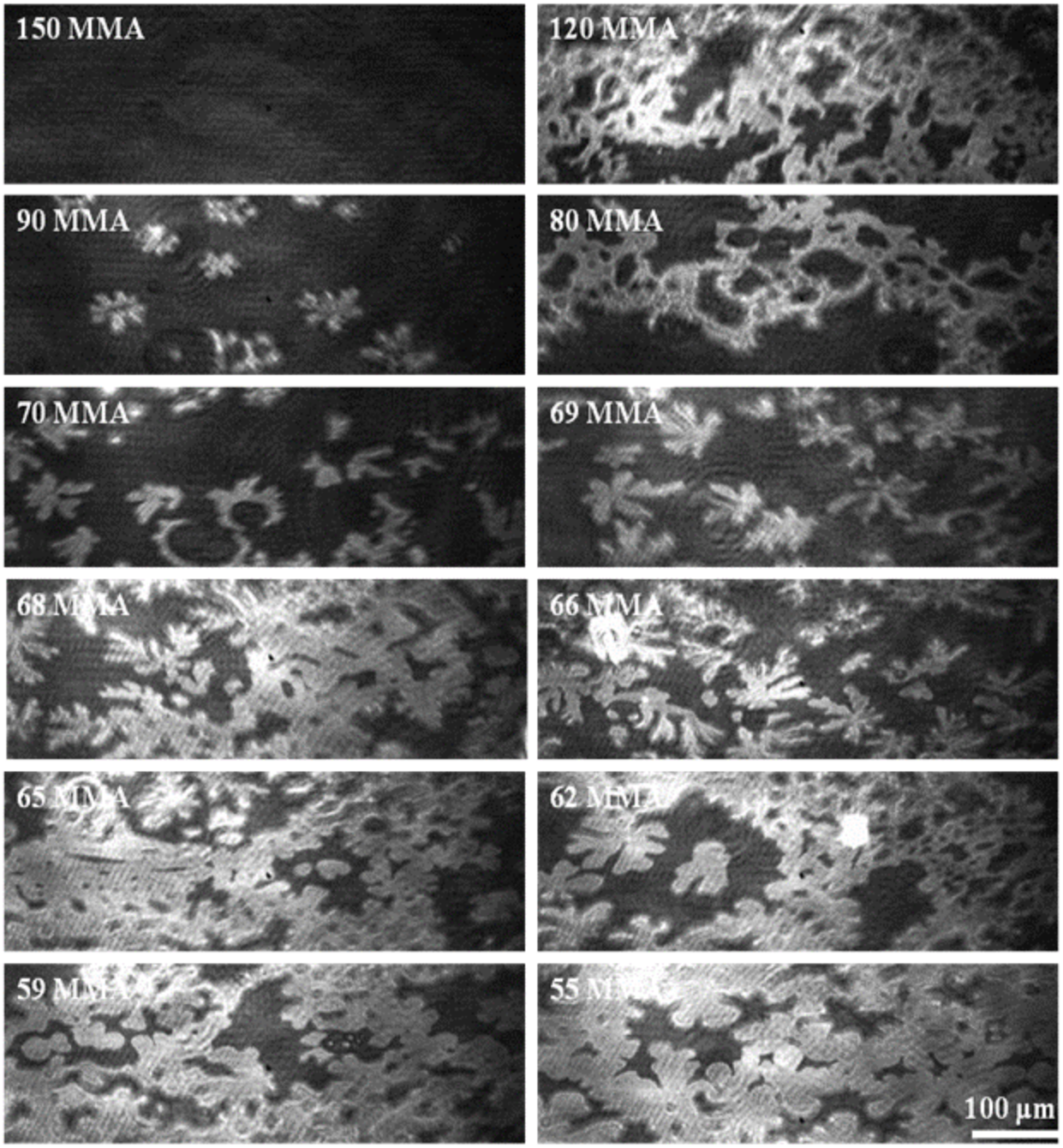

Figure 3.22 BAM images of DPPE domains at 37.5 ^{o}C and for a compression rate of 3.0 Å^{2}/molecule/min.

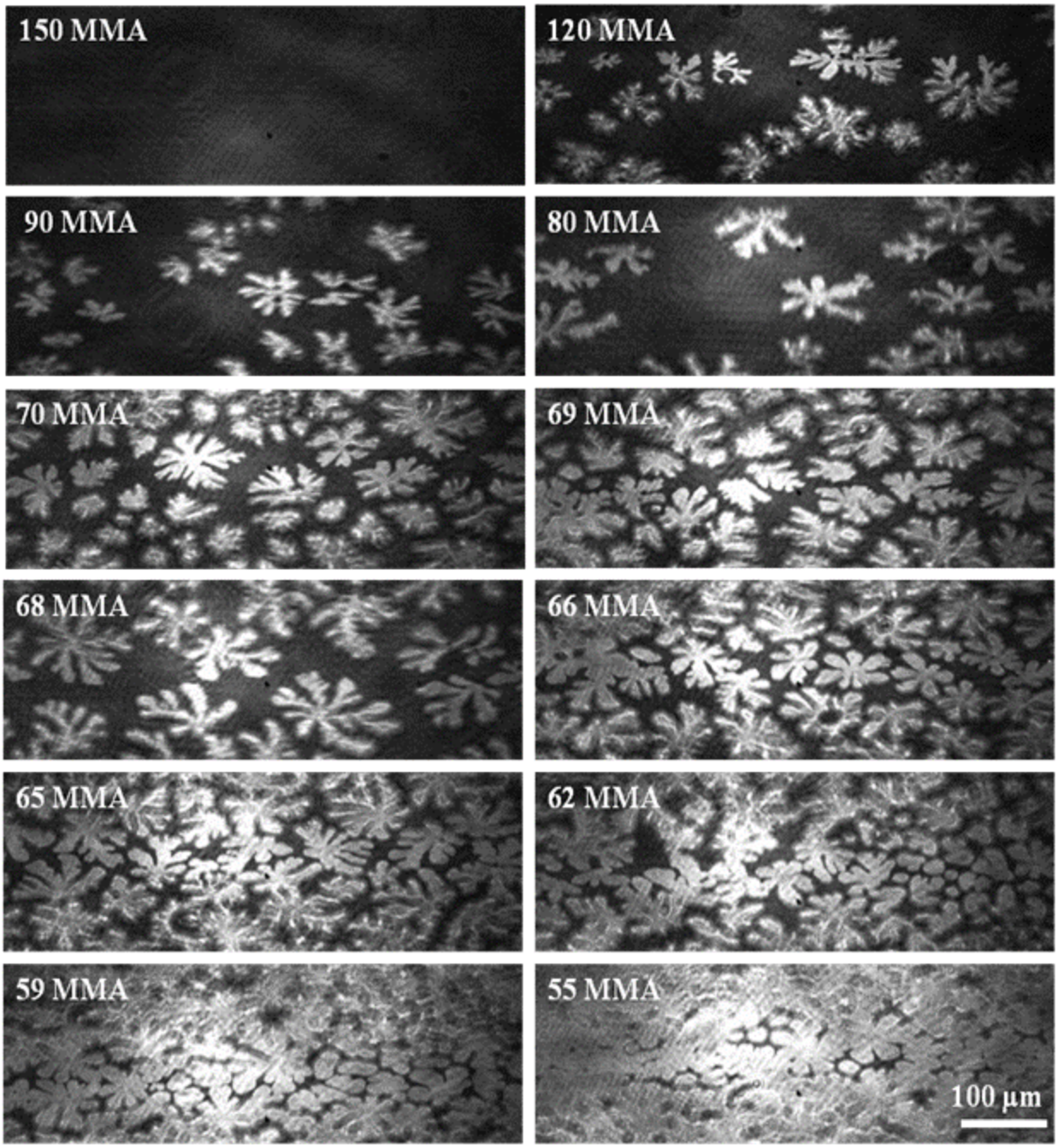

Figure 3.23 BAM images of DPPE domains at 37.5 ^{o}C and for a compression rate of 5.0 Å^{2}/molecule/min.

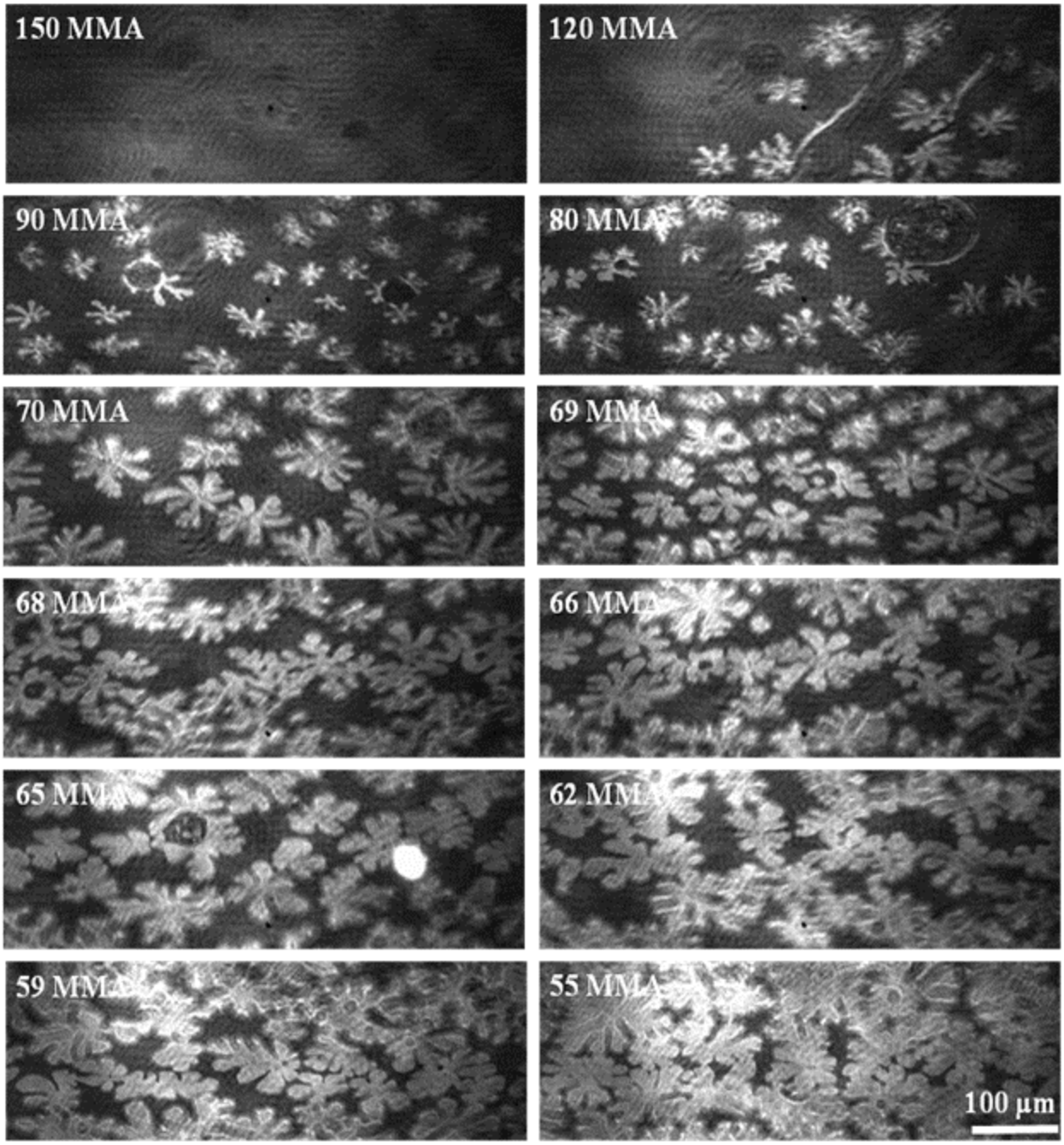

Figure 3.24 BAM images of DPPE domains at 37.5 ^{o}C and for a compression rate of 7.0 Å^{2}/molecule/min.

4. ANIONIC MONOLAYERS AT THE AIR/WATER INTERFACE WITH VARIED TEMPERATURES AND COMPRESSION RATES

DPPG is the most prevalent anionic phospholipid found in lung surfactant of most mammals (Figure 4.1).[134] It also has two saturated 16 carbon alkyl tails like DPPC and DPPE but with a glycerol headgroup. The main phase transition temperature of DPPG bilayers is about 40 ^{o}C which is similar to DPPC.[135] The net negative charge of DPPG indicates that the electrostatic interactions between the lipid molecules within a monolayer are very important. DPPG is typically sold in the form of a sodium (Na) salt and therefore the Na^{+} counterion must be taken into consideration. Simulation studies with PG and the Na^{+} counterion demonstrated that there is indeed strong attractive interactions between PG headgroups. [136-137] The mechanism proposed for this interaction involved an interlipid counterion bridge with the Na^{+} and the strong attractive intra- and intermolecular hydrogen bonding between the headgroups.[136] Pascher *et al*. showed that the cross-sectional area of DPPG is 44 $Å^2$ per molecule which is larger than DPPE but smaller than DPPC.[138] DPPG can exist in an untilted conformation when highly compressed, however DPPC as previously mentioned cannot exist in an untilted configuration even though the two headgroups differ in size by ~2.5 $Å^2$. One reason given for the untilted conformation of DPPG is the attractive hydrogen bonding

interactions between the headgroups of DPPG that can overcome the negative charge of the headgroup.[54]

The experiments presented in Chapter 4 used a Langmuir trough coupled with a BAM to obtain isotherms and images from a pure insoluble monolayer of DPPG compressed isothermally on a pure water at pH 5.5. To understand the domain morphology of DPPG monolayers, three different temperatures and compression rates were used. The temperatures used were 23, 32 and 37 ^{o}C and the compression rates used were 3.0, 5.0, and 7.0 Å^{2}/molecule/min.

4.1 Materials

1,2-dipalmitoyl-*sn*-glycero-3-phospho-(1'-*rac*-glycerol) (DPPG), (> 99% purity; Avanti Polar Lipids, Alabaster, AL) was used without further purification. Methanol and chloroform (spectrophotometric grades) were purchased from Fisher Scientific. Nanopure water was obtained from a Barnstead Nanopure filtration system and had a resistivity of 18.3 MΩ cm.

4.2 Sample Preparation

Stock solution of 1mM DPPG was made using chloroform/methanol mixture with a 3:1 (v/v) ratio.

4.3 Results and Discussion

4.3.1 DPPG

The phase behavior of DPPG monolayers spread on a water subphase has also been studied over the years.[139-141] Some compression rate studies have also been done; for instance, Vollhardt *et al.* used three compression rates 7.5, 13.2, and 22.2 $Å^2$/molecule/min with varying temperatures.[140] The compression rates used in that study showed a change in the domain morphology as the compression rate increased. The compression rates used here however are slower than those done by Vollhardt *et al.*.[140]

4.3.2 Surface Pressure-Area Isotherms of DPPG

Surface Pressure-Area Isotherms of DPPG at 23, 32 and 37 ^oC

The observed phase transitions of DPPG monolayers at 23 ^oC are shown in Figure 4.2. The isotherms are very different than those of DPPC at 23 ^oC (see Figure 3.1) as there is no LE-LC phase. The differences in the shape of the isotherms between both lipids are definitely an indication that the different headgroups allow for different packing of the molecules. The isotherms at 23 ^oC exhibited the following phases : G-LC (>60 MMA), LC (~60-48 MMA), SC (~48-46 MMA) and a collapse phase (<46 MMA).

Figure 4.3 shows the isotherms at 32 ^oC with the following phases: G-LE (>112 MMA), LE (~93-112 MMA), LE-LC, (~93-55 MMA), LC (~55-48 MMA), SC (~48-46) and a collapse phase (<46 MMA). The shape of the isotherms at this temperature is different than the one at 23 ^oC as there is a distinct plateau region in the surface pressure

range of 3-5 mN/m. The lift offs of the isotherms at 32 ^{o}C changed by ~56 MMA when compared to those at 23 ^{o}C.

Figure 4.4 shows the isotherms of DPPG monolayers at 37 ^{o}C with the following phases: G-LE (>116 MMA), LE (~90-116 MMA), LE-LC, (~90-55 MMA), LC (~55-46 MMA) and a collapse phase at <46 MMA. The lift offs of the isotherms at 37 ^{o}C changed by ~62 MMA when compared to the isotherms at 23 ^{o}C and ~4 MMA when compared to 32 ^{o}C. Again, a plateau region was observed but in the surface pressure range of 7-9 mN/m. The compression rate did not affect the shape of the isotherms at any temperature.

4.3.3 BAM Images of DPPG domains

BAM images of DPPG domains at 23 ^{o}C

Figure 4.5 shows the DPPG domains observed at compression rate 7.0 Å^{2}/molecule/min. As was observed with DPPE, the LC phase was also observed at the start of compression and therefore the images in Fig. 4.5 represents the domain morphology for all compression rates. At 170 MMA the domains appeared as very small circles with a diameter of ~5 μm. However at 100 MMA the domain morphology began to change into a network-like pattern. This network-like pattern increased in width with continued compression until it fused into the LC phase.

BAM images of DPPG domains at 32 ^{o}C

Figures 4.6-4.8 illustrate DPPG monolayers at the slowest, intermediate, and fastest compression rates, respectively. At 90 MMA for all compression rates, the

monolayer was in the LE-LC phase. The domains at the slowest compression rate had multiple branches while at the intermediate and fastest compression rates the domains were more circular. At the slowest compression rate the average domain diameter was ~50 μm, while at the intermediate and fastest compression rates the averages were ~30 μm at both compression rates. At 80 MMA and the slowest compression rate, the domains maintained their morphology only increasing to a diameter of ~80 μm, while at the intermediate compression rate the average diameter was ~60 μm. At the fastest compression rate, there was a bimodal distribution in regards to the domain morphology and diameter as circular and multiply-branched domains were observed with average diameters of ~60 and 30 μm, respectively. The domain shape at the slowest compression was maintained until fusion into the LC phase with an average diameter of ~90 μm. At the intermediate compression rate the domain morphology was also maintained, however the average size of the domains were ~70 μm. At the fastest compression rate at 70 MMA the domains were no longer bimodal in regards to both the shape and diameter as only domains with multiple branches were observed with a diameter of ~90 μm.

BAM images of DPPG at 37 ^{o}C

Figures 4.8-4.10 show DPPG monolayers at the slowest, intermediate, and fastest compression rates, respectively. At the slowest, intermediate and fastest compression rate, domains were observed at ~80, 78 and 75 MMA, respectively. At 75 MMA and the slowest compression rate, the average domain diameter was ~70 μm. At 73 MMA for both the intermediate and fastest compression rates, the average domain diameters were

~70 and 50 μm, respectively. With continued compression the domains at the slowest compression rate increased to a diameter of ~90μm while at the intermediate and fastest compression rates domains of ~100 μm or larger were observed indicating again fusion of the domains.

As the compression rate at both 32 and 37 ^{o}C increased, the number of domains also increased at the start of domain formation. However at the intermediate and fastest compression rates at both temperatures the domains fused with continued compression. This phenomenon was also observed with DPPC at 23 ^{o}C and DPPE at 37.5 ^{o}C The strong interactions between the lipid molecules as in DPPE made it difficult to obtain reliable statistical data on the impact on the compression rate on the number of domains.

To understand the impact of temperature on the number and size of observed domains, BAM images at 35 and 37 ^{o}C at the different compression rates were analyzed. For the slowest compression rate (see Figures 4.6 and 4.9), at 70 MMA, the number of domains observed at 32 ^{o}C was less than at 37 ^{o}C. The average diameter of the domains at 32 ^{o}C is ~85 μm, while at 37 ^{o}C the average diameter is ~60 μm. However, at the intermediate compression rate at 32 and 37 ^{o}C, respectively (see Figures 4.6 and 4.10), the number of domains at 70 MMA was greater at 32 ^{o}C. The average domain diameter at 32 and 37 ^{o}C was ~90 and 50 μm, respectively. A similar observation could be made at the fastest compression rate and 32 and 37 ^{o}C (see Figures 4.8 and 4.11).

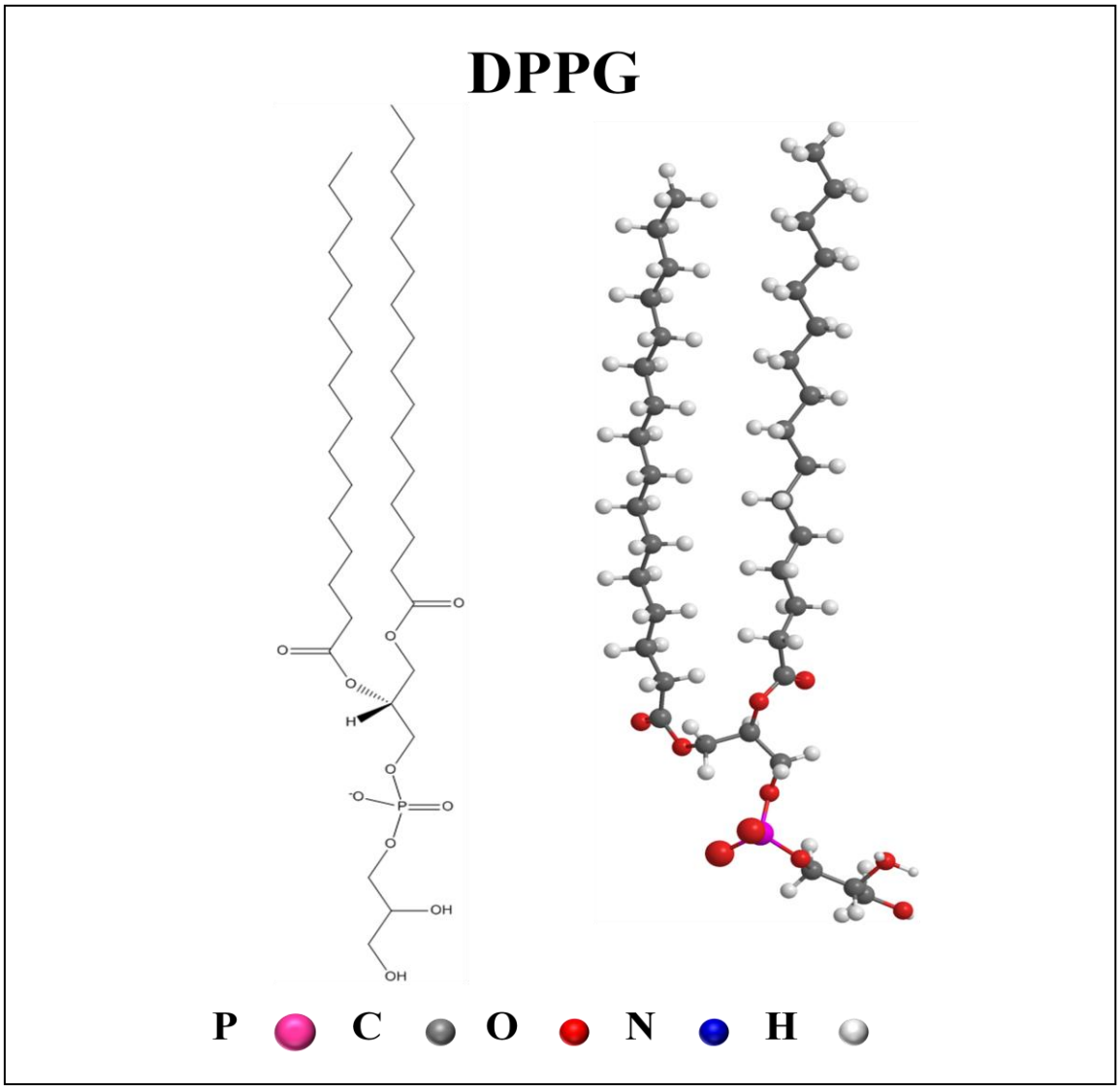

Figure 4.1 The molecular structure of DPPG.

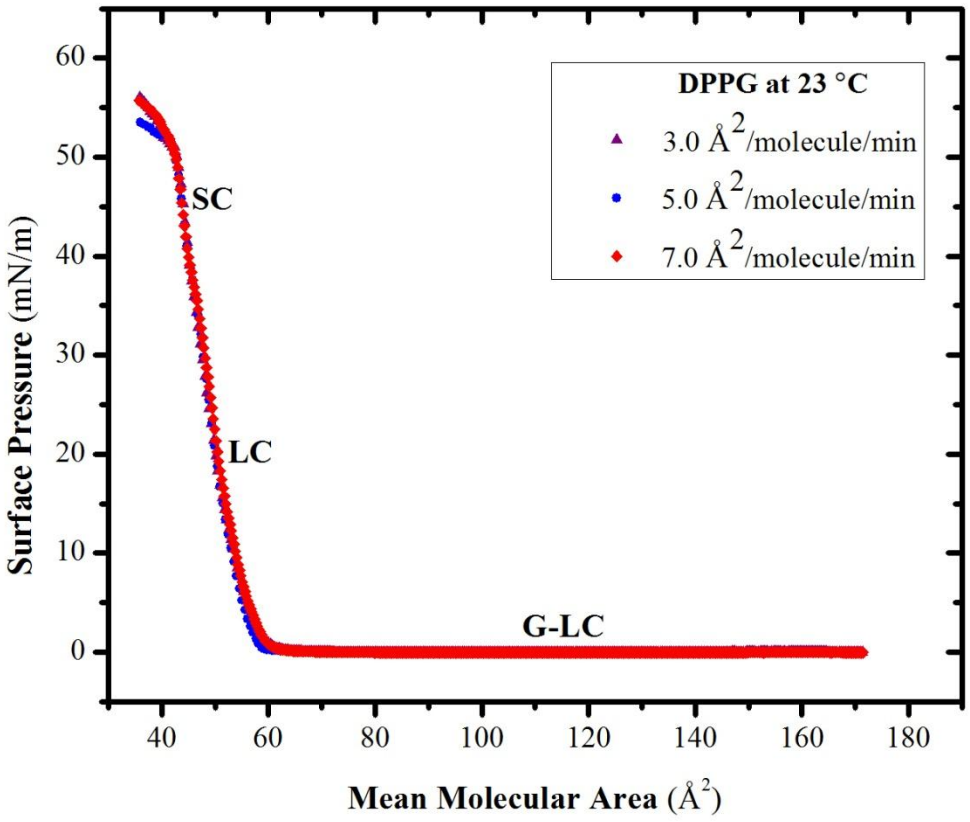

Figure 4.2 Surface pressure-area isotherm of DPPG monolayers spread on water at 23 ^{o}C and for three compression rates.

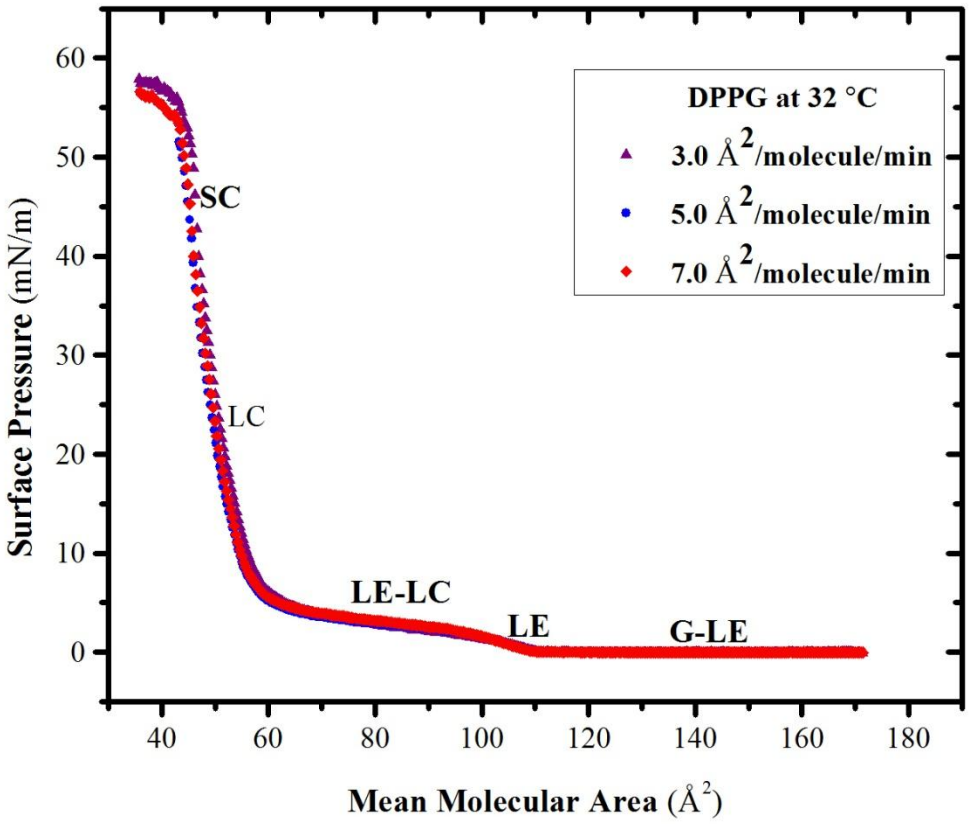

Figure 4.3 Surface pressure-area isotherm of DPPG monolayers spread on water at 35 ^{o}C and for three compression rates.

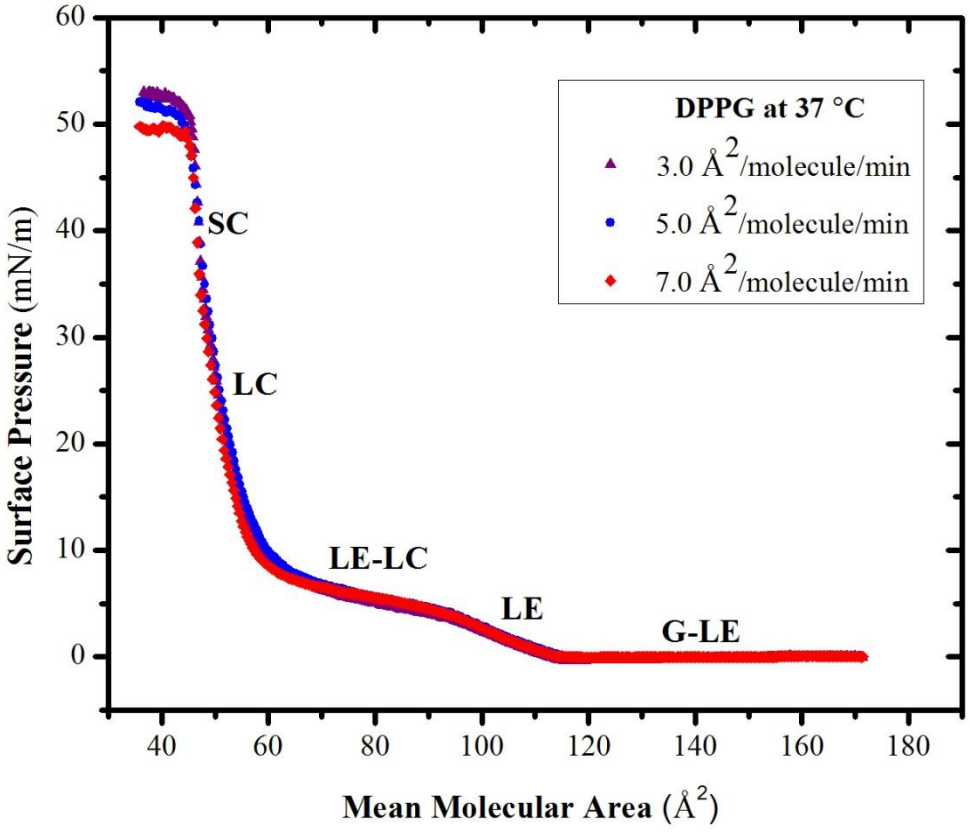

Figure 4.4 Surface pressure-area isotherm of DPPG monolayers spread on water at 37 ^{o}C and for three compression rates.

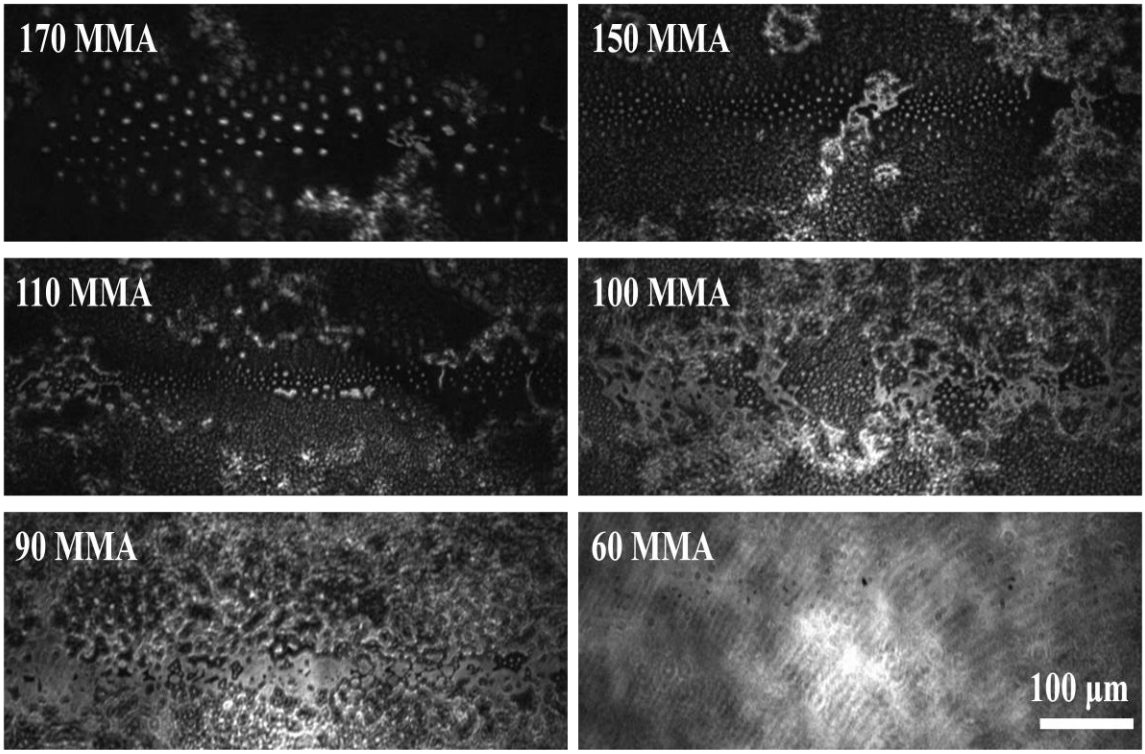

Figure 4.5 BAM images of DPPG domains at 23 ^{o}C for a compression rate of 7.0 Å^{2}/molecule/min. These images can be applied for all compression rates as the domain morphology was not affected.

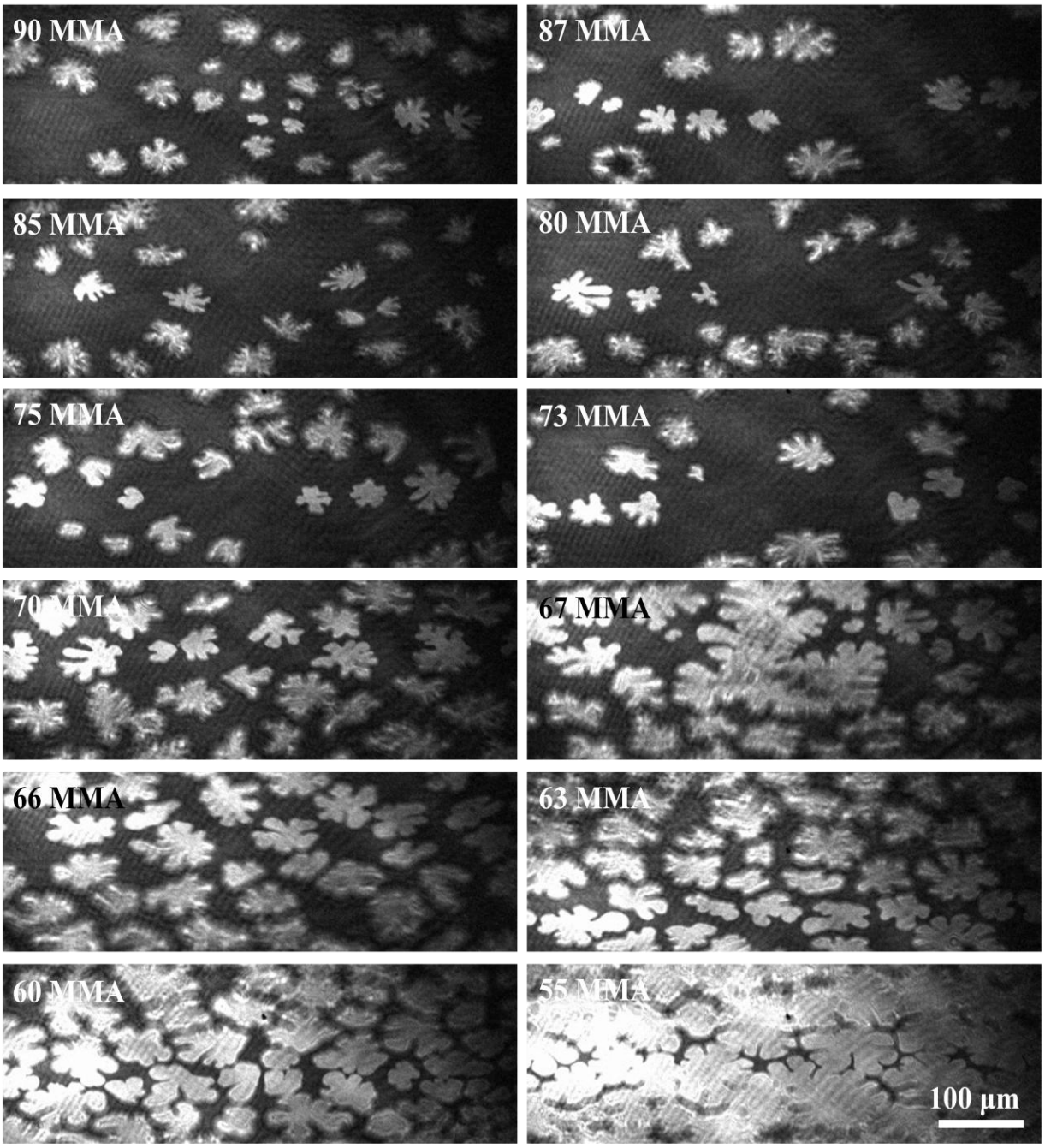

Figure 4.6 BAM images of DPPG domains at 32 ^{o}C and for a compression rate of 3.0 Å^{2}/molecule/min.

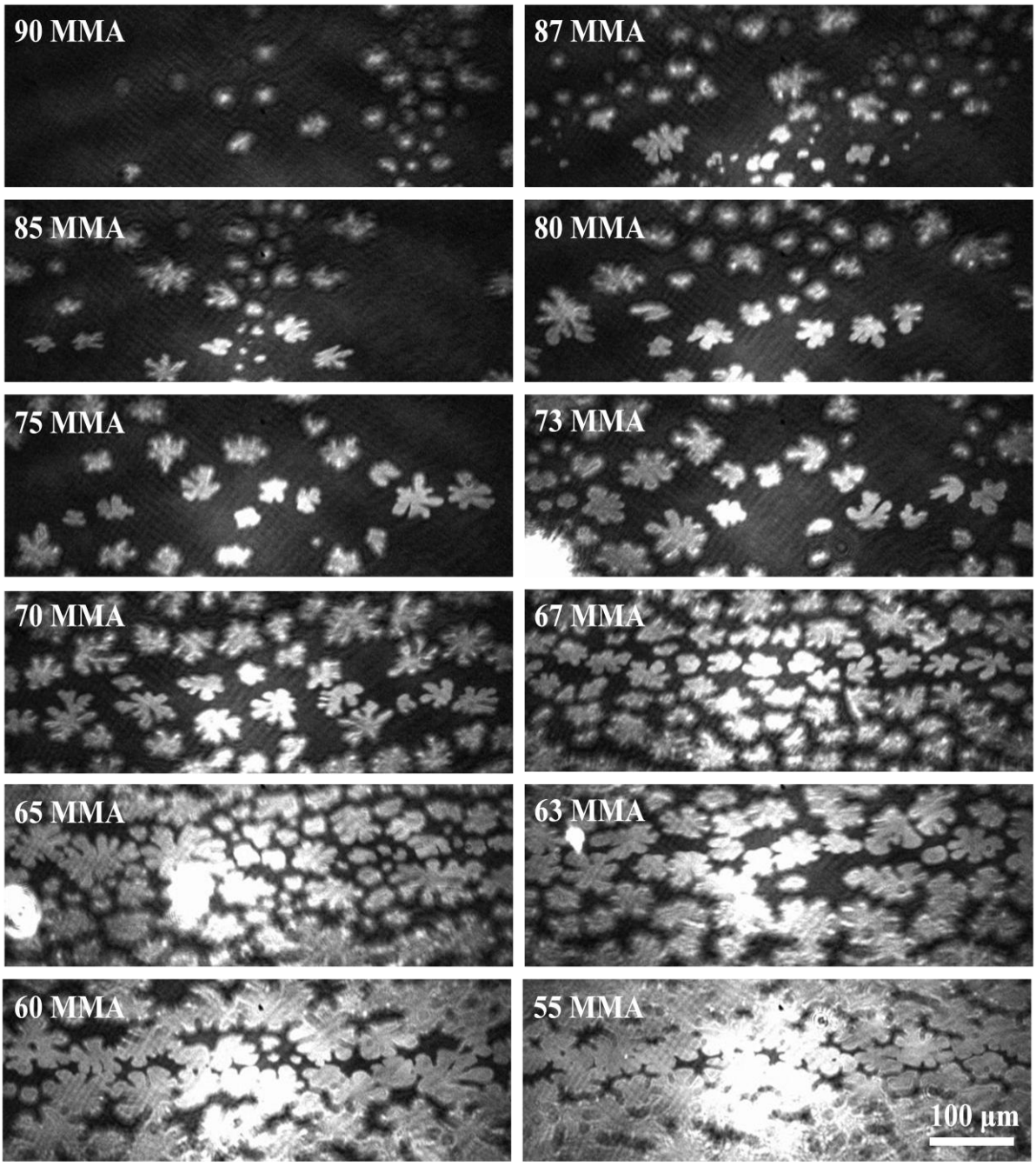

Figure 4.7 BAM images of DPPG domains at 32 ^{o}C and for a compression rate of 5.0 Å^{2}/molecule/min.

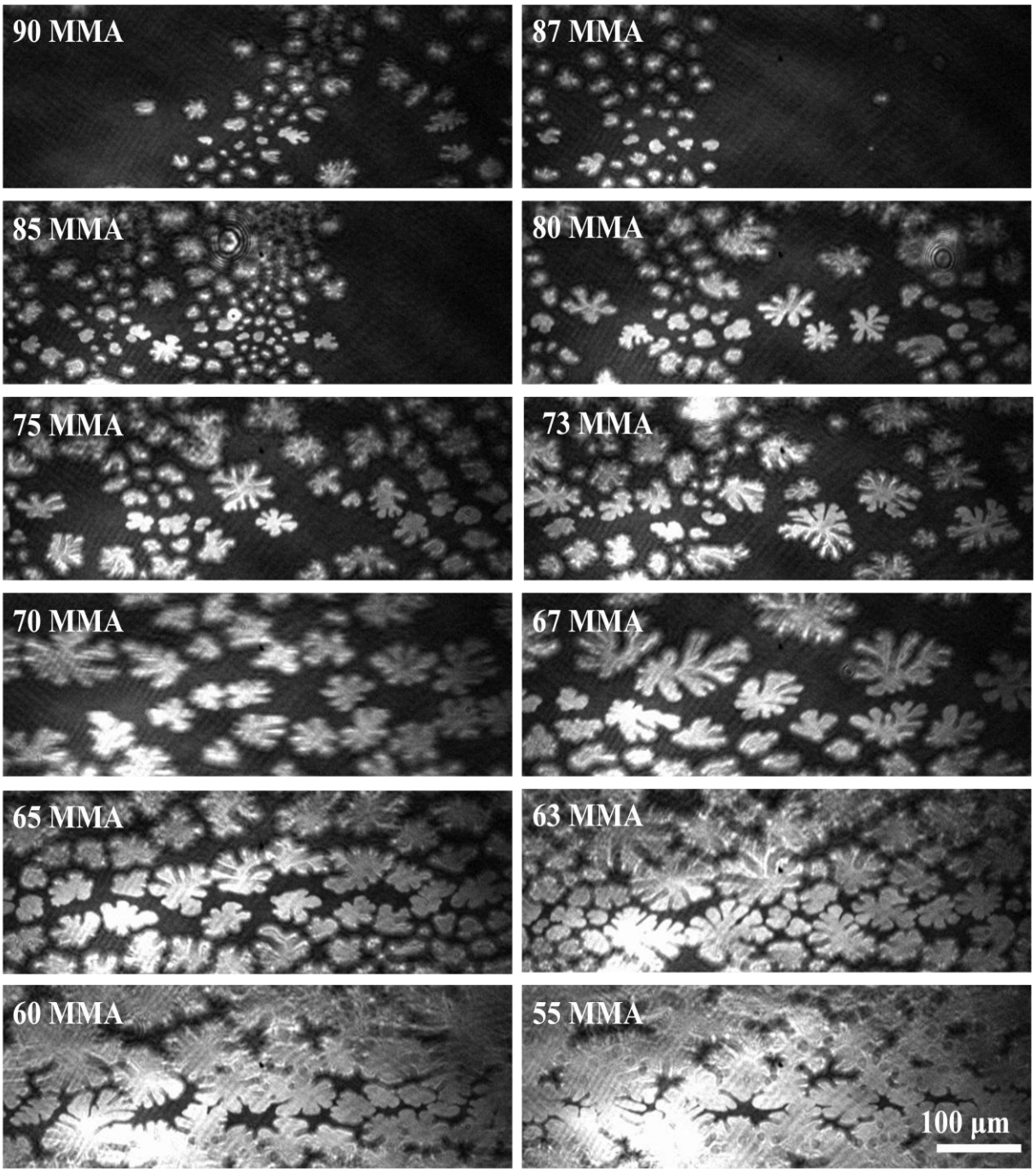

Figure 4.8 BAM images of DPPG domains at 32 ^{o}C and for a compression rate of 7.0 Å^{2}/molecule/min.

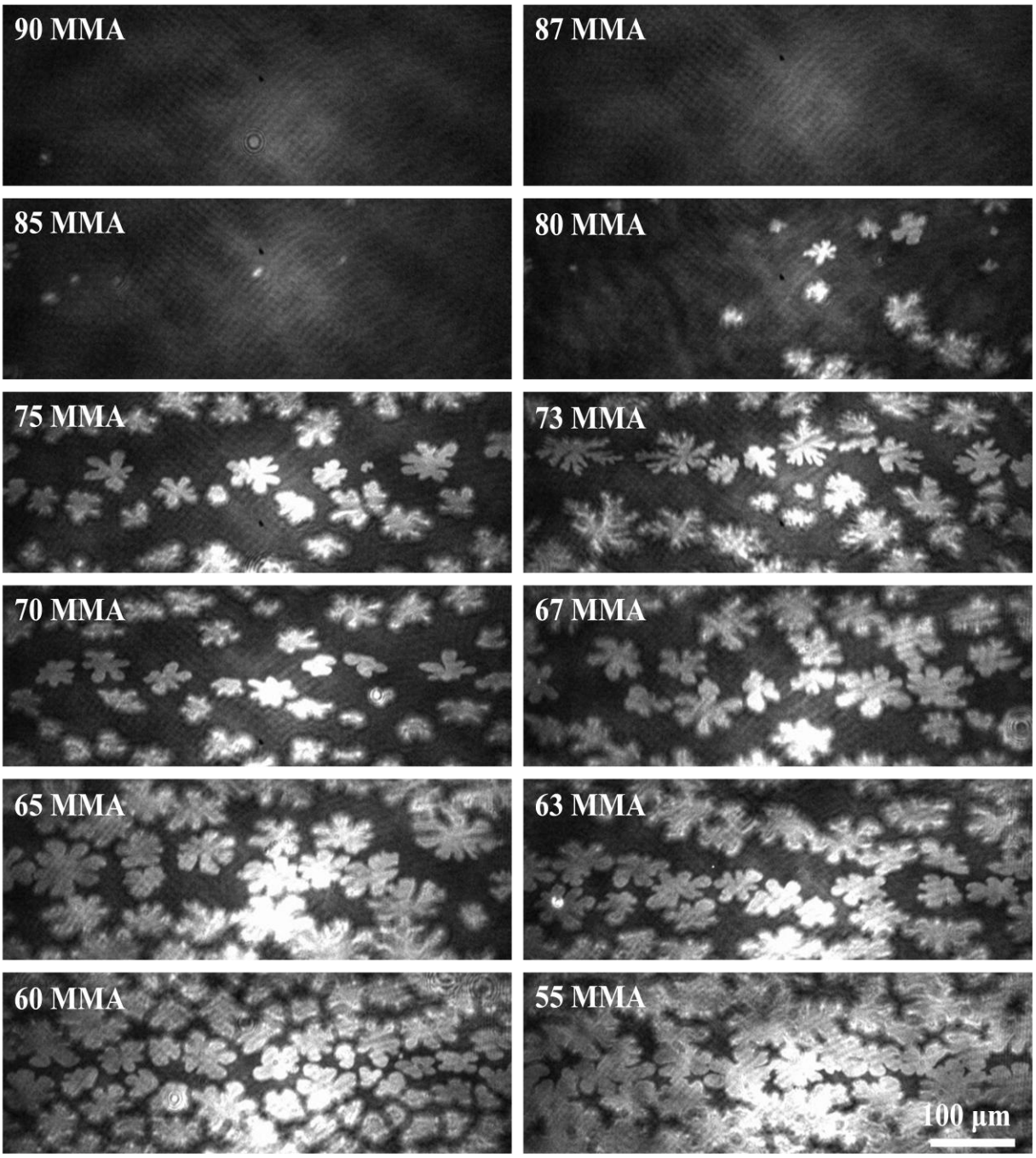

Figure 4.9 BAM images of DPPG domains at 37 ^{o}C and for a compression rate of 3.0 Å^{2}/molecule/min.

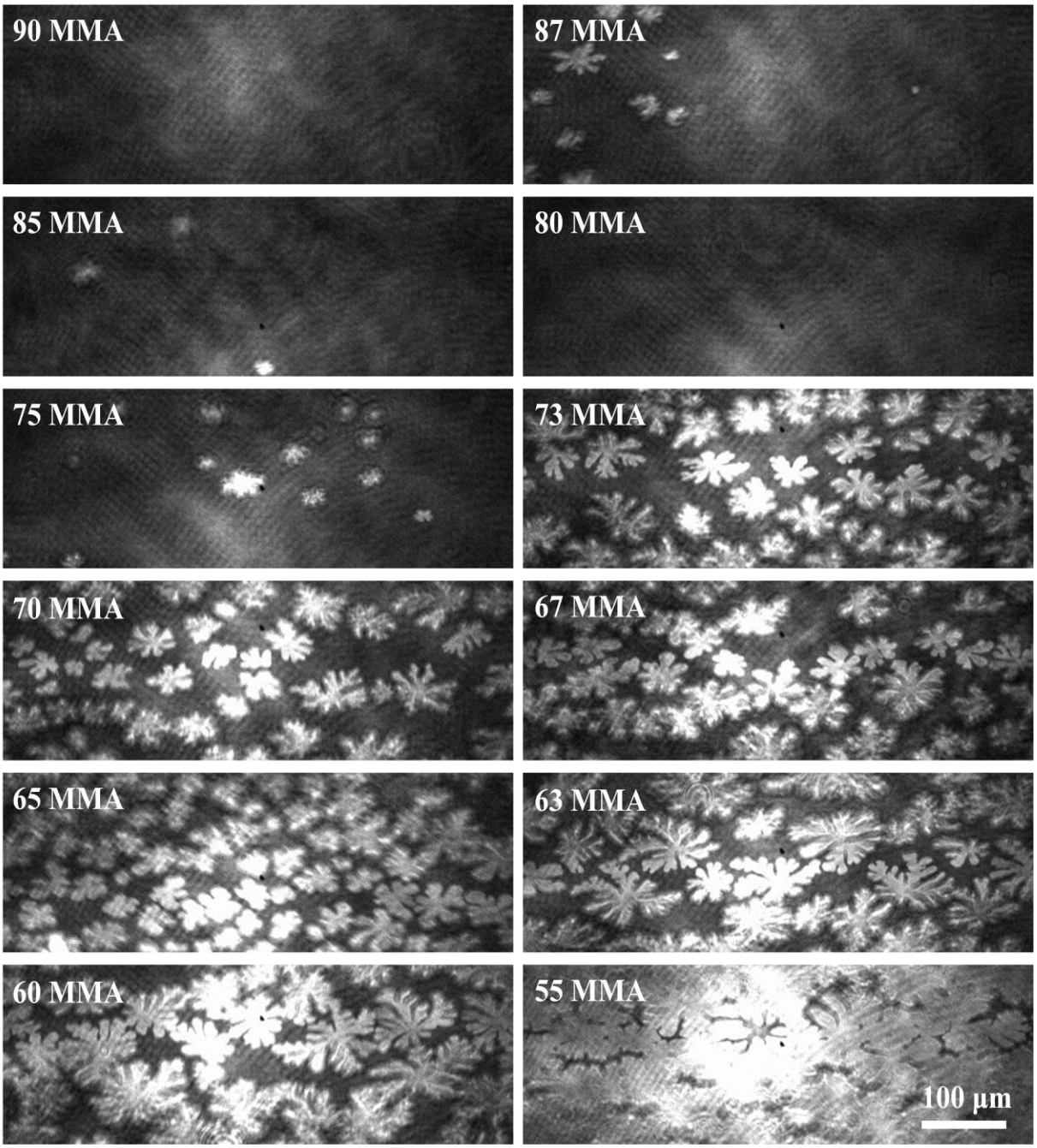

Figure 4.10 BAM images of DPPG domains at 37 ^{o}C and for a compression rate of 5.0 Å^{2}/molecule/min.

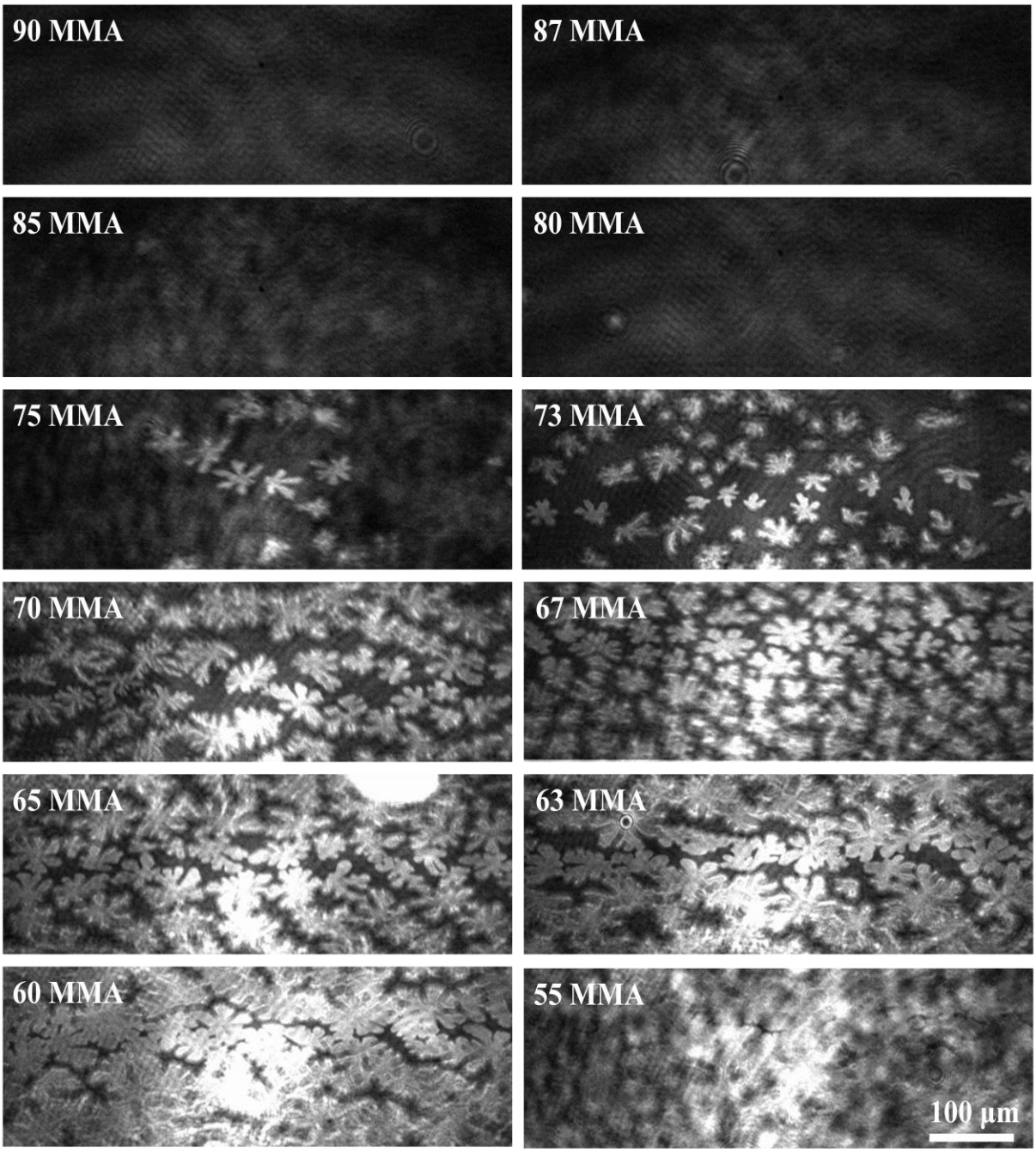

Figure 4.11 BAM images of DPPG domains at 37 ^{o}C and for a compression rate of 7.0 Å^{2}/molecule/min.

5. CONCLUSIONS AND FUTURE WORK

In this thesis, the effects of temperature and compression rate on the phase and morphological behavior of DPPC and DPPE, two zwitterionic lipids, and DPPG, an anionic lipid, spread as monolayers on a water subphase were investigated by means of the surface pressure-area isotherm and Brewster angle microscopy. It was found that the monolayer formed by each individual lipid exhibited different domain number, size, and morphology, depending on the temperature and compression rate.

For the DPPC monolayers, the number of domains in the LE-LC coexistence region increased with the temperature increase but their diameter decreased. The temperature increase also affected the domain morphology; at the lowest temperature, the domains possessed an array of lobed shapes, while at higher temperature they became more circular. In regards to the compression rate, at the lowest temperature, as the compression rate increased the number of domains decreased, however their number increased with higher temperatures. At the highest temperature, the number of domains was not affected by the compression rate indicating that a critical domain number may have been reached. The reduction in the number of the domains at the lowest temperature as the compression rate increased may be due to the fusion of neighboring domains. As the temperature increased the fusion of the domains appear to decrease because of the greater lipid-water interactions.

In the case of DPPE monolayers, as the temperature was increased, domains were observed at a zero surface pressure for at all three temperatures, however there was a reduction in domain size as the temperature increased. The preexisting domains at the higher temperatures however affected domain formation from the LE phase as the number of individual domains were very small at the lower temperature and compression rates The domain number and size also did not follow the same trend as observed with DPPC. In fact, the solid-like nature of the DPPE monolayers resulted in the fusion of domains that were in close proximity to each other even at the highest temperature. As the compression rate increased the fusion of the domains also appeared to increase. Unlike DPPC, domains with multiple branching existed even at the highest temperature.

DPPG monolayers at the lowest temperature also exhibited domains at a zero surface pressure, however as the temperature increased domains were only observed at the LE/LC coexistence region at non-zero surface pressures. The increase in temperature also at the slowest compression rate resulted in a small increase in the number of domains and in a reduction in their diameter. Similar to DPPE monolayers, as the compression rate increased at the higher temperatures, neighboring domains fused to form larger ones. The domain morphology was also similar to DPPE as branched domains were also observed at the highest temperature.

The fusion of domains as the compression rate increases is an indication of increased domain-domain interactions. By comparison of DPPC to DPPE monolayers, the fusion of domains was observed at the lowest temperature with DPPC domains however as the temperature increased the fusion of domains appeared to diminish. In

contrast, for DPPE monolayers, the fusion of smaller domains into large domains was observed even at the highest temperature. One possible reason for the observed differences may be because of the high main phase transition temperature of DPPE in comparison to DPPC.

The fusion of domains at the highest temperature in the DPPG monolayer was also observed even though the transition temperature of DPPG is similar to DPPC. The transition temperatures that are commonly quoted in literature correspond to those of bilayers, however these transition temperatures are also used when referencing monolayers. It appears as though the transition temperature of DPPG monolayer spread over a water subphase may indeed be larger than the transition temperature found for a bilayer.

The hydration of the phospholipid headgroup is dependent on the ability of the lipid to interact with the water molecules. Large domains are an indication of strong attractive lipid-lipid interactions, hence the lipid molecules in large domains are less hydrated than lipid molecules in smaller domains.

The future work with the BAM and Langmuir trough set up include, using a more physiologically relevant subphase, pH, lipid mixtures and more compression rates.

REFERENCES

1. Zuo, Y.Y., et al., *Current perspectives in pulmonary surfactant — Inhibition, enhancement and evaluation.* Biochimica et Biophysica Acta (BBA) - Biomembranes, 2008. **1778**(10): p. 1947-1977.
2. Notter, R.H., *Lung Surfactants: Basic Science and Clinical Applications*. Vol. 149. 2000: Marcel Dekker, Inc.
3. Ware, L.B. and M.A. Matthay, *Medical progress - The acute respiratory distress syndrome.* New England Journal of Medicine, 2000. **342**(18): p. 1334-1349.
4. P. H. Raven and G.B. Johnson, *Biology*. 6th ed. 2002: McGraw-Hill.
5. Ochs, M., et al., *The number of alveoli in the human lung.* American Journal of Respiratory and Critical Care Medicine, 2004. **169**(1): p. 120-124.
6. M. S. Dunnill, *Postnatal growth of the lung.* Thorax, 1962. **17**(329).
7. Hasleton, P.S., *Internal surface-area of adult human lung.* Journal of Anatomy, 1972. **112**(SEP): p. 391-400.
8. http://webschoolsolutions.com/patts/systems/lungs.htm.
9. Wright, J.R., *Immunomodulatory functions of surfactant.* Physiological Reviews, 1997. **77**(4): p. 931-962.
10. Wright, J.R., *Host defense functions of pulmonary surfactant.* Biology of the Neonate, 2004. **85**(4): p. 326-332.
11. Quintero, O.A. and J.R. Wright, *Metabolism of phosphatidylglycerol by alveolar macrophages in vitro.* American Journal of Physiology-Lung Cellular and Molecular Physiology, 2000. **279**(2): p. L399-L407.
12. *Surfactant-replacement therapy for respiratory distress in the preterm and term Neonate.* Pediatrics, 2008. **121**(2): p. 419-432.
13. Veldhuizen, E.J.A. and H.P. Haagsman, *Role of pulmonary surfactant components in surface film formation and dynamics.* Biochimica et Biophysica Acta (BBA) - Biomembranes, 2000. **1467**(2): p. 255-270.
14. Schurch, S., J. Goerke, and J.A. Clements, *Direct determination of surface-tension in lung.* Proceedings of the National Academy of Sciences of the United States of America, 1976. **73**(12): p. 4698-4702.
15. Pastrana-Rios, B., et al., *External reflection absorption infrared spectroscopy study of lung surfactant proteins SP-B and SP-C in phospholipid monolayers at the air/water interface.* Biophysical Journal, 1995. **69**(6): p. 2531-2540.
16. Zhang, H., et al., *On the Low Surface Tension of Lung Surfactant.* Langmuir, 2011. **27**(13): p. 8351-8358.

17. Wright, J.R., *Pulmonary surfactant: a front line of lung host defense.* Journal of Clinical Investigation, 2003. **111**(10): p. 1453-1455.
18. Whitsett, J.A., *Surfactant proteins in innate host defense of the lung.* Biology of the Neonate, 2005. **88**(3): p. 175-180.
19. Zasadzinski, J.A., et al., *The physics and physiology of lung surfactants.* Current Opinion in Colloid & Interface Science, 2001. **6**(5-6): p. 506-513.
20. Schurch, S., et al., *The surface-associated surfactant-reservior in the alveolar lining.* Biology of the Neonate, 1995. **67**: p. 61-76.
21. vonNahmen, A., et al., *The structure of a model pulmonary surfactant as revealed by scanning force microscopy.* Biophysical Journal, 1997. **72**(1): p. 463-469.
22. Ding, J.Q., et al., *Effects of lung surfactant proteins, SP-B and SP-C, and palmitic acid on monolayer stability.* Biophysical Journal, 2001. **80**(5): p. 2262-2272.
23. vonNahmen, A., et al., *The phase behavior of lipid monolayers containing pulmonary surfactant protein C studied by fluorescence light microscopy.* European Biophysics Journal with Biophysics Letters, 1997. **26**(5): p. 359-369.
24. Schurch, S., F.H.Y. Green, and H. Bachofen, *Formation and structure of surface films: captive bubble surfactometry.* Biochimica Et Biophysica Acta-Molecular Basis of Disease, 1998. **1408**(2-3): p. 180-202.
25. Holten-Andersen, N., et al., *KL4 Peptide Induces Reversible Collapse Structures on Multiple Length Scales in Model Lung Surfactant.* Biophysical Journal, 2011. **101**(12): p. 2957-2965.
26. Pattle, R.E., *Surface Lining of lung alveoli.* Physiological Reviews, 1965. **45**(1): p. 48-79.
27. Flach, C.R., et al., *Location of structural transitions in an isotopically labeled lung surfactant SP-B peptide by IRRAS.* Biophysical Journal, 2003. **85**(1): p. 340-349.
28. Baatz, J.E., B. Elledge, and J.A. Whitsett, *Surfactant protein SP-B induces ordering at the surface of model membrane bilayers.* Biochemistry, 1990. **29**(28): p. 6714-6720.
29. Perez-gil, J., C. Casals, and D. Marsh, *Interactions of hydrophobic lung surfactant proteins SP-B and SP-C with the dipalmitoylphosphatidylcholine and dipalmitoylphosphatidylglycerol bilayers studied by electron-spin-resonance spectroscopy.* Biochemistry, 1995. **34**(12): p. 3964-3971.
30. Veldhuizen, R., et al., *The role of lipids in pulmonary surfactant.* Biochimica Et Biophysica Acta-Molecular Basis of Disease, 1998. **1408**(2-3): p. 90-108.
31. Possmayer, F., *A proposed nomenclature for pulmonary surfactant-associated proteins.* American Review of Respiratory Disease, 1988. **138**(4): p. 990-998.
32. Hawgood, S., *Pulmonary surfactant apoproteins - A review of proteins and genomic structure.* American Journal of Physiology, 1989. **257**(2): p. L13-L22.
33. Taneva, S.G. and K.M.W. Keough, *Adsorption of pulmonary surfactant protein SP-A to monolayers of phospholipids containing hydrophobic surfactant protein SP-B or SP-C: Potential differential role for tertiary interaction of lipids, hydrophobic proteins, and SP-A.* Biochemistry, 2000. **39**(20): p. 6083-6093.

34. Hawgood, S. and F.R. Poulain, *Functions of the surfactant proteins - A perspective.* Pediatric Pulmonology, 1995. **19**(2): p. 99-104.
35. Palaniyar, N., et al., *Domains of surfactant protein A that affect protein oligomerization, lipid structure and surface tension.* Comparative Biochemistry and Physiology a-Molecular and Integrative Physiology, 2001. **129**(1): p. 109-127.
36. Clark, H. and K.B.M. Reid, *Structural requirements for SP-D function in vitro and in vivo: Therapeutic potential of recombinant SP-D.* Immunobiology, 2002. **205**(4-5): p. 619-631.
37. Serrano, A.G. and J. Perez-Gil, *Protein-lipid interactions and surface activity in the pulmonary surfactant system.* Chemistry and Physics of Lipids, 2006. **141**(1-2): p. 105-118.
38. B. Corrin and A. G. Nicholson, *Pathology of the lungs*. 3rd ed. (2011): Churchill Livingstone.
39. Goerke, J., *Pulmonary surfactant: functions and molecular composition.* Biochimica Et Biophysica Acta-Molecular Basis of Disease, 1998. **1408**(2-3): p. 79-89.
40. Keating, E., et al., *A modified squeeze-out mechanism for generating high surface pressures with pulmonary surfactant.* Biochimica et Biophysica Acta (BBA) - Biomembranes, 2012. **1818**(5): p. 1225-1234.
41. Foot, N.J., S. Orgeig, and C.B. Daniels, *The evolution of a physiological system: The pulmonary surfactant system in diving mammals.* Respiratory Physiology & Neurobiology, 2006. **154**(1-2): p. 118-138.
42. Orgeig, S., et al., *Recent advances in alveolar biology: Evolution and function of alveolar proteins.* Respiratory Physiology & Neurobiology, 2010. **173, Supplement**(0): p. S43-S54.
43. Fernsler, J.G. and J.A. Zasadzinski, *Competitive Adsorption: A Physical Model for Lung Surfactant Inactivation.* Langmuir, 2009. **25**(14): p. 8131-8143.
44. Rodriguez, R.J., *Respiratory distress syndrome and its management In: Neonatal-perinatal Medicine: Diseases of the Fetus and Infant*. 7th ed, ed. e. (A.A.Fanaroff and R.J. Martin. (2002), St-Louis: Mosby.
45. McIntyre, R.C., et al., *Thirty years of clinical trials in acute respiratory distress syndrome.* Critical Care Medicine, 2000. **28**(9): p. 3314-3331.
46. http://www.mayoclinic.com/health/ards/DS00944/DSECTION=causes.
47. Kopelman, A.E. and O.P. Mathew, *Common respiratory disorders of the newborn.* Pediatrics in review / American Academy of Pediatrics, 1995. **16**(6): p. 209-17.
48. Frerking, I., et al., *Pulmonary surfactant: functions, abnormalities and therapeutic options.* Intensive Care Medicine, 2001. **27**(11): p. 1699-1717.
49. Lipp, M.M., et al., *Fluorescence, polarized fluorescence, and Brewster angle microscopy of palmitic acid and lung surfactant protein B monolayers.* Biophysical Journal, 1997. **72**(6): p. 2783-2804.
50. M.J. Rosen, J.T.K., *Surfactants and Interfacial Phenomena*. 4th ed: Wiley.

51. Boggs, J.M., *Intermolecular hydrogen-bonding between lipids: influence on the organization and function of lipids in membranes.* Canadian Journal of Biochemistry, 1980. **58**(10): p. 755-770.
52. Wydro, P., *The interactions between cholesterol and phospholipids located in the inner leaflet of humane erythrocytes membrane (DPPE and DPPS) in binary and ternary films-The effect of sodium and calcium ions.* Colloids and Surfaces B-Biointerfaces, 2011. **82**(1): p. 209-216.
53. Bruni, R., et al., *Synthetic mimics of surfactant proteins B and C: In vitro surface activity and effects on lung compliance in two animal models of surfactant deficiency.* Molecular Genetics and Metabolism, 1998. **63**(2): p. 116-125.
54. Boggs, J.M., *Lipid intermolecular hydrogen-bonding-influence on structural organization and membrane-function.* Biochimica Et Biophysica Acta, 1987. **906**(3): p. 353-404.
55. Brezesinski, G. and H. Mohwald, *Langmuir monolayers to study interactions at model membrane surfaces.* Advances in Colloid and Interface Science, 2003. **100**: p. 563-584.
56. Möhwald, H., *Phospholipid monolayers*, in *Handbook of Biological Physics*, E.S. R. Lipowsky, Editor. (1995), Elsevier. p. 161-211.
57. Vandeenen, L.L.M., et al., *Monomolecular layers of synthetic phosphatides* Journal of Pharmacy and Pharmacology, 1962. **14**(7).
58. Phillips, M.C. and D. Chapman, *Monolayer characteristics of saturated 1,2-diacyl phosphatidylcholines (lecithins) and phosphatidylethanolamines at air-water interface.* Biochimica Et Biophysica Acta, 1968. **163**(3): p. 301-&.
59. Chapman, D., et al., *Mixed monolayers of phospholipids and cholesterol.* Biochimica Et Biophysica Acta, 1969. **183**(3): p. 458-&.
60. Weis, R.M. and H.M. McConnell, *Two-dimensional chiral crystals of phospholipid.* Nature, 1984. **310**(5972): p. 47-49.
61. Yu, H. and S.W. Hui, *Methylation effects on the microdomain structures of phosphatidylethanolamine monolayers.* Chemistry and Physics of Lipids, 1992. **62**(1): p. 69-78.
62. Wilkin, J., et al., *Spectroscopy & microscopy of aqueous lipid monolayers with applications to pulmonary surfactant: IR and fluorescence studies.* Biophysical Journal, 1997. **72**(2): p. MP271-MP271.
63. Sibug-Aga, R. and R.C. Dunn, *High-resolution studies of lung surfactant collapse.* Photochemistry and Photobiology, 2004. **80**(3): p. 471-476.
64. Kjaer, K., et al., *Ordering in lipid monolayers studied by synchrotron X-ray-diffraction and fluorescence.* Physical Review Letters, 1987. **58**(21): p. 2224-2227.
65. Dutta, P., et al., *X-ray-diffraction studies of organic monolayers on the surface of water.* Physical Review Letters, 1987. **58**(21): p. 2228-2231.
66. Guyot-sionnest, P., J.H. Hunt, and Y.R. Shen, *Sum-frequency vibrational spectroscopy of a langmuir film - study of monolayer-orientation of a two-dimensional system.* Physical Review Letters, 1987. **59**(14): p. 1597-1600.

67. R.G. Dluhy and D.G. Cornell, *In situ measurement of the infrared spectra of insoluble monolayers at the air/water interface.* J. Phys. Chem., 1985. **89**: p. 3195-3197.
68. Blaudez, D., et al., *Polarization modulation FTIR spectroscopy at the air-water interface.* Thin Solid Films, 1994. **242**(1-2): p. 146-150.
69. Mohwald, H., *Phospholipid and phospholipid-protein monolayers at the air-water interface.* Annual Review of Physical Chemistry, 1990. **41**: p. 441-476.
70. McConnell, H.M., *Structures and transitions in lipid monolayers at the air-water interface.* Annual Review of Physical Chemistry, 1991. **42**: p. 171-195.
71. Knobler, C.M. and R.C. Desai, *Phase - transitions in monolayers.* Annual Review of Physical Chemistry, 1992. **43**: p. 207-236.
72. Dhar, P., et al., *Lipid-Protein Interactions Alter Line Tensions and Domain Size Distributions in Lung Surfactant Monolayers.* Biophysical Journal, 2012. **102**(1): p. 56-65.
73. Dhar, P., et al., *Active Interfacial Shear Microrheology of Aging Protein Films.* Physical Review Letters, 2010. **104**(1).
74. Keller, D.J., H.M. McConnell, and V.T. Moy, *Theory of superstructures in the lipid monolayer phase-transitions* Journal of Physical Chemistry, 1986. **90**(11): p. 2311-2315.
75. D. K. Chattoraj, K.S.B., *Adsorption and the Gibbs Surface Excess*. 1984: Plenum Press.
76. Brown, T.E., et al., *Chemistry: The Central Science* 11th ed. 2009: Pearson Education, Inc.
77. Saad, S.M.I., et al., *A double injection ADSA-CSD methodology for lung surfactant inhibition and reversal studies.* Colloids and Surfaces B-Biointerfaces, 2009. **73**(2): p. 365-375.
78. Langmuir, I., *The constitution and fundamental properties of solids and liquids. II. Liquids.* Journal of the American Chemical Society, 1917. **39**: p. 1848-1906.
79. Lyklema, J., *Fundamentals of Interface and Colloid Science: Solid-Liquid Interfaces*. Vol. II: . 1995.
80. Kaganer, V.M., H. Mohwald, and P. Dutta, *Structure and phase transitions in Langmuir monolayers.* Reviews of Modern Physics, 1999. **71**(3): p. 779-819.
81. Prokop, R.M. and A.W. Neumann, *Measurement of the interfacial properties of lung surfactant.* Current Opinion in Colloid & Interface Science, 1996. **1**(5): p. 677-681.
82. Hu, Y.F., K.Y.C. Lee, and J. Israelachvili, *Sealed minitrough for microscopy and long-term stability studies of Langmuir monolayers.* Langmuir, 2003. **19**(1): p. 100-104.
83. Enhorning, G., *Pulsating bubble technique for evaluating pulmonary surfactant.* Journal of Applied Physiology, 1977. **43**(2): p. 198-203.
84. Schurch, S., et al., *A captive bubble method reproduces the insitu behavior of lung surfactant monolayers* Journal of Applied Physiology, 1989. **67**(6): p. 2389-2396.
85. Kang, N., et al., *Interaction between chitosan and bovine lung extract surfactants.* Biochimica Et Biophysica Acta-Biomembranes, 2008. **1778**(1): p. 291-302.

86. Buontempo, J.T. and S.A. Rice, *Infrared external reflection spectroscopic studies of phase - transitions in Langmuir monolayers of heneicosanol.* Journal of Chemical Physics, 1993. **98**(7): p. 5835-5846.
87. Atkins, P. and J.D. Paula, *Physical Chemistry*. 8th ed. 2006: Oxford University Press.
88. Lipp, M.M., et al., *Coexistence of buckled and flat monolayers.* Physical Review Letters, 1998. **81**(8): p. 1650-1653.
89. Hifeda, Y.F. and G.W. Rayfield, *Evidence for first-order phase transitions in lipid and fatty acid monolayers.* Langmuir, 1992. **8**(1): p. 197-200.
90. Gaines, G.L., Jr., *Insoluble Monolayers at Liquid-Gas Interface*. 1966, New York: Wiley.
91. vonTscharner, V. and H.M. McConnell, *An alternative view of phospholipid pahse behavior at thye air water interface. Microscope and film balance studies* Biophysical Journal, 1981. **36**(2): p. 409-419.
92. M. Lösche, E.S., H. Möhwald, *A fluorescence microscopy study concerning the phase diagram of phospholipids.* Ber. Bunsenges. Phys. Chem, 1984. **87**.
93. Kruger, P. and M. Losche, *Molecular chirality and domain shapes in lipid monolayers on aqueous surfaces.* Physical Review E, 2000. **62**(5): p. 7031-7043.
94. Sriram, I. and D.K. Schwartz, *Line tension between coexisting phases in monolayers and bilayers of amphiphilic molecules.* Surface Science Reports, 2012. **67**(6): p. 143-159.
95. Losche, M. and P. Kruger, *Morphology of Langmuir monolayer phases*, in *Morphology of Condensed Matter: Physics and Geometry of Spatially Complex Systems*, K. Mecke and D. Stoyan, Editors. 2002. p. 152-171.
96. Seinfeld, J.H. and S.N. Pandis, *Atmospheric Chemistry and Physics: From Air Pollution to Climate Change*. 1998, New York: Wiley.
97. Davies, S. *Nucleation Theory: A Literature Review and Applications to Nucleation Rates of Natural Gas Hydrates*.
98. Arnold, A., et al., *Temperature and pressure dependent growth and morphology of DMPC/DSPC domains studied by Brewster angle microscopy.* Chemistry and Physics of Lipids, 2005. **133**(2): p. 165-179.
99. Adamson, A.W., *Physical Chemistry of Surfaces*. 1982, New York: Wiley.
100. Meunier, J., *Why a Brewster angle microscope?* Colloids and Surfaces A : Physicochemical and Engineering Aspects, 2000. **171**: p. 33-40.
101. Fowles, G.R., *Introduction to Modern Optics*. 2nd ed. 1989: Dover Publications.
102. http://www.ndt-ed.org/EducationResources/CommunityCollege/RadiationSafety/theory/nature.htm.
103. J. Peatross and M. Ware, *Physics of Light and Optics*. 2008.
104. Huard, S., *Polarization of Light*. 1997: John Wiley & Sons.
105. Hecht, E., *Optics*. 4th ed. 2002: Pearson Education, Inc.
106. http://wdict.net/gallery/elliptical+polarization/.
107. Lheveder, C., et al., *A new Brewster angle microscope.* Review of Scientific Instruments, 1998. **69 (3)**: p. 1446 -1450.

108. Yun, H., et al., *Physicochemical properties of phosphatidylcholine (PC) monolayers with different alkyl chains, at the air/water interface.* Bulletin of the Korean Chemical Society, 2003. **24**(3): p. 377-383.
109. Castada, H., *Brewster Angle Microscopy Study of Model Lung Surfactant Systems at the Air-Water and Air-Physiological Buffer Interfaces*, in *The Department of Chemistry*. 2010, The Ohio State University: Columbus. p. 163.
110. Piston, D.W., *Choosing objective lenses: The importance of numerical aperture and magnification in digital optical microscopy.* Biological Bulletin, 1998. **195**(1): p. 1-4.
111. Mansour, H.M. and G. Zografi, *The relationship between water vapor absorption and desorption by phospholipids and bilayer phase transitions.* Journal of Pharmaceutical Sciences, 2007. **96**(2): p. 377-396.
112. Weidemann, G. and D. Vollhardt, *Long-range tilt orientational order in phospholipid monolayers - A comparison of the order in the condensed phases of dimyristoylphosphatidylethanolamine and dipalmitoylphosphatidylcholine.* Colloids and Surfaces a-Physicochemical and Engineering Aspects, 1995. **100**: p. 187-202.
113. Chen, X.K., et al., *Reorganization and Caging of DPPC, DPPE, DPPG, and DPPS Mono layers Caused by Dimethylsulfoxide Observed Using Brewster Angle Microscopy.* Langmuir, 2010. **26**(24): p. 18902-18908.
114. Leekumjorn, S. and A.K. Sum, *Molecular studies of the gel to liquid-crystalline phase transition for fully hydrated DPPC and DPPE bilayers.* Biochimica Et Biophysica Acta-Biomembranes, 2007. **1768**(2): p. 354-365.
115. Hui, S.W., et al., *The structure and stability of phospholipid-bilayers by atomic-force microscopy.* Biophysical Journal, 1995. **68**(1): p. 171-178.
116. http://en.wikipedia.org/wiki/Hydrogen_bond.
117. Chen, X., et al., *Interfacial Water Structure Associated with Phospholipid Membranes Studied by Phase-Sensitive Vibrational Sum Frequency Generation Spectroscopy.* Journal of the American Chemical Society, 2010. **132**(32): p. 11336-11342.
118. Hubner, W. and A. Blume, *Interactions at the lipid-water interface.* Chemistry and Physics of Lipids, 1998. **96**(1-2): p. 99-123.
119. Jendrasi.Gl and J.H. Hasty, *Hydration of phospholipids.* Biochimica Et Biophysica Acta, 1974. **337**(1): p. 79-91.
120. Harper, K.L. and H.C. Allen, *Competition between DPPC and SDS at the air-aqueous interface.* Langmuir, 2007. **23**(17): p. 8925-8931.
121. Ma, G. and H.C. Allen, *DPPC Langmuir monolayer at the air-water interface: Probing the tail and head groups by vibrational sum frequency generation spectroscopy.* Langmuir, 2006. **22**(12): p. 5341-5349.
122. McConlogue, C.W. and T.K. Vanderlick, *A close look at domain formation in DPPC monolayers.* Langmuir, 1997. **13**(26): p. 7158-7164.
123. Weis, R.M. and H.M. McConnell, *Cholesterol stabilizes the crystal liquid interface in phospholipid monolayers.* Biophysical Journal, 1985. **47**(2): p. 4453-4459.

124. Jyoti, A., et al., *An investigation of the compression rate dependence on the surface pressure-surface area isotherm for a dipalmitoyl phosphatidylcholine monolayer at the air/water interface.* Colloids and Surfaces a-Physicochemical and Engineering Aspects, 1996. **116**(1-2): p. 173-180.
125. McConlogue, C.W., D. Malamud, and T.K. Vanderlick, *Interaction of DPPC monolayers with soluble surfactants: electrostatic effects of membrane perturbants.* Biochimica Et Biophysica Acta-Biomembranes, 1998. **1372**(1): p. 124-134.
126. Kane, S.A., M. Compton, and N. Wilder, *Interactions determining the growth of chiral domains in phospholipid monolayers: Experimental results and comparison with theory.* Langmuir, 2000. **16**(22): p. 8447-8455.
127. Vollhardt, D., *Nucleation and growth in supersaturated monolayers.* Advances in Colloid and Interface Science, 1993. **47**: p. 1-23.
128. Nag, K., et al., *Epifluorescence microscopic observation of monolayers of dipalmitoylphosphatidylcholine: dependence of domain size on compression rates* Biochimica Et Biophysica Acta, 1991. **1068**(2): p. 157-160.
129. Helm, C.A. and H. Mohwald, *Equilibrium and nonequilibrium features determining superlattices in phospholipid monolayers.* Journal of Physical Chemistry, 1988. **92**(5): p. 1262-1266.
130. Sun, R., et al., *A monolayer study on phase behavior and morphology of binary mixtures of sulfatides with DPPC and DPPE.* Colloids and Surfaces B-Biointerfaces, 2009. **73**(2): p. 161-167.
131. Kellener, B.M.J., F. Muller-Landau, and D.A. Cadenhead, *The temperature-dependence characterization of insoluble films at the air-water interface.* Journal of Colloid and Interface Science, 1978. **66**(3): p. 597-603.
132. Alexandre, S., et al., *Interaction of FtsZ protein with a DPPE Langmuir film.* Colloids and Surfaces B-Biointerfaces, 2002. **23**(4): p. 391-395.
133. Mayer, M.A. and T.K. Vanderlick, *Monte Carlo simulation of the shapes of domains in phospholipid monolayers.* Physical Review E, 1997. **55**(1): p. 1106-1119.
134. Keough, K.M.W., *Physical chemistry of pulmonary surfactant in the terminal air spaces,* in *Pulmonary Surfactant: From Molecular Biology to Clinical Practice*, B. Robertson, L.M.G.V. Golde, and J.J. Batenburg, Editors. 1992, Elsevier p. 109-164.
135. Jing, W.G., et al., *Headgroup structure and fatty acid chain length of the acidic phospholipids modulate the interaction of membrane mimetic vesicles with the antimicrobial peptide protegrin-1.* Journal of Peptide Science, 2005. **11**(11): p. 735-743.
136. Zhao, W., et al., *Atomic-scale structure and electrostatics of anionic palmitoyloleoylphosphatidylglycerol lipid bilayers with Na+ counterions.* Biophysical Journal, 2007. **92**(4): p. 1114-1124.
137. Kaznessis, Y.N., S.T. Kim, and R.G. Larson, *Simulations of zwitterionic and anionic phospholipid monolayers.* Biophysical Journal, 2002. **82**(4): p. 1731-1742.

138. Pascher, I., et al., *Conformation and packing properties of membrane lipids: the crystal structure of sodium dimyristoylphosphatidylglycerol.* Biochimica Et Biophysica Acta, 1987. **896**(1): p. 77-88.
139. Minones, J., et al., *The effect of polar groups on structural characteristics of phospholipid monolayers spread at the air-water interface.* Colloids and Surfaces a-Physicochemical and Engineering Aspects, 2002. **203**(1-3): p. 273-286.
140. Vollhardt, D., V.B. Fainerman, and S. Siegel, *Thermodynamic and textural characterization of DPPG phospholipid monolayers.* Journal of Physical Chemistry B, 2000. **104**(17): p. 4115-4121.
141. Grigoriev, D., et al., *Effect of monovalent ions on the monolayers phase behavior of the charged lipid DPPG.* Journal of Physical Chemistry B, 1999. **103**(6): p. 1013-1018.

APPENDIX A BAM IMAGES OF DPPE MONOLAYER AT 35.5 ^{o}C

The following BAM images shown in Fig A.1 illustrate the DPPE monolayer at 35.5 ^{o}C and 7.0 Å^{2}/molecule/min compression rate. This experiment was repeated four times and the images displayed differed on each attempt. At 90 MMA for instance, the images differed in terms of reflectivity as the LC phase moved in and out of focus of the objective lens.

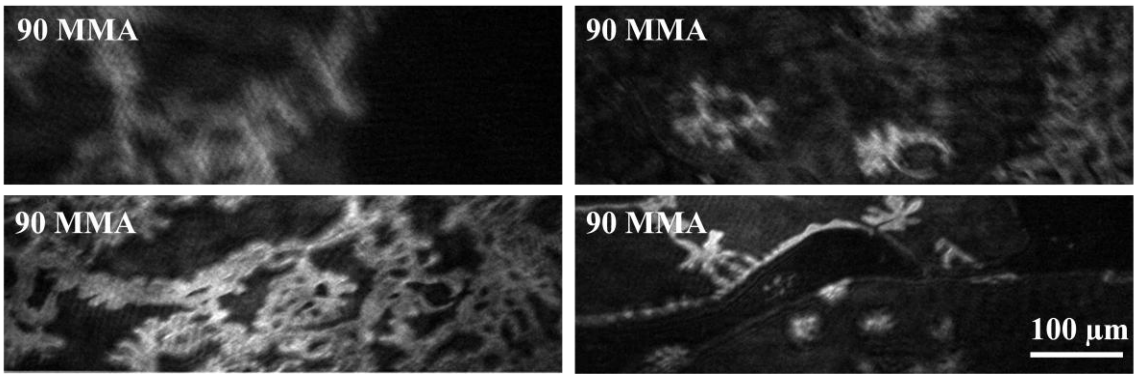

Figure A.1 BAM images of DPPE domains at 35.5 ^{o}C and for a compression rate of 7.0 Å^{2}/molecule/min at 90 MMA